UNIVERSIDADE FEDERAL DO RIO GRANDE DO SUL
ESCOLA DE ENGENHARIA
PROGRAMA DE PÓS-GRADUAÇÃO EM MICROELETRÔNICA

GABRIELA FIRPO FURTADO

State-of-the-art 3-D Monte Carlo Device Simulation: from *n*-MOSFETs to *n*-FinFETs

Thesis presented as a partial fulfillment of the requirements for the degree of Doctorate in Microelectronics.

Advisor: Prof. Dr. Gilson Inácio Wirth

Porto Alegre
2021

CIP – CATALOGING IN PUBLICATION

Furtado, Gabriela Firpo
State-of-the-art 3-D Monte Carlo Device Simulation: from n-MOSFETs to n-FinFETs / Gabriela Firpo Furtado. -- 2021.
92 f.
Orientador: Gilson Inácio Wirth.

Tese (Doutorado) -- Universidade Federal do Rio Grande do Sul, Escola de Engenharia, Programa de Pós-Graduação em Microeletrônica, Porto Alegre, BR-RS, 2021.

1. 3-D TCAD particle-based simulation. 2. Monte Carlo. 3. FinFET. 4. MOSFET. 5. Reliability. I. Wirth, Gilson Inácio, orient. II. Título.

Reitor: Prof. Carlos André Bulhões Mendes
Vice-Reitora: Profa. Patricia Helena Lucas Pranke
Pró-Reitor de Pós-Graduação: Prof. Júlio Otávio Jardim Barcellos
Diretora do Instituto de Informática: Profa. Carla Maria Dal Sasso Freitas
Coordenador do PGMICRO: Prof. Tiago Roberto Balen
Bibliotecária-chefe do Instituto de Informática: Beatriz Regina Bastos Haro

ACKNOWLEDGEMENTS

I would like to thank CNPq for funding my research.

I would like to express my gratitude for my advisor Prof. Gilson Wirth, for all his help and tutelage during the course of my PhD degree. I would also like to thank Prof. Dragica Vasileska for her invaluable advice and sustained support.

I would like to thank my parents and my brother for the solid basis of love, values and effort that allowed me to achieve my goals. I would like to thank my father Jorge for all the caring, for introducing the deeply fundamental love of reading and the enthusiasm for sciences. I would like to thank my mother Cleunice for all the loving and trust, for helping me to develop countless essential competencies such as discernment and critical thinking, for teaching me to be devoted to the people and to the things I value, and for being the pillar of strength during my life. I would also like to thank my partner Vinícius for all the love, unfailing support, understanding, and for our easy, deep lifelong connection.

State-of-the-art 3-D Monte Carlo Device Simulation: from *n*-MOSFETs to *n*-FinFETs

ABSTRACT

A novel 3-D TCAD Monte Carlo n-type semiconductor device simulator is presented in this work. The first step to achieve such comprehensive simulator was to develop a n-type bulk-Si simulator to be used as the basis for the device simulator. A planar PMOS simulator was then fundamentally adapted to a planar NMOS device simulator by incorporating the n-type bulk-Si characteristics and properly changing far-reaching aspects such as carrier dynamics, boundary conditions, scattering mechanisms and their occurrence rates, and band structure. Later, the NMOS device simulator was expanded to tridimensional FinFET structures, accounting for the changes in the device geometry and its impact in boundary checking, the materials on each region, new input variables, potential calculation, velocity and energy calculations, carrier and dopant positions on the new 3-D device, source, drain and gate contacts, and charge conservation. The simulator accounts for real-space treatment of carrier-carrier and carrier-ion interactions. This allows the study of the impact of individual, localized charges and their impact on device variability, besides of avoiding the double-counting of the Coulomb forces which is traditionally attached to momentum-space modelling. In order to substantiate the obtained results, the bulk-Si characteristics were validated with experimental data, and the NMOS and n-FinFET behavior was analyzed and compared to the expected characteristics. The FinFET simulator was then used to obtain novel insights in the study of hot-carrier degradation, which is a major reliability concern on state-of-the-art transistors. The 3-D particle-based simulator was also employed to evaluate ballistic transport under a carrier-centric perspective in deeply scaled FinFETs, and it is now being used to study trap coupling in such devices.

Keywords: 3-D TCAD particle-based simulation. Monte Carlo. FinFET. MOSFET. Reliability. Variability.

Simulação 3-D Monte Carlo de Dispositivos: de n-MOSFETs a n-FinFETs

RESUMO

Um simulador 3-D TCAD Monte Carlo de dispositivos semicondutores inédito é apresentado nesse trabalho. Primeiramente, desenvolveu-se um simulador de substrato de silício tipo *n*, usado como base para o simulador de dispositivos. Um simulador planar PMOS foi então substancialmente adaptado para simular dispositivos NMOS através da incorporação das características do silício tipo *n* e de mudanças necessárias em aspectos como dinâmica de partículas, condições de fronteira, mecanismos de espalhamento e suas taxas de ocorrência e a estrutura de bandas do material. Posteriormente, o simulador NMOS foi expandido para estruturas FinFET tridimensionais, levando em consideração as mudanças na geometria do dispositivo e sua repercussão na checagem das fronteiras, nos materiais em cada região, novas variáveis de entrada, cálculo do potencial, velocidade e energia dos portadores, posições dos portadores e dos dopantes na nova estrutura 3D, contatos de fonte, dreno e porta e conservação de carga. O simulador conta com tratamento no espaço-real das interações portador-portador e portador-íon. Isso possibilita o estudo do impacto de cargas individuais e localizadas e seu impacto na variabilidade do dispositivo, além de evitar a dupla-contagem das forças de Coulomb que tradicionalmente são associadas à modelagem no espaço momento. A fim de substanciar os resultados obtidos, as características do substrato de silício foram validadas com dados experimentais, e o comportamento dos dispositivos NMOS e n-FinFET foram analisados e comparados com as características esperadas. O simulador FinFET foi então usado para proporcionar novo entendimento do estudo de degradação por *hot-carriers*, que é um grande problema de confiabilidade em transistores modernos. O simulador 3-D de partículas foi também empregado para analisar o transporte balístico sob uma perspectiva centrada no portador em FinFETs, e está sendo utilizado agora para estudar acoplamento de armadilhas nesses dispositivos.

Palavras-chave: Simulação 3-D TCAD baseada em partículas. Monte Carlo. FinFET. MOSFET. Confiabilidade. Variabilidade.

LIST OF FIGURES

Figure 1 - Hierarchy of Transport Models 13
Figure 2 - Simplified Bulk Monte Carlo Flowchart 17
Figure 3 - Description of an Ensemble MC method. There are N carriers in the ensemble, Δt is the observation time and the total simulation time is t_s. Each blue symbol corresponds to a scattering event. 23
Figure 4 - Scattering mechanisms for semiconductors 26
Figure 5 – Constant energy surfaces for silicon, showing the *g*-process (along the longitudinal direction) and *f*-process (along a transversal direction). Note that there is one possible final valley for a *g*-process and four possible final valleys for a *f*-process 31
Figure 6 - Flowchart for device simulation based on the ensemble Monte Carlo method. 35
Figure 7- Representation of Different Particle-Mesh Methods 40
Figure 8 - Acoustic scattering rate for silicon. 46
Figure 9 - Non-polar optical scattering rate for silicon. 47
Figure 10 - Electron drift velocity over time 48
Figure 11 - Electron energy *vs* time 49
Figure 12 - Velocity dependence on electric field 49
Figure 13 - Energy dependence on electric field 50
Figure 14 - Charge flow through source and drain contacts 51
Figure 15 - Dependence of carrier energy with position along the device length. 52
Figure 16 - Dependence of carrier velocity on direction along the device length 52
Figure 17 - Drain current *vs* gate voltage for $V_D = 0.3$ V. 54
Figure 18 - Drain current *vs* drain voltage for $V_G=1.1$ V. 54
Figure 19 - Electric potential along device length and depth for $V_G = 1.1$ V, $V_D = V_S = V_B = 0$ V. 55
Figure 20 - Electric potential along device length and depth after 3 ps simulation for $V_G = V_D = 1.1$ V, $V_S = V_B = 0$ V 55
Figure 21 - Electric potential along device length and width for $V_G = 1.1$ V, $V_D = V_S = V_B = 0$ V. 57
Figure 22 - Electric potential along device length and width after 3 ps simulation with $V_G = V_D = 1.1$ V, $V_S = V_B = 0$ V. 58
Figure 23 - Electron density [m^{-3}] along device length and depth for equilibrium condition. . 59
Figure 24 - Electron density [m^{-3}] along device length and width for equilibrium condition. . 59
Figure 25 - Electron density [m^{-3}] along device length and depth after 3 ps simulation 60
Figure 26 - Electron density [m^{-3}] along device length and width after 3 ps simulation. 61
Figure 27 – Basic structure of the FinFET used in this work. The silicon area is presented in gray, the gate dielectric is shown in yellow, the metal gate is depicted in red, and the silicon oxide is shown in blue. 62
Figure 28 - Dopant atoms randomly distributed in the device. The acceptor atoms are represented with black circles, and the donors with blue circles 62
Figure 29 - Electric potential distribution over one of the side gates of a FinFET, showing the presence of metal grains with different characteristics. The yellow cells (1.103 V) have a potential 0.2 V higher than the blue ones (0.903 V), due to the difference in the work function in those regions. 63
Figure 30 - Velocity (a) and energy (b) of the ensemble of carriers in different devices. The black line represents the average values for a set of devices 63
Figure 31 . Electrostatic potential along the device length and depth with $V_D = V_S = V_B = 0$ V and (a) $V_G = 0.1$ V, and (b) $V_G = 0.9$ V. 64

Figure 32 Electrostatic potential in the device as a function of its length and depth with V_D = 0.9 V, V_S = V_B = 0 V, and (a) V_G = 0.1 V, and (b) V_G = 0.9 V. 65
Figure 33 - Electrostatic potential along device length and width for equilibrium condition with V_G = 0.9 V, V_D = V_S = V_B = 0 V. 66
Figure 34 - Electrostatic potential in the device as a function of its width and depth with V_G = V_D = 0.9 V and V_S = V_B = 0 V. 66
Figure 35 - Electron density [m^{-3}] along device length and depth after 15ps simulation for a slice in the middle of the channel width (W/2). 66
Figure 36 - Electron density [m^{-3}] along device length and depth after 15ps simulation for a slice that captures one of the side channels. 67
Figure 37 - I_D -V_G curve for different devices, depicting the variability between devices with the same parameters 68
Figure 38 - I_D -V_D curve for different devices with the same parameters as in Figure 37. 68
Figure 39 - (a) Drain current with (I_{on}) and without (I_{ball}) scattering, (b) percentage of carriers which suffer zero scattering events (ballistic carriers) for different channel lengths and (c) the ballisticity ratio compared to other similar works from the literature, being [1] (ELTHAKEB; ELHAMID; ISMAIL, 2015), [2] (PALESTRI *et al.*, 2005), [10] (BUFLER *et al.* 2017) and [11] (PALESTRI *et al.*, 2004). 72
Figure 40 - Histogram of the number of scattering events a single carrier experienced while crossing the channel in devices with channel lengths of (a) 14 nm, (b) 22 nm and (c) 30 nm. The histograms are normalized by the number of carriers evaluated to show the probability as a function of the scattering events count. 74
Figure 41 - The main plot shows the bivariate histograms of the scattering events a single carrier experienced while crossing the channel in devices with channel lengths of (a) 14 nm, (b) 22 nm and (c) 30 nm. The sub-plots show the normalized histogram for particular scattering mechanism (either phonon scattering or surface roughness scattering). 75
Figure 42 - Distribution of the transit time in 14 and 30 nm gate length devices. Case (a) considers all carriers that crossed the channel, and case (b) considers only the carriers that had no scattering in the channel. 76
Figure 43 - Distribution of the electrons' energy at three different moments (entrance in the channel, exit of the channel with t_{tr} < 50 fs and exit of the channel with t_{tr} > 100 fs), for (a) 14 nm device and (b) 30 nm device. 78
Figure 44 - Distribution of the electrons' energy for transit times in three different time windows for (a) 14 nm and (b) 30 nm devices. 78
Figure 45 - Distributions of carriers' energy with and without short-range e-e interactions for 14 nm channel length device with transit time smaller than 25 fs (a), between 25 fs and 100 fs (c) and larger than 100 fs (e), and for 30 nm channel length devices with transit time smaller than 70 fs (b), between 70 fs and 200 fs (d) and larger than 200 fs (f). 79

LIST OF TABLES

Table 1 - Mean and Standard Deviation of the Distributions in Figure 45(a),(c),(e) 80
Table 2 – Mean and Standard Deviation of the Distributions in Figure 45(b),(d),(f) 81

LIST OF ABREVIATIONS AND ACRONYMS

BTE	Boltzmann Transport Equation
CIC	Cloud-in-Cell
DOS	Density of States
EMC	Ensemble Monte Carlo
FinFET	Fin Field-Effect Transistor
GD	Global Problem Domain
HCD	Hot-carrier Degradation
IEEE	Institute of Electrical and Electronics Engineers
MC	Monte Carlo
MESFET	Metal-Semiconductor Field-Effect Transistor
MGG	Metal Grain Granularity
MOSFET	Metal-Oxide-Semiconductor Field-Effect Transistor
NEC	Nearest-Element-Center
NGP	Nearest-Grid-Point
NMOS	Negative-Channel Metal-Oxide-Semiconductor
P^3M	Particle-Particle-Particle-Mesh
PM	Particle-Mesh
PMOS	Positive-Channel Metal-Oxide-Semiconductor
PP	Particle-Particle
RDF	Random Dopant Fluctuation
SD	Standard Deviation
SE	Standard Error
SRD	Short-Range Domain
TCAD	Technology Computer-Aided Design

TABLE OF CONTENTS

1 INTRODUCTION...12

2 MONTE CARLO METHOD FOR TRANSPORT CALCULATION....................16

2.1 Single-Particle Monte Carlo Method 16
2.1.1 Initial Condition 17
2.1.2 Free-Flight Time Generation 18
2.1.3 Drift Process 20
2.1.4 Scattering Event 20
2.1.5 Scattering Rates 21

2.2 Ensemble Monte Carlo Method 22
2.2.1 Velocity and Energy Calculations 25

3 SCATTERING MECHANISMS...26

3.1 Phonon Scattering 27
3.1.1. Acoustic Phonon Scattering 28
3.1.2. Non-polar Optical Phonon Scattering 30
3.1.3. Ionized Impurity Scattering 32

4 DEVICE SIMULATION..34

4.1 Simulation Steps 34
4.1.1 Material Parameters Initialization 36
4.1.2 Mesh size and Time-step.. 36
4.1.3 Device Structure Description 37
4.1.4 Metal Grain Granularity 38
4.1.5 Dopants Distribution 38
4.1.6 Carrier Initialization 39
4.1.7 Monte Carlo Routine 39
4.1.8 Balance of Drain and Source Contacts 39
4.1.9 Particle-Mesh Coupling 39
4.1.10. Particle-particle-particle-mesh (P^3M) Algorithm 40
4.1.11. Poisson's Equation Solver 42

4.2 N-MOSFET Implementation Overview 43

4.3 N-FinFET Implementation Overview 44

5 BULK SILICON MONTE CARLO SIMULATION RESULTS 46

6 N-MOSFET DEVICE SIMULATION RESULTS 51

6.1 Charge Conservation 51

6.2 Carriers Velocity and Energy 52

6.3 Drain Current *vs* Gate and Drain Voltages 53

6.4 Electric Potential 55

6.5 Carrier Densities 58

7 N-FINFET DEVICE SIMULATOR RESULTS..61

8 CASE STUDIES..69

8.1 Ballistic Transport in FinFETs..69
8.1.1. Methodology..71
8.1.2. Results and Discussions..72
8.1.3. Ballistic Transport in n-FinFETs Conclusions……………………………………..……..……… 82

9 CONCLUSIONS..84

REFERENCES..86

1 INTRODUCTION

The constant reduction of semiconductor device dimensions gave rise to an increase in variability, leading to randomly distributed device parameters and circuit response; in parallel, device scaling has made the impact of charge trapping at localized states in the gate dielectric or at the Si/SiO_2 interface grow significantly, turning it into a relevant reliability concern on modern technologies. It has become therefore mandatory to develop proper models and simulators that are able to accurately predict device electrical behavior and its fluctuations due to variability issues. Device simulation may enable the prediction of device behavior and dependence on different parameters without the need to manufacture the device and perform experiments, leading to reduction of manufacturing costs and to performance improvement in future technologies. In this regard, technology computer aided design (TCAD) tools can be very useful, allowing the user to access internal information of device parameters and structure, enabling the evaluation of different scenarios rapidly, decreasing design cycle time, giving insight for next trials on manufacture and shortening time to market.

In order to address the market and academy needs, constant efforts have been made to implement fast and accurate device simulators. Generically, there are two main components of semiconductor device simulation that must be solved self-consistently with one another: transport equations and electromagnetic fields.

The fields are driving forces for charge transport and arise from external sources, charge distribution or current densities. The electric and magnetic fields can be obtained from the solution of Maxwell's equations, but, in certain conditions, it is only necessary to evaluate the quasi-static electric field resulting from Poisson's equation, given by Equation 1, what significantly simplifies the calculations:

$$\frac{\partial^2\psi}{\partial x^2}+\frac{\partial^2\psi}{\partial y^2}+\frac{\partial^2\psi}{\partial z^2}=-\frac{\rho(x,y,z)}{\varepsilon_s}\ , \quad (1)$$

in which ψ is the electric potential, ρ is the free charge density and ε_s is the material permittivity.

The transport equations, alternatively, can have semi-classical or quantum approaches, being the latter more precise, but frequently prohibitively time-consuming. The semi-classical models have been traditionally used in device simulation and describe the charge transport via different solving approaches to the Boltzmann Transport Equation (BTE), employing

techniques like drift-diffusion, hydrodynamic equations and Monte Carlo method. The BTE is given by

$$\frac{\partial f(\boldsymbol{r},\boldsymbol{k},t)}{\partial t}+\frac{1}{\hbar}\nabla_{\mathbf{k}}\mathrm{E}(\mathbf{k})\,.\nabla_{\mathbf{r}}f(\boldsymbol{r},\boldsymbol{k},t)+\frac{\boldsymbol{F}}{\hbar}\nabla_{\mathbf{k}}f(\boldsymbol{r},\boldsymbol{k},t)=\left.\frac{\partial f(\boldsymbol{r},\boldsymbol{k},t)}{\partial t}\right|_{collisions}, \qquad (2)$$

where ħ is the reduced Planck constant, $f(\boldsymbol{r},\boldsymbol{k},t)$ is the one-particle distribution function and the right-hand side is the rate of change of the distribution function due to random collisions (VASILESKA, 2016).

Figure 1 shows different transport models, according to their degree of exactness and implementation difficulty, what characterizes a traditional trade-off.

Figure 1 - Hierarchy of Transport Models

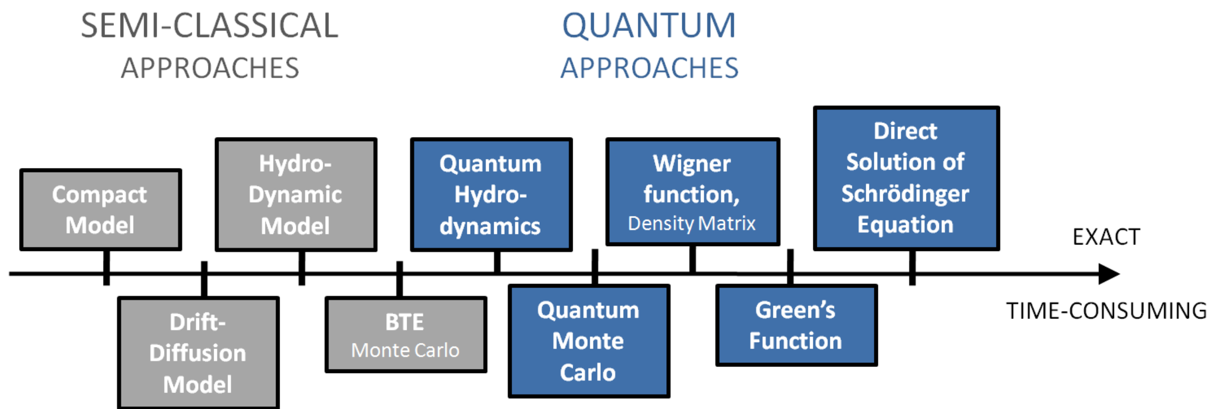

Source: Elaborated by the author

The Monte Carlo method has been extensively used for particle nonequilibrium transport calculation in semiconductor materials and devices in the past decades. It is a powerful tool to evaluate transport properties of carriers in both bulk semiconductor and device simulation. In a semiconductor, a large number of carriers interact mutually, characterizing an intricate many-body system. In order to simplify this analysis when this system can be considered an ensemble of independent carriers, the *single-particle Monte Carlo technique* can be applied to evaluate carrier transport more easily by using an approximate method that simulates this ensemble of carriers by tracking the trajectory of a single carrier undergoing successive scattering events. The *ensemble Monte Carlo method*, alternatively, simulates a synchronous ensemble of particles, simultaneous and successively calculating the motion of many carriers that represent the system of interest. While the single-particle technique is used to simulate the steady-state behavior of a system, and is usually applied in homogeneous bulk semiconductors, the ensemble Monte Carlo simulation is appropriated for transient simulation of semiconductor devices.

The semi-classical models may be invalid for ultrasmall devices in which quantum effects become performance determinant, so that the classical transport concepts are no longer applicable. Some of the effects that may become relevant in down-scaled devices regard the drift process, such as velocity overshoot, ballistic transport, hot-electron and hot-phonon effects, oxide polar optical phonons decreasing channel mobility, and some regard diffusion processes, like its anisotropy and hot-electron diffusion. The environment also has a relevant impact in ultrasmall devices through low-level radiation effects, remote polar scattering, synergetic effects, parasitic and interconnect factors. Effects directly connected to the device size, like spatial quantization, bigger influence of device boundaries on performance and quantum resonances also must be taken into account. Generation-recombination noise, hot-electron thermionic emissions, impact ionization effects, low-dimensional effects, quantum transport, interface physics modeling, long-range Coulomb potential, electron-phonon interactions with confined phonons, re-examine effective mass theory, statistical mechanics of the finite Fermi systems and nonlinear response theory are other important effects that influence down-scaled devices (VASILESKA, 2016). These are not the subject of this work, whose approach is semi-classical, meant to model channels down to 10 nm.

In this work, a bulk n-type silicon Monte Carlo simulator was developed and later expanded to a TCAD *n*-MOSFET simulator; the next and final step was to adapt it to a 3-D *n*-FinFET simulator, allowing state-of-art device simulation. The developed device simulator allows, for example, the insertion of charge traps in the gate oxide in order to evaluate their impact on the device threshold voltage. This is a powerful tool that is not present on commercial simulation tools and can provide insight to device designers on how the real device characteristics deviate from the ideal behavior, without the need to manufacture and test the devices to obtain initial information on trap impact, which varies with the specific technology that is being used. The Monte Carlo device simulator described on this thesis was developed, therefore, aiming to cover topics and allow simulation of effects and phenomena that cannot be studied properly using typical TCAD tools, but are critical to modern device performance.

In the next chapters, the Monte Carlo technique will be discussed in detail and its application to device simulation will be presented. Chapter 2 introduces the Monte Carlo method for particle transport, explaining its logic and main steps. Chapter 3 details the main scattering mechanisms that take place in silicon and presents their scattering rates. The device simulator is introduced in Chapter 4, coupling particle transport to Poisson's equation.

Simulation results from bulk silicon Monte Carlo algorithm regarding carrier velocity and energy over time for different electric fields will be shown in Chapter 5. Chapters 6 and 7 respectively show results obtained with the n-MOSFET and the n-FinFET device simulator for different aspects, such as current curves, electric potential distribution, electron density, and carrier velocity and energy over the channel length. Chapter 8 presents the main case studies that have already been performed using the 3-D TCAD device simulator. The conclusions and possible future work will be discussed in Chapter 9.

2 MONTE CARLO METHOD FOR TRANSPORT CALCULATION

The Monte Carlo (MC) technique is a stochastic method to solve large and complex mathematical problems; in this thesis, the MC method is applied to simulate nonequilibrium particle dynamics in semiconductor materials. It is a semi-classical method for solving BTE, since particle motion is treated classically, and particle interactions are introduced through quantum-mechanical perturbation theory. The Monte Carlo algorithm consists of simulating free particle motions (free flights) terminated by random scattering events that repeatedly take place during the total observation time. The algorithm consists of randomly choosing the duration of the free flight and then selecting stochastically the scattering event that aborts the free motion and affects the final energy and momentum of the carrier. This procedure is constantly repeated, creating a free-flight/scattering loop that is interrupted only when the total simulation time is achieved.

2.1 Single-Particle Monte Carlo Method

The single-particle Monte Carlo method applied to transport analysis consists in the simulation of a carrier in the momentum space. The simulation evaluates the drift of a particle (free flight) under constant electric field during a randomly generated time called flight time. The free flight is terminated by a scattering event that is due to, for example, impurities, phonons, or surface roughness. The sequence free flight/scattering is repeated until the simulation end time is reached. The duration of the free flight depends on the total scattering rate, which is the sum of the scattering rates of each individual source of scattering. Figure 2 shows the flowchart for the bulk Monte Carlo method, showing the main simulation steps.

Figure 2 - Simplified Bulk Monte Carlo Flowchart

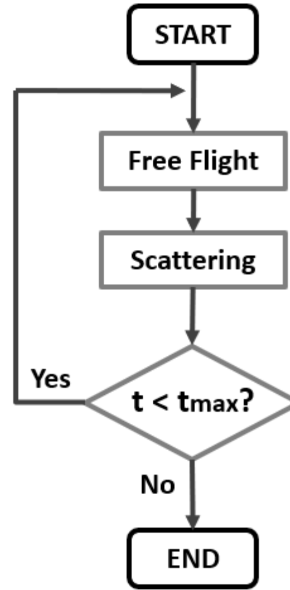

Source: Elaborated by the author

The main steps involved in the Monte Carlo algorithm will be discussed next.

2.1.1 Initial Condition

The particle positions in real space and k-space must be defined. The carrier initial condition is assumed to follow Boltzmann distribution, in which the carrier energy is given by

$$\mathrm{E} = -\frac{3}{2}\,\mathrm{K_B T}\ln(\mathrm{r_1}), \tag{3}$$

where K_B is Boltzmann constant, T is the temperature and r_1 is a random number lying uniformly between 0 and 1, excluding the limits.

The magnitude of the **k** vector is determined from Equation 3 by the *E-k* relation. The bands are often approximated as a parabola in terms of the relation between the energy and the wave vector, i.e., $E = \frac{\hbar^2 k^2}{2m^*}$.

The magnitude of the **k** vector is then explicit as

$$k = \frac{\sqrt{2m^* E}}{\hbar} \tag{4}$$

for parabolic bands.

This approximation is accurate only for energies close to the valley energy minima, where the parabolic-like form is identified. For higher energies, the parabolic approximation becomes inaccurate, and then a more complex, nonparabolic model must be employed.

The k.p perturbation theory (Costato, 1972) gives a nonparabolic equation in the form of Equation 5, that is itself valid as long as $\frac{\hbar k^2}{2m^*} \ll E_g$, being E_g the energy gap between the valence and the conduction bands.

$$E(1 + \alpha E) = \frac{\hbar k^2}{2m^*} \tag{5}$$

The nonparabolicity factor α is a material dependent constant, given by

$$\alpha = \frac{1}{E_g}\left(1 - \frac{m_c}{m_0}\right)^2, \tag{6}$$

in which m_c is the conductivity mass and m_0 is electron rest mass.

For non-parabolic bands, **k** can be written as

$$k = \frac{\sqrt{2m^* E(1 + \alpha E)}}{\hbar} \tag{7}$$

When $\frac{\hbar k^2}{2m}$ assumes values near the bandgap, the equations 5 and 6 lead to imprecise results, and a full-band calculation is required to model the semiconductor band structure.

The components of the **k** vector are then written as

$$\begin{aligned} k_x &= k\, sin\theta\, cos\phi \\ k_y &= k\, sin\theta\, sin\phi \\ k_z &= k\, cos\theta \end{aligned}\ , \tag{8}$$

where θ is the polar angle and ϕ the azimuthal angle given respectively by

$$\begin{aligned} cos\theta &= 1 - 2r_2 \\ sin\theta &= \sqrt{1 - cos^2\theta} \end{aligned} \tag{9}$$

and

$$\phi = 2\pi\, r_3 \tag{10}$$

where r_2 and r_3 are random numbers uniformly distributed from 0 to 1.

2.1.2 Free-Flight Time Generation

The total scattering rate $W_T[k(t)]$ is the result of the sum of energy-dependent scattering rates, being therefore itself dependent on electron energy and written as

$$W_T[k(t)] = \sum_{i=1}^{N} W_i[k(t)]\, , \tag{11}$$

where the subscript i denotes a particular scattering mechanism, assuming values $i = 1, 2, \dots, N$ for N possible mechanisms.

In order to apply the Monte Carlo method, the probability that a carrier scatters after a free flight must be calculated. The probability that a particle has *not* scattered after a time *t* is given by $1 - \int_0^t W_T[k(t')]dt'$; using the approximation $ln(1 + x) \approx x$ for small values of x, it can be expressed as $exp\left\{-\int_0^t W_T[k(t')]dt'\right\}$. The probability per unit time $P(t)$ of an electron moving freely during a time *t* and then scattering in the time interval *dt* is given by

$$P(t) = W_T[k(t)]exp\left\{-\int_0^t W_T[k(t)]dt\right\}. \quad (12)$$

Now, the free flight time t_r that precedes the scattering events can be determined by evaluating t for a certain $\mathrm{P(t)}/W_T[k(t)]$ in Equation 12, given by a random number r uniformly distributed in the interval]0,1[. The integral in Equation 12 cannot be solved analytically because of the complexity of $W_T[k(t)]$; if a fictitious scattering event is introduced in order to make the total scattering rate constant in time, this difficulty is overcome. This virtual scattering process is called *self-scattering* and it must have no impact in the **k** vector, being defined so that the electron state before and after the scattering event is the same. Although it means the same under a physical approach, it has tremendous advantages mathematically, since the self-scattering rate $W_{self}[k(t)]$ is chosen so that the new total scattering rate Γ becomes constant. Equation 13 shows the mathematical representation of Γ and Equation 14 shows a slightly different representation of the self-scattering rate.

$$\Gamma = W_T[k(t)] + W_{self}[k(t)] \quad (13)$$

$$W_{self}[k(t)] = \Gamma - \sum_{i=1}^{N} W_i[k(t)] \quad (14)$$

The value of Γ is chosen to be larger than the largest original total scattering rate $W_T[k(t)]$.

Since now the total scattering rate Γ is constant, Equation 12 can be rewritten as

$$\mathrm{P(t)} = \Gamma e^{-\Gamma t}\,. \quad (15)$$

Assuming that $r = \frac{\mathrm{P(t)}}{\Gamma}$ is a uniformly distributed random number, the free flight time t_r can be expressed as

$$t_r = -\frac{1}{\Gamma}\ln r\,. \tag{16}$$

Having the free-flight time defined, the carrier will drift during t_r.

2.1.3 Drift Process

Considering the carrier potential energy varies slowly as a function of position, the carrier drift motion can be treated semi-classically, and the carrier is regarded as a free particle with its effective mass. Since in the Monte Carlo method the electric field is assumed to be constant during the free-flight time, the wave vector change $\Delta\mathbf{k}$ can be calculated from

$$\Delta\mathbf{k} = \frac{q}{\hbar}\mathbf{F}\,t_r\,. \tag{17}$$

where q is the carrier charge, ħ is the reduced Planck constant and $\boldsymbol{F}$ is the electric field.

During the drift process, the carrier accelerates freely due to the electric field, and this process stops when it undergoes a random scattering event.

2.1.4 Scattering Event

There are several random scattering events that may occur in semiconductors; for silicon, the main processes are acoustic phonon scattering, non-polar optical phonon scattering and Coulomb scattering.

There are two things concerning the scattering events that must be taken into account: type of scattering and carrier final state.

The selection of the scattering mechanism that terminates the free flight will be dependent on a uniformly distributed random number r_2 which lies between 0 and Γ, excluding the limits, which will be compared to the accumulated scattering rate up to a certain mechanism. Considering the scattering mechanisms are divided into [1,2,...,N] types, the accumulated scattering rate of the *n-th* mechanism includes the scattering rate of all previous mechanisms, i.e., $W_n[k(t)] = \sum_{i=1}^{n} W_i[k(t)]$. The randomly generated number r_2 will then be confronted with $W_n[k(t)]$; the *n-th* scattering mechanism will be chosen when $W_{n-1}[k(t)] < r_2 \leq W_n[k(t)]$, i.e., the selected scattering mechanism will be the first one to have an accumulated scattering rate bigger than r_2.

Since the calculation of $W_n[k(t)]$ is time-consuming, it is appropriated to calculate the scattering rate of every scattering mechanism for the different quantized energy levels that will be used in the simulation. Instead of solving the integral equation every time a carrier undergoes a scattering event, what would make the simulation computational cost prohibitively high, all possible values are previously calculated and organized on a *scattering table*. Every time a collision happens, the scattering rate of each process is taken from the scattering table and compared to a random number as described previously. The scattering rate calculation will be introduced in the next section.

The particle energy and wave vector may change after the scattering event. If an acoustic phonon scattering happens, the energy remains the same as before the event, since it is considered an elastic process. If there is a non-polar optical phonon scattering, the energy of the particle changes by the phonon energy.

2.1.5 Scattering Rates

In order to determine the rates that rule the scattering process, the needed mathematical tooling must be introduced.

The Schrödinger equation is used to determine the electronic states for a periodic potential $V(\boldsymbol{r})$ and is given by

$$\left[-\frac{\hbar^2}{2m_0}\nabla^2 + V(\boldsymbol{r})\right]\psi(\boldsymbol{r}) = E\psi(\boldsymbol{r}), \tag{18}$$

in which ħ is Planck's constant divided by 2π, m_0 is the electron mass in free space, ∇^2 is the Laplacian operator, $\psi(\boldsymbol{r})$ is the eigenfunction to be determined and E is the energy eigenvalue.

The transition rate from an initial state **k** to a final state **k'** can be evaluated by using Fermi's Golden Rule, which is based on the solution of the time-dependent Schrödinger equation and on first-order, time-dependent perturbation theory. The scattering theory is based on the transition probability between two eigenstates that are the solutions of Schrödinger's equation for the perturbation potential H' with the unperturbed Hamiltonian operator H_0 (TOMIZAWA, 1993). The Schrödinger equation that must be solved is

$$i\hbar\frac{\partial\psi(\boldsymbol{r},t)}{\partial \mathrm{t}} = (H_0 + \lambda H')\psi(\boldsymbol{r},t). \tag{19}$$

The unperturbed Hamiltonian operator H_0 is assumed to be solved as $H_0\psi_{\boldsymbol{k}} = E_{\boldsymbol{k}}\psi_{\boldsymbol{k}}$. This work does not mean to provide a detailed mathematical derivation of the quantum mechanical phenomena that rules the scattering mechanisms, but interested readers can find the step-by-step solution in (TOMIZAWA, 1993); the solution of Equation 19 that gives rise to Fermi's Golden Rule will now be presented right away.

For the *j*th scattering mechanism, Fermi's Golden Rule is expressed as

$$\Gamma_j(\boldsymbol{k},\boldsymbol{k}') = \frac{2\pi}{\hbar}\left|M_j(\boldsymbol{k},\boldsymbol{k}')\right|^2 \delta(E_{k'} - E_k \mp \hbar\omega), \tag{20}$$

where $\Gamma_j(\boldsymbol{k},\boldsymbol{k}')$ and $M_j(\boldsymbol{k},\boldsymbol{k}')$ are respectively the transition probability between initial state **k** and final state **k'** and the matrix element for the *j*th scattering mechanism, E_k and $E_{k'}$ are the initial and final state energies of the carrier and $\hbar\omega$ is the energy absorbed (upper sign) or emitted (lower sign) during the transition.

The matrix element of the perturbation potential between states k' and k is given by $M(\boldsymbol{k},\boldsymbol{k}') =< \psi_{k'}|H'|\psi_k >$, and each scattering event leads to a different matrix element. It can also be written as $\langle m,\boldsymbol{k}'|V_j(\boldsymbol{r})|n,\boldsymbol{k}\rangle$ for transitions from state $\boldsymbol{k}$ in band *n* to state $\boldsymbol{k}'$ in band *m*, being $V_j(\boldsymbol{r})$ the scattering potential of the *j-th* process.

Analyzing Equation 20, it becomes clear that the expression for $\Gamma_j(\boldsymbol{k},\boldsymbol{k}')$ is different from zero only if the argument of the δ-function equals zero. This can only be achieved if the final state energy differs from the initial state energy by the phonon energy $\hbar\omega$, what evidences the conservation of energy.

The total scattering rate for a certain scattering mechanism of a given initial state $\boldsymbol{k}$ in band *n* is given by the sum of the individual scattering rates of all possible final states and bands, as shown in Equation 21.

$$\Gamma_j[n,\boldsymbol{k}] = \frac{2\pi}{\hbar}\sum_{m,k'}\left|\langle m,\boldsymbol{k}'|V_j(\boldsymbol{r})|n,\boldsymbol{k}\rangle\right|^2 \delta(E_{k'} - E_k \mp \hbar\omega) \tag{21}$$

The main scattering events that are relevant for silicon and their occurrence rates will be presented in detail in Chapter 3.

2.2 Ensemble Monte Carlo Method

The ensemble Monte Carlo (EMC) method consists on successively applying the single particle method to different carriers. Instead of following the motion of only one carrier

for successive time steps, the ensemble Monte Carlo method follows a large number of carriers during each time step, being the motion of each carrier computed individually and independently. Labeling the carriers present in the material from 1 to N, the method consists of observing the first carrier drift during a Δt, while it may or may not be scattered, then following the motion of the second observed carrier during this time window, repeating this procedure until all N particles have independently drifted during the time interval Δt. At every Δt, the position and momentum of each carrier must be reevaluated so that it can be used to define the motion of the particles during the next time window. The motion of each particle during the next Δt is then determined by the conditions fixed right before the beginning of the drift, i.e., the change in the carrier position *during* the motion in the time window is not considered, so that only the particle final position is considered and determines the conditions of the next drift period.

Figure 3 shows the drift of N particles during a t_s time interval. The observation time window has a length Δt, and the blue symbols indicate when a scattering event took place. Note that it is possible to have none or multiple scatterings during a time interval; nonetheless, the particle drift keeps governed by the conditions defined at the beginning of Δt, i.e., regardless the collisions, there is always a time increment of Δt between two observations.

Figure 3 - Description of an Ensemble MC method. There are N carriers in the ensemble, Δt is the observation time and the total simulation time is t_s. Each blue symbol corresponds to a scattering event.

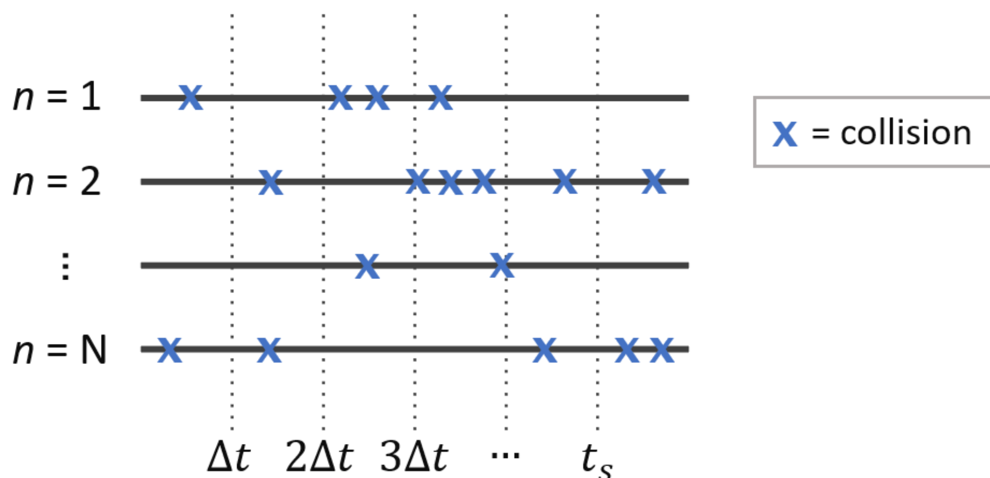

Source: Adapted from Vasileska, 2016

Following a carrier during a time window of length Δt, the time t_{scat} up to the next scattering event, which is defined as the free-flight time, is determined by a random number. There are two major possible scenarios that may happen then, concerning the comparison between the free-flight time and the observation time window:

a) $t_{scat} \geq \Delta t$: When t_{scat} is equal to or larger than the observation time window, the carrier will simply drift during Δt, and the new scattering time will be given by $t_{scat2} = t_{scat} - \Delta t$. If t_{scat2} is still bigger than Δt, it means that, similarly to what happened on the first time interval of Δt, no scattering event will take place during the second observation window. The new free-flight time is determined again by doing $t_{scat3} = t_{scat2} - \Delta t$, and the same procedure is repeated until the scattering time gets smaller than Δt.

b) $t_{scat} < \Delta t$: When the free-flight time is smaller than the observation window, a scattering event will certainly take place before the end of the time interval Δt. The carrier will drift up to t_{scat}, when it will be scattered and the new carrier energy will be evaluated. A new free-flight time t_{scat2} is then defined by generating a random number. If $t_{scat2} < \Delta t - t_{scat}$, it means the second scattering event will happen within this time window, after the particle has drifted during t_{scat2}, and then once again a new free-flight time (t_{scat3}) must be randomly generated. If instead $t_{scat2} > \Delta t - t_{scat}$, the carrier will drift during the remnant time up to the end of the observation time window, when all the other carriers' motion will be evaluated and the real- and momentum-space positions of the particles will be computed. Similarly to what was described in the previous scenario, a new free-flight time will be considered as $t_{scat3} = t_{scat2} + t_{scat} - \Delta t$, and it must be compared to Δt to define it if falls back into the cases (a) or (b).

After the first carrier has drifted for Δt, the motion of all the other carriers in the system will be successively evaluated during this time window. Then, after all the particles have been individually considered, there must be a new evaluation of the particles motion during the next time interval Δt, which has as initial conditions the final positions of the carriers at the end of time window that has just passed. By taking into account a large number of carriers, it becomes possible to simulate the carrier-carrier scattering mechanism.

2.2.1 Velocity and Energy Calculations

The value of relevant quantities associated to the ensemble of particles, such as energy, velocity and valley occupation, which are computed at every time increment of Δt, are calculated as the average of the individual values of each particle. Since the observation of the particles takes place at fixed time-steps of length Δt, the value of these quantities are evaluated at every Δt. Taking the *energy* as an example, its mean value on the *n*th time-step can be calculated by Equation 22, in which N is the total number of particles and i assigns the particle in the ensemble.

$$\bar{e}(n\Delta t) = \frac{1}{N}\sum_{i=1}^{N} e_i(n\Delta t) \tag{22}$$

It is important to note that the number of particles in the simulation defines the precision of the results, characterizing a tradeoff between computational effort and accuracy. The standard error (SE) of the simulation mean result diminishes as the number of particles (N) increases, what is evidenced by the expression $SE = {SD}/{\sqrt{N}}$, where SD is the standard deviation. For the energy mean estimation, the standard deviation itself is given by $SD = \sqrt{\frac{\sum_{i=1}^{N}(e_i)^2 - N\bar{e}^2}{N-1}}$.

3 SCATTERING MECHANISMS

When electrons are being transported in a semiconductor, they undergo scattering processes that change their trajectories. There are several scattering mechanisms that are present in different semiconductors like Si, GaAs and Ge, and the prevalence of each of them depends on the material properties. The main scattering processes that are modeled for semiconductor simulation are due to the carrier interaction with phonons, defects or with other carriers, and can be divided into:

- acoustic phonon scattering;
- non-polar optical phonon scattering;
- polar optical phonon scattering;
- piezoelectric scattering;
- alloy disorder scattering;
- ionized impurity scattering;
- neutral impurity scattering;
- electron-electron interactions;
- impact ionization.

Figure 4 shows the scattering mechanisms listed above divided into the categories of defect scattering, carrier-carrier scattering and lattice scattering.

Figure 4 - Scattering mechanisms for semiconductors

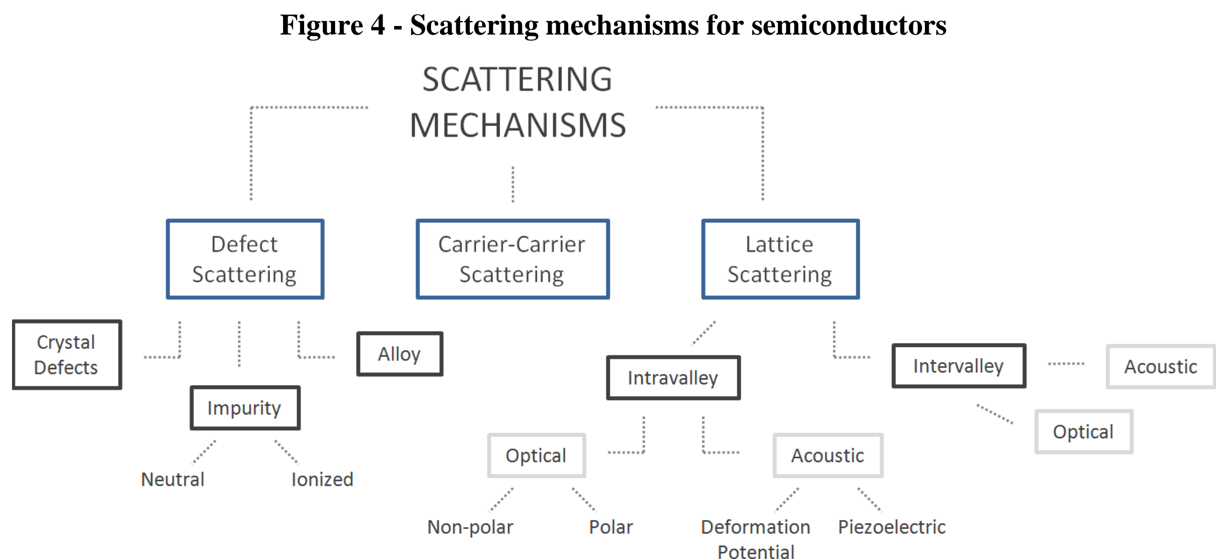

Source: Adapted from Vasileska (2016)

Relevant scattering mechanisms for a silicon material system are: scattering due to intravalley acoustic and inter-valley non-polar optical phonons, surface roughness scattering, and Coulomb scattering. The electron-phonon scattering mechanisms are treated in momentum space. In particle-based device simulations, discussed later in the text, the Coulomb interactions, involving electron-ion and electron-electron interactions, are treated in real space using molecular dynamics approach. In silicon material system, two types of electron-phonon interactions are important: acoustic and non-polar optical phonon scattering. For the sake of completeness, their scattering rate equations will be discussed next, following the approach presented in Vasileska (2016).

3.1 Phonon Scattering

The vibrations of the crystalline lattice disturb the purely periodic potential associated with the regular array of atoms constituting the crystal. The wave nature of the lattice vibrations are quantized as *phonons*, and their interaction with the carriers gives rise to the phonon scattering.

There are two possible phonon modes: acoustic and optical. When neighboring atoms oscillate in the same direction, the phonon belongs to the acoustic branch of the vibration spectra, and, if it interacts with a carrier, the acoustic phonon scattering process takes place. Since the neighboring atoms displace in the same direction, the changes in lattice spacing are produced by the differential displacement or strain. When neighboring atoms vibrate in the opposite directions, alternatively, the lattice spacing is changed directly, and this leads to the optical branch in the phonon spectra. If a carrier interacts with this phonon mode, optical phonon scattering takes place.

The displacement of an ion in the crystal from its equilibrium, zero temperature position leads to a variation in the crystal potential, and this deviation is phenomenologically modeled by a *deformation potential*. The vibrations in the crystal lattice produce an elastic strain, and its variation through the crystal changes the energy of the electronic states. In order to calculate the scattering rates that result from the electron-phonon interactions, the variation on the potential felt by an electron in the conduction band must be evaluated when an atom is displaced from its original position.

In compound semiconductors, the polar nature of bonds can lead to strong interaction; the dipole moment between atoms is perturbed by the phonon displacement of the lattice, resulting in *polar* carrier scattering caused by this electric field. This kind of scattering

mechanism may be originated by both acoustic and optical phonons. The former is called *piezoelectric* scattering and the latter is referred as *polar optical* scattering, being a very relevant process in compound semiconductors.

In the next sections, the most relevant scattering events that occur in silicon will be presented and their modelling on the momentum space will be introduced.

3.1.1. Acoustic Phonon Scattering

For acoustic vibration modes, the unit cell is deformed by the differential displacement of the neighboring atoms. Equation 23 shows that the perturbation potential is given by the product of the deformation potential Ξ_d and the derivative of the lattice displacement $\boldsymbol{u}(\boldsymbol{r},t)$, presented in Equation 24.

$$H' = \Xi_d \, \nabla . \boldsymbol{u}(\boldsymbol{r},t) \tag{23}$$

$$\boldsymbol{u}(\boldsymbol{r},t) = \sum_{\mathbf{q}} \left(\sqrt{\frac{\hbar}{2\rho\Omega\omega_q}} \right) \mathbf{e}_{\mathbf{q}} \left(a_{\mathbf{q}} + a_{\mathbf{q}}{}^{+} \right) e^{i\mathbf{q}.\boldsymbol{r}} \tag{24}$$

Where $\mathbf{q} = \mathbf{k'} - \mathbf{k}$ is the phonon wave vector, $\hbar\omega_q$ is the phonon energy, ρ is the solid density, Ω is the volume of the crystal, $\mathbf{e}_{\mathbf{q}}$ is the unit polarization vector and $a_{\mathbf{q}}$ and $a_{\mathbf{q}}{}^{+}$ are the phonon creation and annihilation operators respectively.

The transition rate, i.e., the transition probability per unit time $S(\boldsymbol{k},\boldsymbol{k'})$ for intravalley acoustic phonon scattering can be calculated by solving Equation 23 for the lattice displacement given by equation 24. The interaction potential for acoustic phonons is then given by Equation 25.

$$H' = \sum_{\mathbf{q}} iq\Xi_d \left(\sqrt{\frac{\hbar}{2\rho\Omega\omega_q}} \right) \left(a_{\mathbf{q}} + a_{\mathbf{q}}{}^{+} \right) e^{i\mathbf{q}.\boldsymbol{r}} \tag{25}$$

Equation 25 can be used to obtain the matrix element of the perturbation potential, and then it can be substituted into Fermi's golden rule to result in the transition rate shown in Equation 26.

$$S(\boldsymbol{k},\boldsymbol{k'}) = \frac{\pi\, \Xi_d^2 q^2}{\rho\Omega\omega_q} \left(n_q + \tfrac{1}{2} \mp \tfrac{1}{2} \right) \delta(\boldsymbol{k'} - \boldsymbol{k} \mp \boldsymbol{q}) \delta(E_{\boldsymbol{k'}} - E_{\boldsymbol{k}} \mp \hbar\omega_q) \tag{26}$$

where the two δ-functions express the conservation of momentum and energy, the $\mp$ sign denotes the absorption and emission processes and n_q is the number of acoustic phonons in a state $\mathbf{q}$, described with the Bose-Einstein distribution function shown in Equation 27.

$$n_{\boldsymbol{q}} = 1/(e^{\frac{\hbar\omega_{\boldsymbol{q}}}{K_B T_L}} - 1) \tag{27}$$

At room temperature, the acoustic phonon energy $\hbar\omega_{\boldsymbol{q}}$ is significantly smaller than $K_B T_L$, so the acoustic phonon scattering can be approximated as elastic. On this case, the equipartition is applicable and $n_{\boldsymbol{q}}$ can be expressed as $n_{\boldsymbol{q}} \approx {K_B T_L}/{\hbar\omega_{\boldsymbol{q}}}$, where T_L is the lattice temperature.

Using these approximations, Equation 26 can be rewritten as

$$S(\boldsymbol{k}, \boldsymbol{k}') = \frac{\pi\, \Xi_d^2 K_B T_L}{\hbar\rho {v_s}^2 \Omega} \frac{k}{qE} \delta\left(\frac{q}{2k} \pm cos\theta'\right), \tag{28}$$

where θ' is the polar angle between $\boldsymbol{k}$ and $\boldsymbol{q}$ and $v_s = \sqrt{\frac{c_L}{\rho}} = \frac{\omega_q}{q}$ is the velocity of sound in the crystal.

Integrating Equation 28, the total intravalley acoustic phonon scattering rate out of state k is given by

$$W(E) = \left(\frac{2\pi\, \Xi_d^2\, K_B T_L}{\hbar\rho {v_s}^2}\right) N(E), \tag{29}$$

in which $N(E)$ is half of the density of states (DOS) function.

Considering a parabolic band structure, $N(E)$ has the form shown in Equation 30, where $m_d^* = \sqrt[3]{m_l {m_t}^2}$ is the DOS effective mass.

$$N(E) = \left(\frac{(2m_d^*)^{\frac{3}{2}} \sqrt{E}}{4\pi^2 \hbar^3}\right) \tag{30}$$

For normal device operation, however, the applied electric fields are large and the carriers acquire very high kinetic energy, making the parabolic approximation inaccurate. The nonparabolic band model is a better option then, and half the DOS function assumes the values expressed by

$$N(E) = \left(\frac{(2m_d^*)^{\frac{3}{2}} \sqrt{E(1 + \alpha E)}}{4\pi^2 \hbar^3}\right)(1 + 2\alpha E). \tag{31}$$

Substituting Equation 31 into Equation 29, the elastic acoustic phonon scattering rate out of state **k** for nonparabolic bands equals to:

$$W(E) = \left(\frac{2\pi\, \Xi_d^2\, K_B T_L}{\hbar \rho {v_s}^2}\right)\left(\frac{(2m_d^*)^{\frac{3}{2}}\sqrt{E(1+\alpha E)}}{4\pi^2\hbar^3}\right)(1+2\alpha E) \tag{32}$$

3.1.2. Non-polar Optical Phonon Scattering

In order to analyze the scattering caused by carrier interaction with non-polar optical phonons, it becomes necessary to introduce a parameter of optical displacement. The relative displacement of atoms in a unit cell may affect the electronic energy directly. Since neighboring atoms oscillate in opposite directions in the optical modes of vibration, the resulting perturbation potential, as shown in Equation 33, is a product of the intervalley deformation potential $\boldsymbol{D}_{ij}$ and the lattice optical displacement $\boldsymbol{u}(\boldsymbol{r}, t)$, which was itself given in Equation 24.

$$H' = \boldsymbol{D}_{ij} \,.\, \boldsymbol{u}(\boldsymbol{r}, t) \tag{33}$$

The intervalley deformation potential quantifies the scattering strength from the initial valley i to the final valley j.

The transition rate for intervalley non-polar optical phonon scattering is then obtained using Fermi's golden rule as:

$$S(\boldsymbol{k}, \boldsymbol{k}') = \frac{\pi\, D_{ij}^2\, Z_j}{\rho \omega_{ij} \Omega}\left[n(\omega_{ij}) + \tfrac{1}{2} \mp \tfrac{1}{2}\right] \delta(E_{k'} - E_k \mp \hbar\omega_{ij} + \Delta E_{ji}) \tag{34}$$

where D_{ij} is the intervalley deformation potential, Z_j is the number of available final states for the carrier to scatter into, $n(\omega_{ij})$ is the phonon occupancy factor given by the Bose-Einstein distribution function shown in Equation 27, $\hbar\omega_{ij}$ is the energy of the non-polar optical phonon, E_k is the electron energy and ΔE_{ji} is the difference between the potential energies in the bottom of the valley *j* and the bottom of valley *i*.

Regarding the number of final states available for scattering (Z_j), the intervalley non-polar acoustic phonon scattering may be divided in two categories, which are known as *f*-process and g-process. This division is based on the material's constant energy surfaces, as shown in Figure 5 for silicon. If the scattering forces the carrier to move to a valley that is located along the original axis where the carrier was located previously to the collision, the carrier is scattering in a longitudinal direction, characterizing a g-process. In this case, there is only one valley available as an option for the final state, what makes $Z_j = 1$. Otherwise, if the

carrier is scattered to a valley that is located in an axis different from the one where the initial valley is located, the carrier is scattered in a transverse direction. There are then four options as feasible final valleys after the scattering, making $Z_j = 4$ and defining a *f*-process.

Figure 5 – Constant energy surfaces for silicon, showing the *g*-process (along the longitudinal direction) and *f*-process (along a transversal direction). Note that there is one possible final valley for a *g*-process and four possible final valleys for a *f*-process.

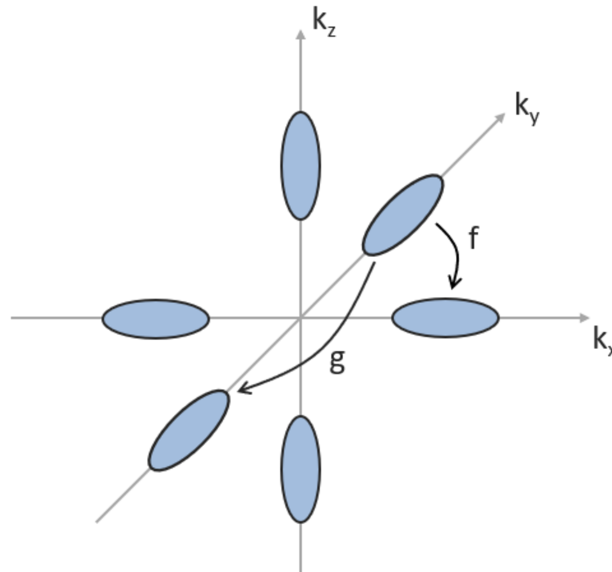

Source: Elaborated by the author

The total scattering rate out of state k is obtained by integrating equation 34. For a parabolic band structure and using a zero-order approximation, the scattering rate is of the form

$$W(E) = \frac{\pi\, D_{ij}^2\, Z_j}{\rho\omega_{ij}} \left[n(\omega_{ij}) + \tfrac{1}{2} \mp \tfrac{1}{2}\right] N(E_k \pm \hbar\omega_{ij} - \Delta E_{ji}) \tag{35}$$

where $Z_j = 1$ for g-type process and $Z_j = 4$ for f-type process and the density of states $N(E_k \pm \hbar\omega_{ij} - \Delta E_{ji})$ follows Equation 30.

Additionally, Ferry (1976) derived the first-order model shown in

$$\begin{aligned} W(E) = \frac{\sqrt{2}\, m^{*\frac{5}{2}}\, D_1^2}{\pi\rho\omega_0\hbar^5} & \Big[n(\omega_0)\sqrt{E + \hbar\omega_0}(2E + \hbar\omega_0) \\ & + (n(\omega_0) + 1)\sqrt{E - \hbar\omega_0}\sqrt{2E - \hbar\omega_0}\, u_0(E - \hbar\omega_0)\Big], \end{aligned} \tag{36}$$

where D_1 is the first-order deformation potential, ω_0 is the phonon radian frequency and u_0 is the unit step function, defined by $u_0(x) = \begin{cases} 0, & x < 0 \\ 1, & x \geq 0 \end{cases}$.

For nonparabolic bands, alternatively, the zero-order approximation is given by Equation 37, in contrast to Equation 35 for parabolic bands.

$$W(E) = \frac{\pi D_{ij}^2 Z_j}{\rho\omega_{ij}}\left[n(\omega_{ij}) + \frac{1}{2} \mp \frac{1}{2}\right]\left(\frac{(2m_d^*)^{\frac{3}{2}}\sqrt{E_f(1+\alpha E_f)}}{4\pi^2\hbar^3}\right)(1 + 2\alpha E_f) \tag{37}$$

In which $E_f = E_k + \hbar\omega_{ij} - \Delta E_{ji}$ for phonon absorption and $E_f = E_k - \hbar\omega_{ij} - \Delta E_{ji}$ for phonon emission. The optical phonon energy $\hbar\omega_{ij}$ corresponds to the amount of energy the electron absorbs or emits when interacting with the phonon. For silicon, the energy difference ΔE_{ji} is zero, since the six valleys are equivalent.

Since the optical phonon energy $\hbar\omega_0$ is comparable to the carriers average thermal energy at room temperature, optical phonon scattering is considered inelastic. This opposes to the acoustic phonon scattering, in which the phonon energy is much smaller than $K_B T$, therefore leading to elastic scattering.

3.1.3. Ionized Impurity Scattering

When a semiconductor is doped, the Coulomb potential of the ionized impurities may deflect electrons, resulting in the called *Coulomb scattering*. The rate at which this scattering process takes places is directly proportional to the doping density, and increases as the square power of the energy of the electron.

In vacuum, the electrostatic potential due to a point charge is coulombic; the presence of free carriers in the crystal leads to a *screened* potential, i.e., the mobile charge carriers lead to a damping of the electric field. Differing in the screened potential used in the model, the carrier scattering due to this screened potential has been modeled by the Conwell-Weisskopf and the Brooks-Herring approaches (TOMIZAWA, 1993)

In order to obtain the ionized impurity scattering rate, the screened potential in a *n*-type semiconductor is derived. Being e the electronic charge and Ze the charge of the impurity atom, it is supposed that a positive charge $Ze\delta(r)$ is introduced at the origin of the assumed coordinate system, what is indicated by $\delta(r)$. The introduction of a doping atom disturbs the charge neutrality in the vicinity of this point, increasing the electron density by $\delta n = n - n_0$, where n_0 is the equilibrium electron density. The solution of Poisson's equation in spherical coordinates leads to the electrostatic potential as shown in Equation 38,

$$\frac{1}{r^2}\frac{d}{dr}\left(r^2\frac{dV}{dr}\right) = -\frac{e}{\varepsilon_s}[Z\delta(r) - \delta n] \tag{38}$$

being ε_s the semiconductor dielectric constant and r the distance from the origin.

Considering that n_0 is sufficiently low so that it can be modelled by the classical distribution function, so that $\delta n \approx V \frac{e n_0}{k_B T}$, and then using this relation to solve Equation 38, the screened Coulomb potential is obtained as the particular solution:

$$V(r) = \frac{Ze}{4\pi\varepsilon_s r} e^{-\frac{r}{L_D}} \tag{39}$$

where L_D is known as Debye length and is calculated by $L_D = \sqrt{\varepsilon_s V_T / e N_D}$, being V_T the thermal voltage and N_D the density of donors.

The perturbation potential used to obtain the scattering rate is then:

$$H' = \frac{Ze^2}{4\pi\varepsilon_s r} e^{-\frac{r}{L_D}} \tag{40}$$

Using this expression to calculate the matrix element in Fermi's golden rule and considering that the number of ionized impurities per unit volume in the crystal space is given by n_i, the total scattering rate for nonparabolic bands is obtained as

$$W(k) = \frac{\sqrt{2} Z^2 e^4 n_i}{\varepsilon_s^2 \sqrt{m_d^* E_\beta}} \sqrt{E(1+\alpha E)} \frac{1 + 2\alpha E}{1 + 4(\frac{E(1+\alpha E)}{E_\beta})} \tag{41}$$

where $E_\beta = \frac{\hbar^2}{2 m_d^* L_D^2}$.

In the particle-based device simulator presented in this thesis, however, a real-space approach was implemented instead of the momentum-space modelling presented above. Chosen here to model Coulomb iterations, the P^3M approach will be presented in Section 4.1.9.

4 DEVICE SIMULATION

In Chapter 2, carrier transport in bulk semiconductors was evaluated by the numerical solution of the Boltzmann transport equations using the Monte Carlo method. In order to simulate a device, however, the electric field that drives the charge transport must be taken into account by the solution of Poisson's equation. Carrier transport and the driving fields are coupled in device simulation, and must be solved self-consistently. The electric field coming from the solution of Poisson's equation is responsible for the acceleration of the carriers that drift under the Monte Carlo phase, while the charge distribution itself defines the electric fields in Poisson's equation.

Over small time intervals, nonetheless, Poisson's equation may be decoupled from the BTE, simplifying the calculations. During this time interval, the carriers drift driven by the frozen electric field that resulted from the solution of Poisson's equation at the end of the previous time interval, and then the Monte Carlo calculations lead to the charge distribution that, at the end of this time interval, will define the Poisson's equation that provides the fields for the next Δt.

Besides the potential calculation obtained by the solution of Poisson's equation, there is something else that changes from bulk semiconductor simulation to device simulation: instead of being spread in a boundless region, the particles are restricted in a specific region defined by the device boundaries. These boundaries must be suitably defined into the code so that the particles may be reflected at the surface or may exit or enter the device through the terminals.

The structure of the Monte Carlo device simulation will be presented on the next section.

4.1 Simulation Steps

Device simulation can be roughly divided in:

- Initialization of material parameters, device structure and carriers energy, momentum and position;
- Particle-mesh coupling;
- Solution of Poisson's equation;
- Interpolation of force to particle location.
- Monte Carlo free-flight/scattering;

Figure 6 shows the device simulation framework based on the ensemble Monte Carlo method.

Figure 6 - Flowchart for device simulation based on the ensemble Monte Carlo method.

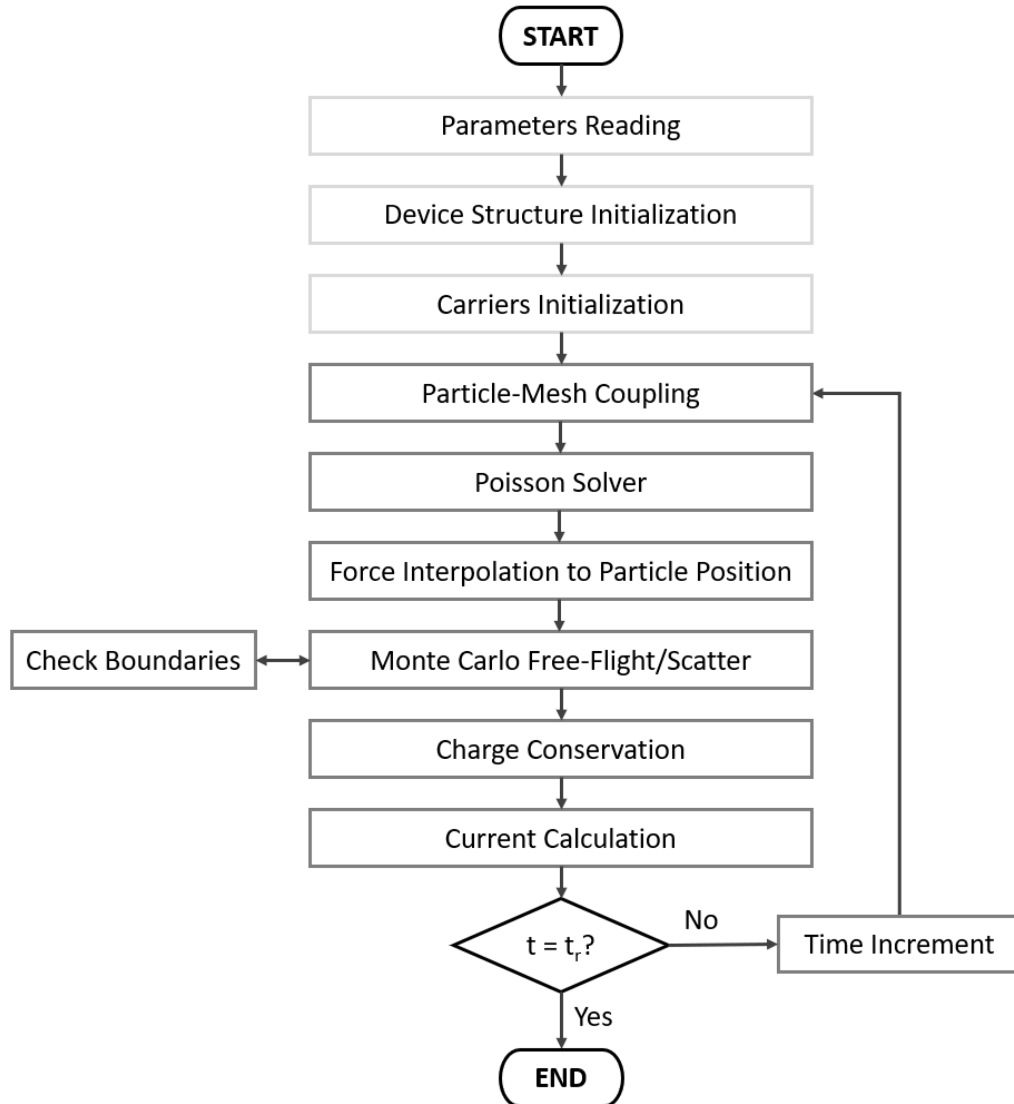

Source: Elaborated by the author

As shown in Figure 6, Monte Carlo device simulation can be divided in three main parts: calculating particle dynamics with appropriate boundary conditions; verifying particles entrance or exit through the device terminals; potential calculation with opportune boundary conditions (TOMIZAWA, 1993). In the following sub-sections, the simulation steps will be presented in the order they are first called in the simulator code.

4.1.1 Material Parameters Initialization

The material parameters that are needed in the many equations that were presented in this work must be inserted in the simulation via an input file. Material parameters such as crystal density, velocity of sound in the crystal, dielectric constant and effective masses are then read by the code.

4.1.2 Mesh size and Time-step

In order to allow stable Monte Carlo device simulation, the mesh size ($\Delta x, \Delta y$ and/or Δz) and the simulation time-step (Δt) must be chosen appropriately, correlating to each other in connection with the numerical stability. While Poisson's equation is solved *at* every Δt, the particle dynamics ruled by the Monte Carlo algorithm takes place *during* this small time-step.

The *mesh size* defines the spatial resolution of the potential and is therefore determined by the charge variations. In order to be sensitive to these fluctuations, the mesh size must be smaller than the smallest wavelength of the charge variations, which is approximately equal to the Debye length (L_D), expressed as

$$L_D = \sqrt{\frac{\varepsilon_s \, K_B T}{e^2 n}}, \tag{42}$$

being ε_s the material dielectric constant, K_B the Boltzmann constant, T the carrier temperature, e the magnitude of the electronic charge and n the carrier density. The mesh size in the simulation must be chosen to be smaller than L_D, so that relevant information on the potential profile is not lost, but it cannot be too small so that it troubles the Poisson solver convergence. The mesh size can also be changed by the user accordingly to the device size - smaller devices can have a smaller grid, and larger devices can have proportionally bigger mesh size.

The largest stack of computational cost of a Monte Carlo 3D device simulator is the solution of Poisson's equation, being the Monte Carlo method itself a lot less time-consuming. The mesh size influences Poisson's equation solver directly, so that it must be chosen wisely. A strategy that may be employed in order to reduce computational cost is to use a non-uniform mesh, which has a larger size where precision is not needed, like in the semiconductor substrate, leaving the smaller mesh size only for the regions that demand high simulation precision, as in the device conduction channel or in the specific region where a phenomenon is being studied. Even though it changes depending on the device characteristics, typical values for the mesh size may range around 2 nm.

In order to be able to decouple Poisson's equation from BTE, the simulation time-step must be suitably small. From the viewpoint of stability criterion, this can be assured by making the time-step Δt smaller than the inverse of the plasma frequency, i.e.,

$$\Delta t \ll \frac{1}{\omega_p} \tag{43}$$

where the plasma frequency ω_p is given by

$$\omega_p = \sqrt{\frac{e^2 n}{\varepsilon_s m^*}} \tag{44}$$

being m^* the effective mass of the carrier. If the modeled semiconductor has multiple valleys, the smallest effective mass that a carrier may experience must be taken into account in Equation 44. Although it changes depending on the device characteristics, typical values for the time step may range around 0.1 fs.

Even though the mesh-size and the time-step were defined separately, they must be self-consistent; this can be checked by evaluating the maximum distance the carriers can move during Δt, which is regarded as l_{max} and is written as

$$l_{max} = v_{max}\, \Delta t\,, \tag{45}$$

in which v_{max} is the maximum carrier velocity, approximated as the maximum group velocity of the carriers in the semiconductor.

The time-step must be chosen to be small enough to make l_{max} smaller than the spatial mesh size estimated using equation 42. Since Poisson's equation is only solved at every Δt, the fields are updated only at these moments, and a too large time-step might lead to an unaccounted substantial change in the charge distribution.

4.1.3 Device Structure Description

The device must be described in the simulator by defining the boundary conditions, which enter the simulation in the Monte Carlo particle dynamics and in the numerically solved Poisson's equation. All the design options are defined, such as the device type (such as MOSFET, MESFET, FinFET) and the optional addition of characteristics like high-k dieletric, that affect the semiconductor device operation.

Except for the four MOSFET terminals, the surfaces are defined by mirror boundary conditions. The boundaries are then assumed to perfectly reflect the particles that reach them,

reversing the velocity component normal to the surface when the carriers collide against the surface. The Neumann condition of zero electric field in the direction normal to the surface is then applied to Poisson's equation analysis.

The drain and source contacts are treated as particle reservoirs, and the carriers may enter or exit the device through these terminals. Regarding Poisson's equation, the contacts are considered Dirichlet boundaries where the bias voltages are applied. If a carrier crosses the device border in a contact, it is accounted for to calculate the current.

4.1.4 Metal Grain Granularity

Since metal grain granularity (MGG) is a relevant source of variability in FinFETs (WANG, 2011; NAGY, 2017; SUDARSANAN, 2019), it is mandatory to include its effects in the simulator.

The MGG modelling approach which was used in the code is the one presented in (VARDHAN, 2017). First, the grains and their characteristics must be defined. The average grain size (Ag) is defined according to the metal gate material, ranging from 5 to 20 nm. The expected number of grains (E[Ng]) is calculated for each metal gate plane as the ratio between the surface area (SA) and the average grain size, i.e., E[Ng] = SA/Ag. The number of grains is drawn from a Poisson distribution. The position of each grain is randomly selected from a uniform distribution in the 2-D plane of the metal gate. For each grain, the work function (WF) is randomly selected according to the WF values and their occurrence probabilities depending on the metal gate material. Lastly, the grains must be assigned to the grid, in order to define the WF value on each mesh cell. For each grid node in the gate, the distance to each grain in the plane is calculated, and the WF value from the closer grain is assigned to the node. The process is repeated for each metal gate surface.

4.1.5 Dopant Distribution

The doping atoms are randomly placed in the appropriate regions of the device. The expected number of dopants that would belong to a certain region is calculated by its volume and doping density. The actual number of doping atoms in each region is then randomly picked from a Poisson distribution whose mean is the number previously calculated from the volume and doping density.

4.1.6 Carrier Initialization

Opposing to what happens in the bulk Monte Carlo method, the initial number of carriers and their location is not arbitrary, being the former defined so that initial charge neutrality is assured in the device by balancing the dopant ions, and the latter is defined by the equilibrium solution of Poisson equation. Similarly to the bulk Monte Carlo method, however, the energy and the momentum of each carrier are obtained respectively by the Boltzmann distribution and the generation of a random *k*-vector that matches the energy condition, as discussed in Section 2.1.1.

4.1.7 Monte Carlo Routine

The Monte Carlo method is applied as discussed in Chapter 2, following a free-flight and scattering loop. The difference now is that the semiconductor is no longer physically unlimited, so that the device boundaries must be respected. The boundaries must be checked at each step so that no carrier enters the oxide or leaves the device through its borders.

4.1.8 Balance of Drain and Source Contacts

It is important to check if drain and source contacts are balanced, i.e., if the same number of charges that enter one contact leave the other, maintaining charge conservation. At each step, electrons may be included to balance the number of dopants on the cells on the vicinities of the contacts. The particles are deleted when they leave the contacts naturally. The charge balance is evaluated in the group of cells near each contact as a whole, not cell by cell.

4.1.9 Particle-Mesh Coupling

While Poisson's Equation is solved on specific grid points, the Ensemble Monte Carlo method evaluates particle motion under continuous space coordinates. In order to make both components compatible, a particle-mesh (PM) coupling method is needed for both particle assignment to a mesh point and force interpolation. The PM coupling is compound of the assignment of the particle to the mesh, Poisson's equation solution on the mesh, calculation of the mesh-defined forces, and interpolation to define the forces on the particle.

In order to assign the charges along the corners of the mesh cell, there are three main particle-mesh methods, shown in Figure 7: nearest-grid-point (NGP), nearest-element-center (NEC) and cloud-in-cell (CIC).

Figure 7- Representation of Different Particle-Mesh Methods

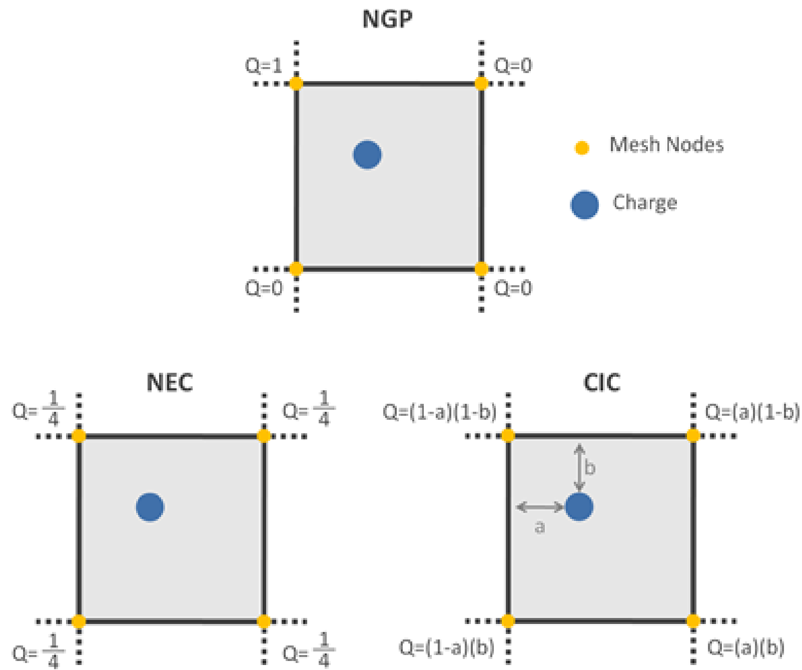

Source: Elaborated by the author

In the NGP method, the charge is assigned to the nearest grid point. It is the simplest PM method, but it leads to a noisy charge distribution, what can affect numerical stability. The NEC method considers that the charge is equally distributed in the four grid points that limit the cell. The CIC method leads to the most precise alternative, since the charge distribution to each corner is made proportionally to its distance from it.

4.1.10. Particle-particle-particle-mesh (P^3M) Algorithm

In order to properly simulate particle dynamics, all the relevant scattering mechanisms must be taken into account, including carrier-carrier and carrier-ion interactions. The scattering rates used in the Monte Carlo algorithm are typically calculated in *k*-space; in the past, it was common to model Coulomb interaction that way, using the Brooks-Herring approach, but it led to double counting of the force, as well as frequently other problems like faster thermalization of the carriers at the drain end of the device, disregard of multi-ion contributions to the scattering potential and of dynamical perturbations to the Coulomb fields resulting from carrier movement. There was also need of knowledge of the noisy and time-varying local distribution function, so that the scattering rates had to be constantly reevaluated during the simulation, what took away the convenience of the one-time calculated scattering tables (AHMED, 2005). Since the *k*-space analysis of Coulomb scattering leads to many

inconveniences, real-space molecular dynamics approaches for this scattering mechanism have been developed, such as the particle-particle-particle-mesh (P^3M) coupling method (HOCKNEY; EASTWOOD, 1988), the fast multipole method (GREENGARD; ROKHLIN, 1997) and the corrected Coulomb forces approach (GROSS; VASILESKA; FERRY, 1999), being the first method the one addressed in this work.

The *particle-particle-particle-mesh* algorithm is one of the three principal models of particle simulation, being a hybrid of the other two: the *particle-particle* (PP) model, that uses the force law to obtain the forces of interaction and the equations of motion to obtain the state of the system (particle positions and velocities) for a certain time, and the *particle-mesh* (PM) model, that treats the force as a field quantity approximated on a mesh - the charge is assigned to a mesh, where Poisson's equation is then solved, followed by the computation of the mesh-defined potential and its interpolation to the actual particle positions. While the PP model is suitable for small systems with long-range forces or for large systems with only a few interparticle distances that result in nonzero forces of interaction, the PM method can have a significant reduction on computational costs, at the expense of loss of resolution in the potential and force fields, so that it is appropriate only for smoothly varying forces. The P^3M method combines the advantages of the PP and PM models, allowing the simulation of large correlated systems with long-range (such as coulombic) forces (HOCKNEY; EASTWOOD, 1988).

The basic idea of the P^3M method is to split the interparticle forces into two components: a *short range* part, which is nonzero only for particle separations smaller than a certain cutoff radius and is computed by direct particle-particle pair force summation, and a *long-range* part, that varies smoothly and is calculated by the particle-mesh method. Equation 46 shows that the total force on particle i can be split in the direct forces of particles j on particle i in the short-range domain (SRD), corresponding to the first sum, and in the mesh forces of particle j on particle i in the global problem domain (GD), including the effect of material boundaries and boundary conditions on particle i, corresponding to the second sum (AHMED, 2005).

$$\boldsymbol{F_i} = \sum_{\substack{j \neq i \\ SRD}} \boldsymbol{F_{ij}}^{\boldsymbol{sr}} + \sum_{\substack{j \neq i \\ GD}} \boldsymbol{F_{ij}}^{\boldsymbol{m}} \quad (46)$$

Where $\boldsymbol{F_{ij}}^{\boldsymbol{sr}}$ is the short-range Coulomb force of particles j on particle i and $\boldsymbol{F_{ij}}^{\boldsymbol{m}}$ is the long-range mesh force of particles j on particle i.

The short-range Coulomb force can be written as

$$\boldsymbol{F_{ij}}^{sr} = \boldsymbol{F_{ij}}^{coul} - \boldsymbol{R_{ij}} \tag{47}$$

where $\boldsymbol{F_{ij}}^{coul}$ is the force of particle j on particle i, given by Coulomb's law,

$$\boldsymbol{F_{ij}}^{coul} = \frac{\boldsymbol{q_i q_j}(\boldsymbol{r_i} - \boldsymbol{r_j})}{4\pi\varepsilon|\boldsymbol{r_i} - \boldsymbol{r_j}|^3}, \tag{48}$$

where q_i and q_j are particle charges and r_i and r_j are particle positions.

The variable $\boldsymbol{R_{ij}}$ is a reference force that avoids double counting of the forces of the SRD and GD, being equal to the mesh force within the short-range domain and to the Coulomb force outside the short-range domain. The Coulomb force is kept restricted to the SRD, where the reference force goes smoothly to zero, and outside the short-range domain cutoff radius ($\boldsymbol{r_{sr}}$), the force is kept equal to the mesh forces, so that the reference force corresponds to the point particle force law.

In order to integrate P^3M with the EMC method to account for carrier-carrier and carrier-impurity interactions for uniform meshes, Wordelman and Ravaioli (2000) followed Hockney's approach and obtained the reference forces used on this work, shown in Equation 49.

$$\boldsymbol{R_{ij}}(r) = \frac{\boldsymbol{q_i q_j}}{4\pi\varepsilon}\, x$$

$$x \begin{cases} \dfrac{1}{35\boldsymbol{r_{sr}}^2}(224\xi - 224\xi^3 + 70\xi^4 + 48\xi^5 - 21\xi^6) & 0 \le \boldsymbol{r} \le \boldsymbol{r_{sr}}/2\,. \\ \dfrac{1}{35\boldsymbol{r_{sr}}^2}\left(\dfrac{12}{\xi^2} - 224 + 896\xi - 840\xi^2 + 224\xi^3 + 70\xi^4 - 48\xi^5 + 7\xi^6\right) & \boldsymbol{r_{sr}}/2 \le \boldsymbol{r} \le \boldsymbol{r_{sr}} \\ \dfrac{1}{\boldsymbol{r}^2} & \boldsymbol{r} > \boldsymbol{r_{sr}}. \end{cases} \tag{49}$$

where $\boldsymbol{r}$ is the interaction radius and $\xi = 2r/r_{sr}$.

4.1.11. Poisson's Equation Solver

Monte Carlo device simulation requires the potential profile, which is obtained as the solution of Poisson equation, given by

$$\nabla.(\varepsilon_s \nabla\psi) = -\rho \tag{50}$$

where ψ is the electric potential, ρ is the free charge density and ε_s is the material permittivity. The 3D case is solved using the strongly-implicit method (STONE, 1968), so that the potential distribution along the device is found.

4.2 N-MOSFET Implementation Overview

The PMOS Monte Carlo device simulator previously developed by Camargo (2016) in collaboration with Prof. Dragica Vasileska's group in Arizona State University (ASU) was used as the basic structure for the development of a NMOS device simulator. In order to adapt the code to n-channel MOSFETs, initially a n-type bulk-Si Monte Carlo code was implemented. The NMOS device simulator was then obtained by combining the basic bulk-Si properties to the proper boundary conditions and to the Poisson equation solution structure of the PMOS code. Using the theoretical framework presented in Chapters 2, 3 and 4, the adaptation of the original PMOS to a NMOS device simulator required several, far-reaching changes and/or insertions in the code, including:

- Boundary conditions, such as electric potential on the source, drain, gate and back contacts and also on the silicon;
- Electron initial and updated positions after each iteration;
- Doping;
- New modelling of the scattering mechanisms – random selection and new equation of the different scattering rates for each scattering mechanism
- Scattering tables;
- Charge distribution and conservation;
- Band structure for n-type silicon;
- Electron velocity calculation;
- Momentum/energy relation;
- Different valley velocity calculation;
- All Monte Carlo loop with new effective masses and different material characteristics;
- Initial electron distribution in three different valleys, both in space and regarding their initial energy.

In general, those changes appear or echo in many different locations on the code and need to be changed in a self-consistent, cohesive manner.

4.3 N-FinFET Implementation Overview

The expansion from planar to tridimensional transistors leads to several changes and new needs on the code. First, the transistor geometry and the materials that constitute each region of the device were changed, impacting significantly the boundary conditions and therefore the numerical solution of the Poisson equation which, coupled with the BTE, compose the semiconductor device simulation. New variables were inserted and read to define dimensions, materials and transistor characteristics.

The alteration of the structure geometry affects many simulation blocks, which demand corrections and must be readapted. It is necessary, for instance, to adapt the subroutines regarding initial potential, doping, velocity, and energy calculation. The carrier positions at the beginning of the simulation, after the equilibrium condition (voltage different from zero applied only at the gate electrode), and at each iteration must be properly accounted for.

Regarding the definition of the materials on the 3-D device, the changes on the gate oxide and on the contacts may be highlighted. In order to simulate tridimensional charge transport, oxide was inserted on the sides of the MOS transistor, allowing the creation of lateral channels, which add to the traditional top channel of planar transistors. Aiming to simulate the behavior of devices which have high-k gate dielectrics, silicon oxide with equivalent thickness to the high-k material was used to isolate all channel regions from the gate metal.

The device contacts were adapted through the addition of source and drain contacts on the fin sides, creating the side channels. The gate contacts were altered from the original poly-Si on planar device to metal gate on the 3-D transistor. In order to achieve that, the work function (W_m) of the metal gate and the electron affinity (X_{sc}) were used to calculate the electric potential $\phi(i,j,k)$ on the contacts through a new equation to the gate contacts on the 3-D space:

$$\phi(i,j,k) = \frac{V_g}{V_t} + dE_c + \frac{X_{sc}}{V_t} - \frac{W_m}{V_t} \tag{51}$$

On which $V_t = {}^{kT}/_{q}$ is the thermal voltage, being k the Boltzmann constant, T the temperature and q the fundamental charge.

Moreover, changes were made on the subroutine that verifies if a carrier is crossing a border, i.e., leaving the silicon area. Typically, the boundaries act as mirrors; if, after a

simulation step, a carrier would be located outside silicon after the drift determined by the Monte Carlo section, it is reflected inside the semiconductor, with the same momentum magnitude, but in the opposite direction. When, alternatively, the carrier crosses the border in a contact region, its exit is accounted for and considered on the device current calculation. Finally, if a carrier crosses a frontier between the semiconductor and the gate oxide, it may undergo surface scattering or be reflected specularly, depending on the surface scattering rate. For a tridimensional device, the complexity of boundary checking increases substantially, due to the necessity of considering the different possibilities by which a carrier could leave the device in three dimensions, on the top and side channels.

The mesh on which the fields are calculated and the Poisson equation is solved also needed to be adapted to the tridimensional structure. The volume of each cell was correspondingly adapted to consider the new device boundaries, that introduce changes on size between the cells.

Additional alterations were performed on the charge conservation subroutine, which assures the charge neutrality on the vicinities of the contacts at each simulation step. Another relevant alteration was the inclusion of directional injection of carriers.

5 BULK SILICON MONTE CARLO SIMULATION RESULTS

The bulk ensemble Monte Carlo particle dynamics simulator was implemented and some simulations were performed in order to verify its correctness. Silicon was chosen as the semiconductor material, and it was modeled as a three valley semiconductor. In all the simulations, 20000 carriers were simulated, divided into 1000 possible energy levels, and temperature was set to 300 K. The electric field was applied in the [111] direction, being equally divided into the three coordinate components.

The scattering tables were obtained from the scattering rate equations shown in Chapter 3 and were implemented in the bulk simulator. The intravalley acoustic phonon scattering (Figure 8), intervalley zero-order *g* and *f* non-polar optical phonon scatterings (Figure 9) and Coulomb scattering were considered in the code.

Figure 8 - Acoustic scattering rate for silicon.

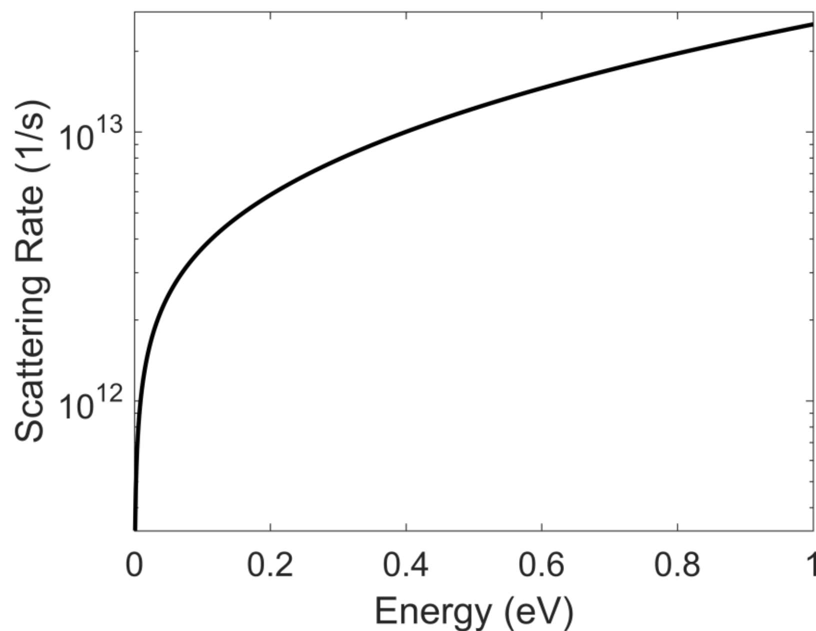

Source: Elaborated by the author

Figure 9 - Non-polar optical scattering rate for silicon.

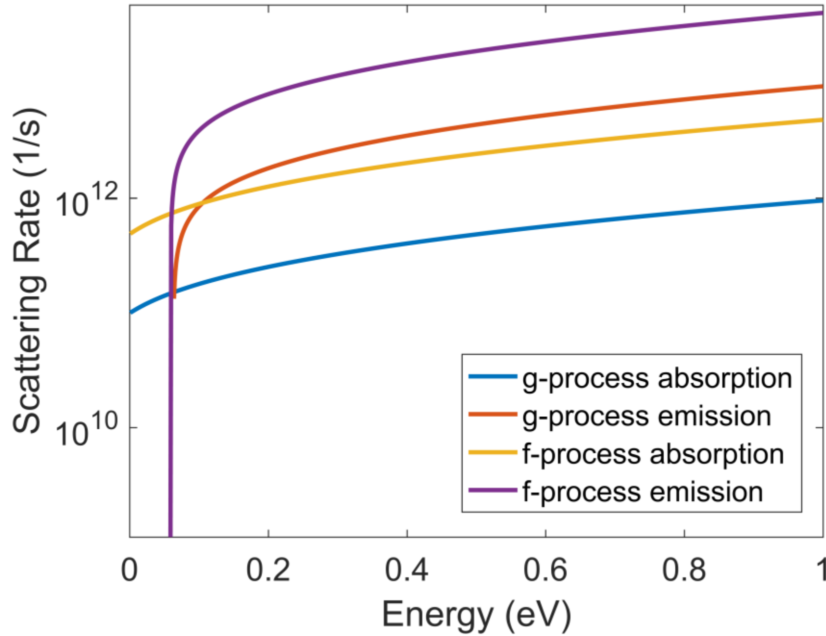

Source: Elaborated by the author

The transient and steady state drift velocities of electrons and their energy over time were calculated using the simulator. Since a three-valley semiconductor model was used, the output files registered the velocity in *x, y* and *z* axis for the three valleys, i.e., v_{x1}, v_{x2} and v_{x3}, v_{y1}, v_{y2} and v_{y3}, , v_{z1}, v_{z2} and v_{z3}. Assuming the occupation of valleys labeled as *1, 2* and *3* is given by n_1, n_2 and n_3, the final velocity at *x, y* and *z* is pondered by the valley occupation and given by

$$v_a = \frac{v_{a1}n_{1+}v_{a2}n_{2+}v_{a3}n_3}{n_1 + n_2 + n_3} \ , a = x, y \ or \ z \ . \tag{52}$$

The magnitude of the velocity is then given by

$$v = \sqrt{v_x{}^2 + v_y{}^2 + v_z{}^2}. \tag{53}$$

The mean valley occupation is the same for the three valleys when the field is applied to the [111] direction, but it varies from valley to valley if the field is not applied equally between them. If the electric field magnitude is different at each coordinate, the valley occupation is proportional to the magnitude, i.e., stronger fields lead to higher valley occupation; if the field is applied in the [010] direction, for example, the valley occupation is

larger in the y direction. Considering the electron longitudinal mass ($m_l = 0.91$) is bigger than the transverse mass ($m_t = 0.19$), and knowing that the valleys are represented by ellipsoids aligned with the coordinate axis, as shown in Figure 5, and that the valleys labeled as *1, 2* and *3* have each their longitudinal axis along *x, y* and *z*, respectively, the electrons that are located in a valley whose longitudinal axis is aligned with the stronger field have a higher effective mass and then gain less velocity. A possible explanation for the unequal valley occupation for unequal field application is that the carriers that are located on the valleys aligned with the stronger field gain less energy due to the smaller velocity, and then take longer to suffer a scattering, staying in this valley for a longer time.

Figure 10 shows the drift velocity over time for different electric fields that range from $5.5x10^4$ V/m to $5.5x10^6$ V/m.

Figure 10 - Electron drift velocity over time

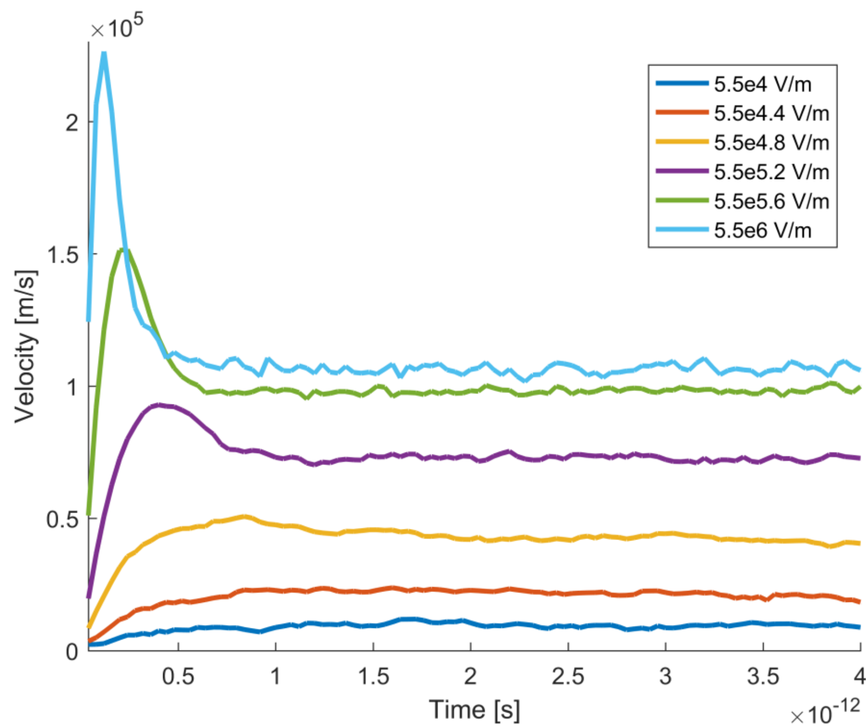

Source: Elaborated by the author

From Figure 10, velocity overshoot is verified for sufficiently high electric fields, as expected. It also evinces the fact that higher electric fields lead to higher velocities.

The results for electron energy over time are presented in Figure 11. As expected, high electric fields lead to higher electron energy.

Figure 11 - Electron energy *vs* time

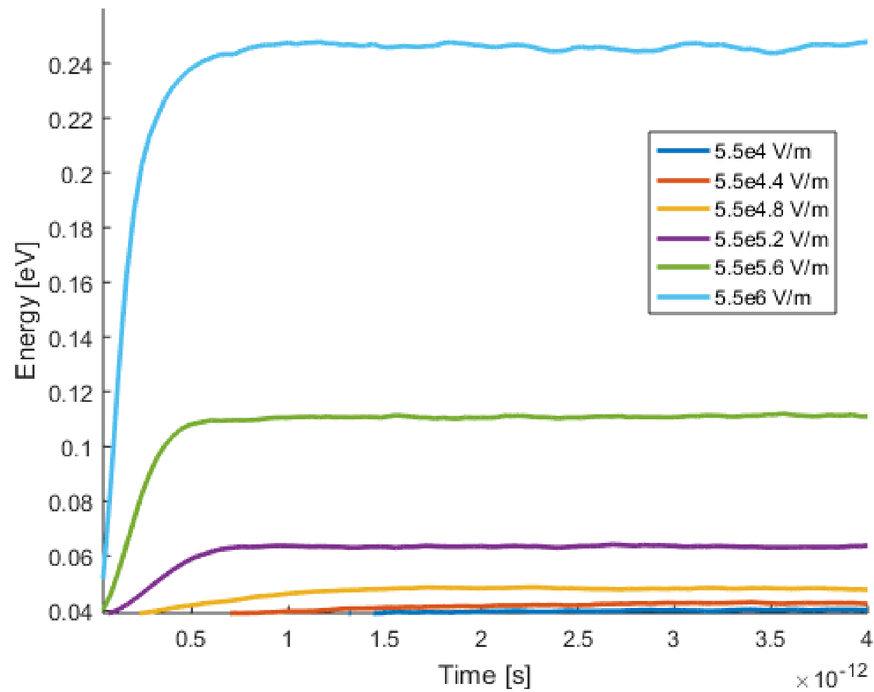

Source: Elaborated by the author

The relation between the velocity and the electric field is shown in Figure 12, and the dependence of energy with the field is shown in Figure 13.

Figure 12 - Velocity dependence on electric field

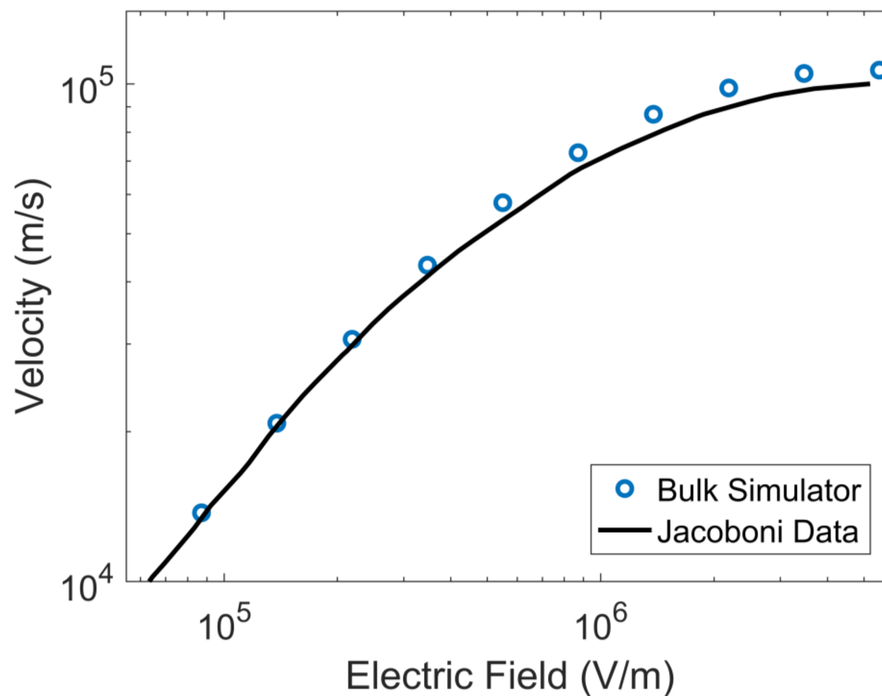

Source: Elaborated by the author

Figure 13 - Energy dependence on electric field

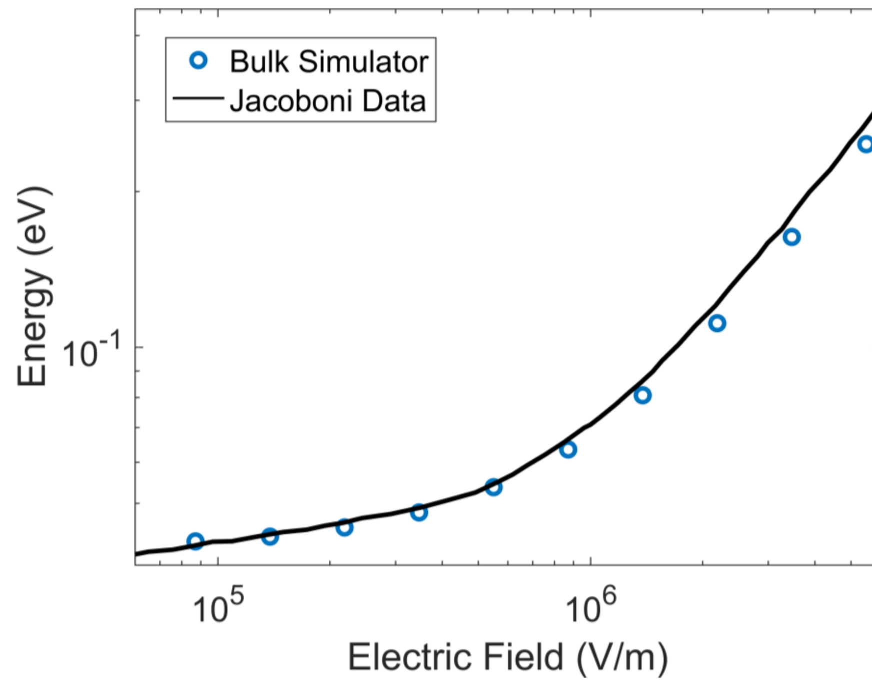

Source: Elaborated by the author

The carriers velocity and energy are in good agreement with the experimental data of Canalli (1975) and the simulation results of Jacoboni (1977).

6 N-MOSFET DEVICE SIMULATION RESULTS

The bulk silicon simulator was expanded to a device simulator that allows the simulation of n-type MOSFET. The device simulated is a planar silicon *n*-MOSFET, with doping densities of $N_A = N_D = 10^{19}$ cm^{-3}, device length of 72 nm, device depth and width of 105 nm, oxide (SiO_2) thickness of 1.2 nm, and source and drain junction depths of 15 nm. The simulation time step was of 0.1 fs. The gate contact is made of polysilicon, and the drain, source and bulk contacts are metallic. The device length is considered to be in the source-drain direction, i.e., along the device channel length, the device depth is in the oxide-bulk direction and the device width is in the channel width direction. Simulation results at 300 K regarding different aspects, such as charge conservation, carriers velocity and energy, electric current, carrier density and electric potential, will be addressed in the next sections.

6.1 Charge Conservation

In order to assure charge conservation, the number of electrons that enter the source contact must be equal to the number of electrons that leave the drain contact, assuming there are no gate and body currents. The number of carriers that passes through the source and drain contacts during a 3 ps simulation was verified, and the results are shown in Figure 14.

Figure 14 - Charge flow through source and drain contacts

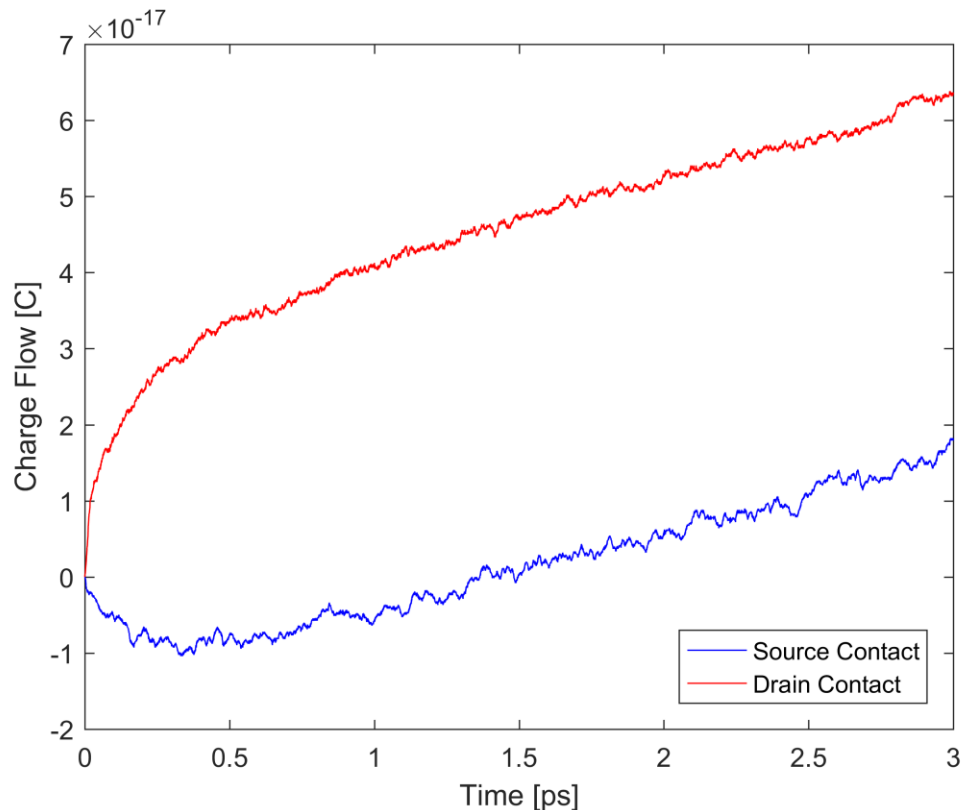

Source: Elaborated by the author

After reaching steady state, the source and drain curves are parallel, which means that the derivative of the cumulative charge in the source and drain contacts have the same absolute value, confirming the charge conservation.

6.2 Carrier Velocity and Energy

The average carriers energy and average velocity on the axis along the device channel length direction were simulated for $V_G = V_D = 1.1\ V$, with source and bulk grounded, and the results are shown in Figures 15 and 16. The source region extends on the device length direction from 0 nm to 18 nm, with contacts from 0 nm to 12 nm, and the drain region goes from 54 nm to 72 nm, with contacts from 60 nm to 72 nm. The channel is in the region between 18 nm and 54 nm on the device length direction. In order to evaluate the variability, Figs. 15 and 16 show the behavior of 40 different devices in different colors, and the average is presented in black.

Figure 15 - Dependence of carrier energy with position along the device length.

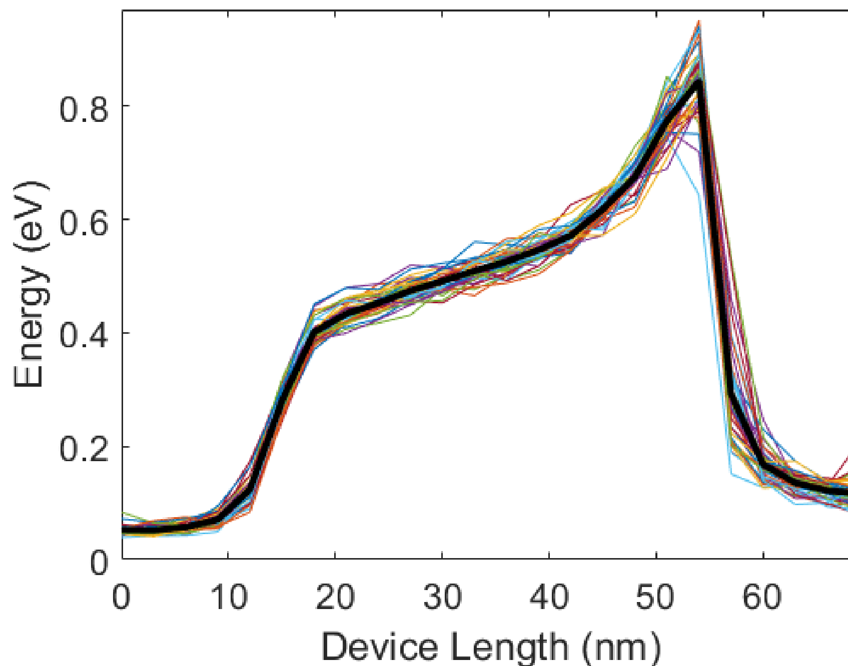

Source: Elaborated by the author

Figure 16 - Dependence of carrier velocity on direction along the device length with their position along this axis.

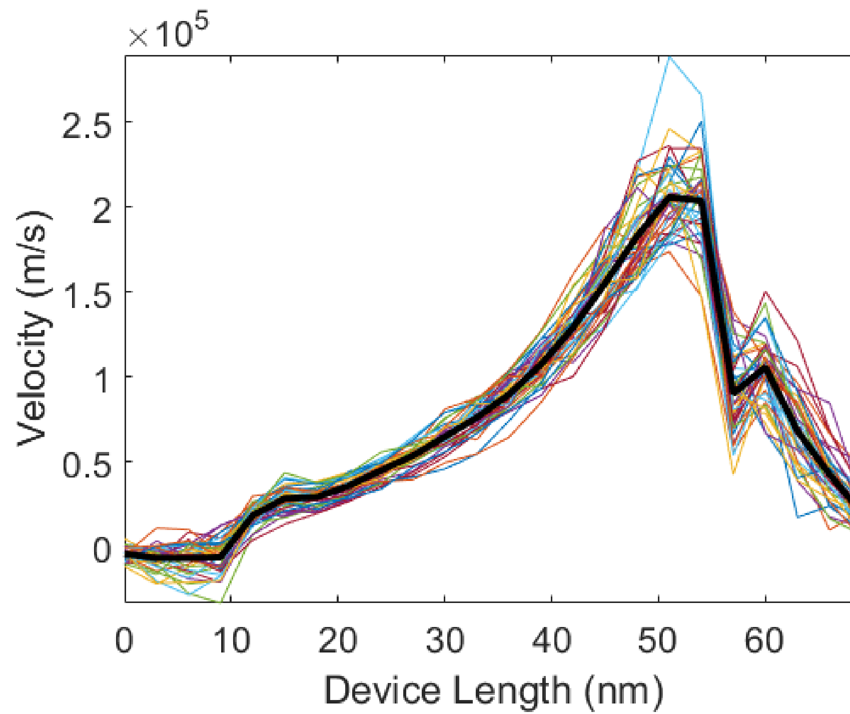

Source: Elaborated by the author

The energy and velocity curves follow the expected shape, with both quantities increasing along the channel, so that the carriers reach their maximum energy and maximum velocity in the channel region near the drain.

6.3 Drain Current *vs* Gate and Drain Voltages

In order to verify that the current dependence on gate and drain voltages matches the traditional MOSFET current curves, the device was simulated for different bias conditions.

For the $I_D\ x\ V_G$ curve, shown in Figure 17, the drain voltage was set to 0.3 V and the source and bulk voltages to 0 V.

Figure 17 - Drain current *vs* gate voltage for V_D = 0.3 V.

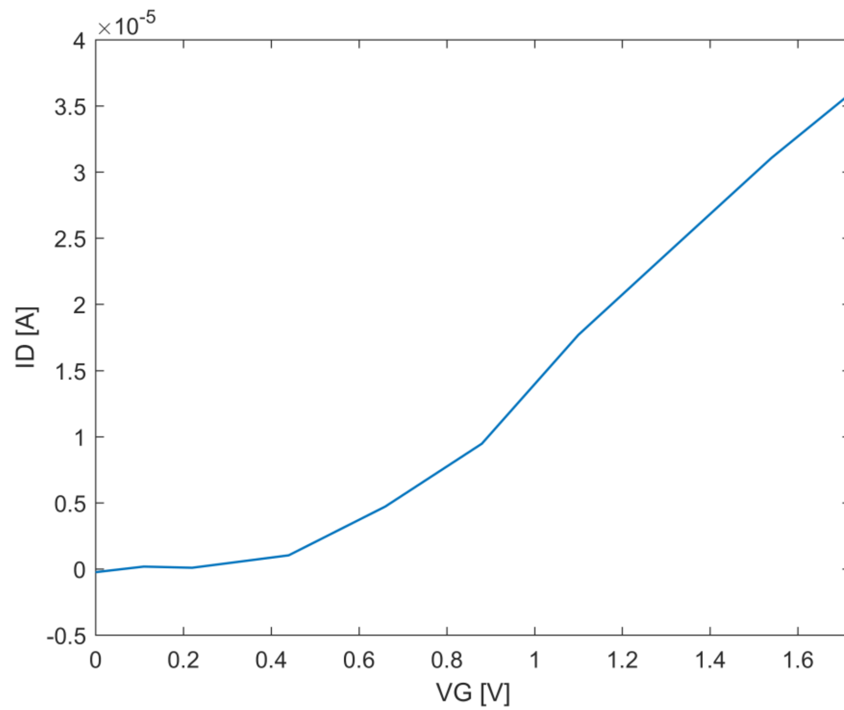

Source: Elaborated by the author

The drain current *vs* drain voltage was simulated for V_G = 1.1 V, to assure that the channel was already formed. The values are shown in Figure 18.

Figure 18 - Drain current *vs* drain voltage for V_G=1.1 V.

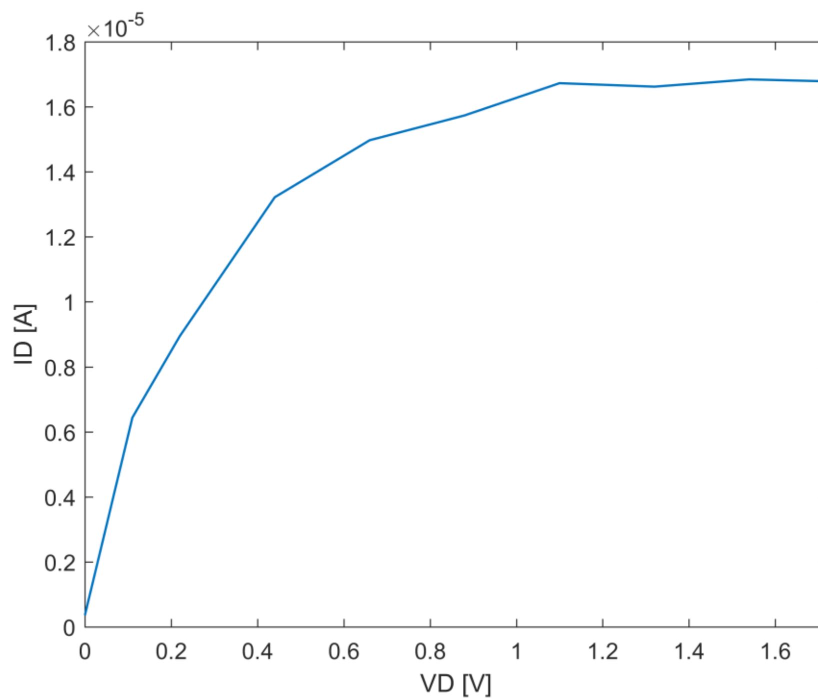

Source: Elaborated by the author

Figure 18 shows current saturation for V_D higher than approximately 1 V.

6.4 Electric Potential

The electric potential was plotted along the device length and device depth directions, as shown in Figure 19 and Figure 20, for equilibrium condition ($V_G = 1.1$ V, $V_D = V_S = V_B = 0$ V) and after the 3 ps simulation ($V_G = V_D = 1.1$ V, $V_S = V_B = 0$ V) respectively. The cut on the W direction was made in the middle of the channel, i.e., W = 52.5 nm. The simulated mesh size of 3 nm was also used on the plots, and the dimensions are expressed in *nm*.

Figure 19 - Electric potential along device length and depth for $V_G = 1.1$ V, $V_D = V_S = V_B = 0$ V.

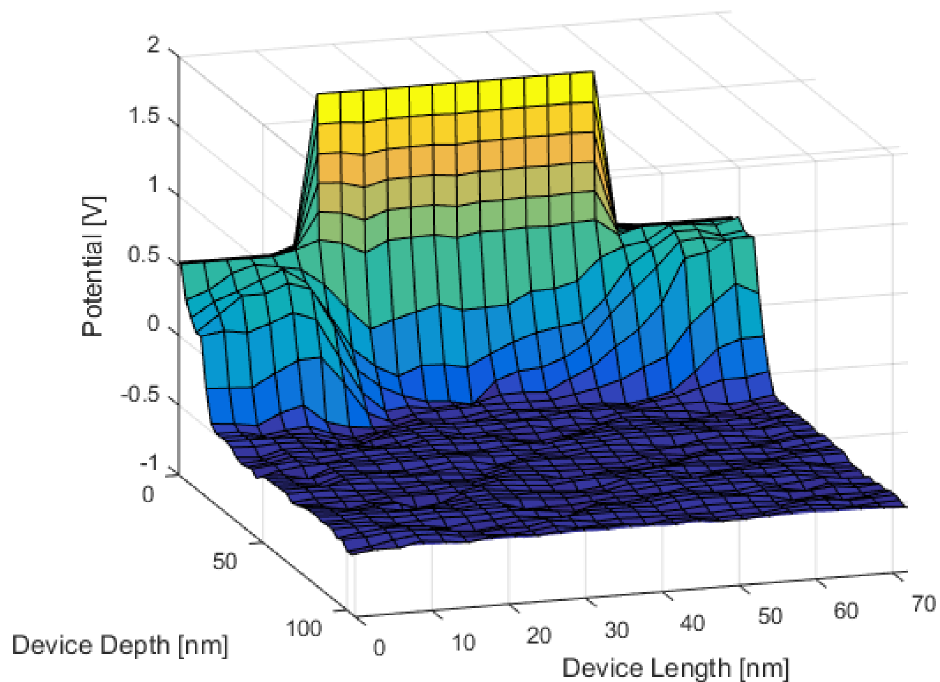

Source: Elaborated by the author

Figure 20 - Electric potential along device length and depth after 3 ps simulation for $V_G = V_D = 1.1$ V, $V_S = V_B = 0$ V.

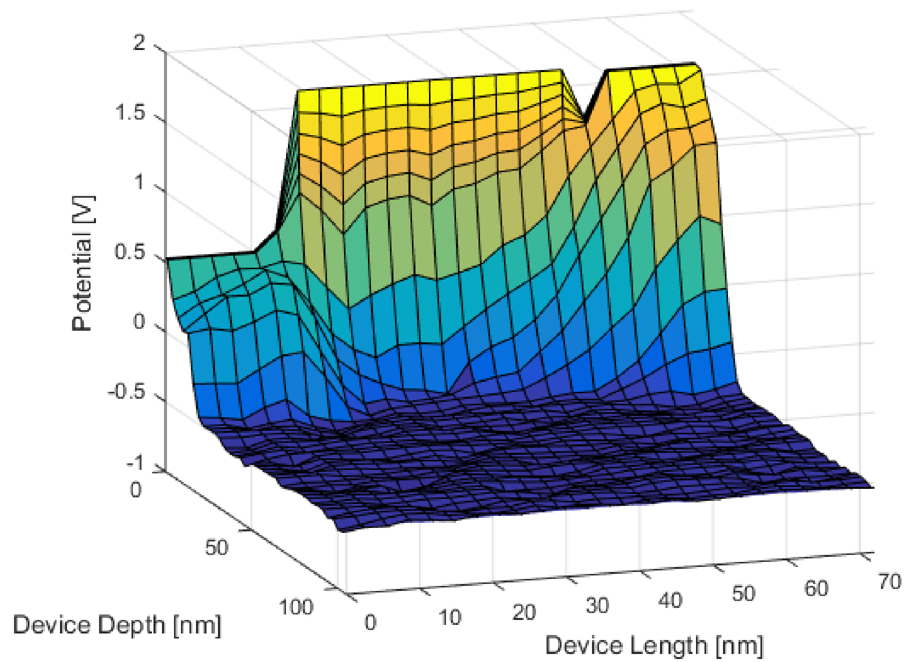

Source: Elaborated by the author

It is possible to see in Figure 19 that, for the equilibrium condition, the source and drain contacts are at the same potential, and the central part of the device is at higher potential, due to the bias applied to the gate. After the voltage is applied to the drain contact, the drain potential rises accordingly, as shown in Figure 20.

The electric potential was also plotted as a function of the position in the direction of device *width* and length. Figure 21 displays the results for equilibrium condition, clearly showing the presence of fluctuations due to random dopants.

Figure 21 - Electric potential along device length and width for V_G = 1.1 V, V_D = V_S = V_B = 0 V.

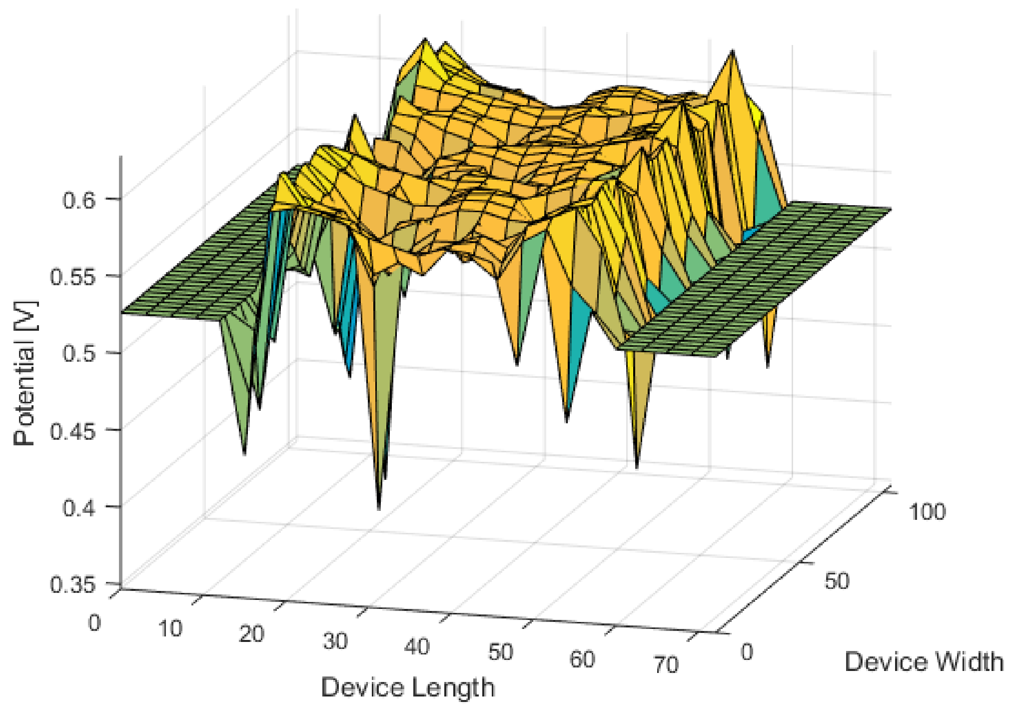

Source: Elaborated by the author

The results obtained after the application of drain voltage V_D = 1.1 V are shown in Figure 22.

Figure 22 - Electric potential along device length and width after 3 ps simulation with $V_G = V_D =$ 1.1 V, $V_S = V_B = 0$ V.

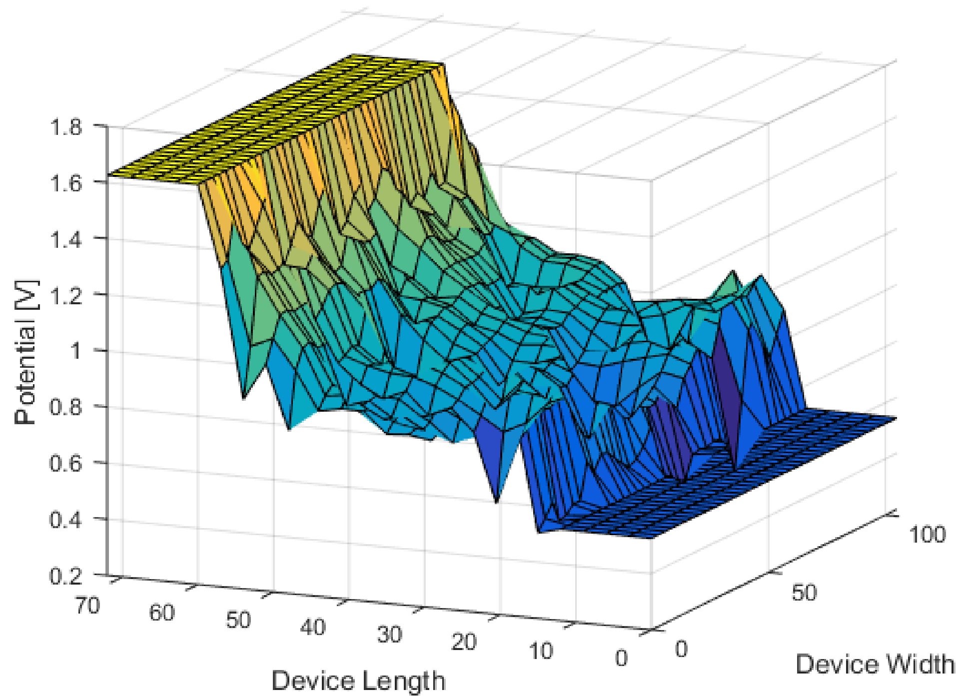

Source: Elaborated by the author

6.5 Carrier Densities

The channel formation can be verified by plotting the electron density along the channel for the equilibrium condition. Figure 23 and Figure 24 show, respectively, the carrier density along the channel for different positions in the device depth and width directions, with $V_G = 1.1$ V and $V_D = V_S = V_B = 0$ V. Since the gate oxide is 1.2 nm thick, the channel interface is located at 1.2 nm in the device depth direction. The dimensions are expressed in *nm*.

Figure 23 - Electron density [m^{-3}] along device length and depth for equilibrium condition.

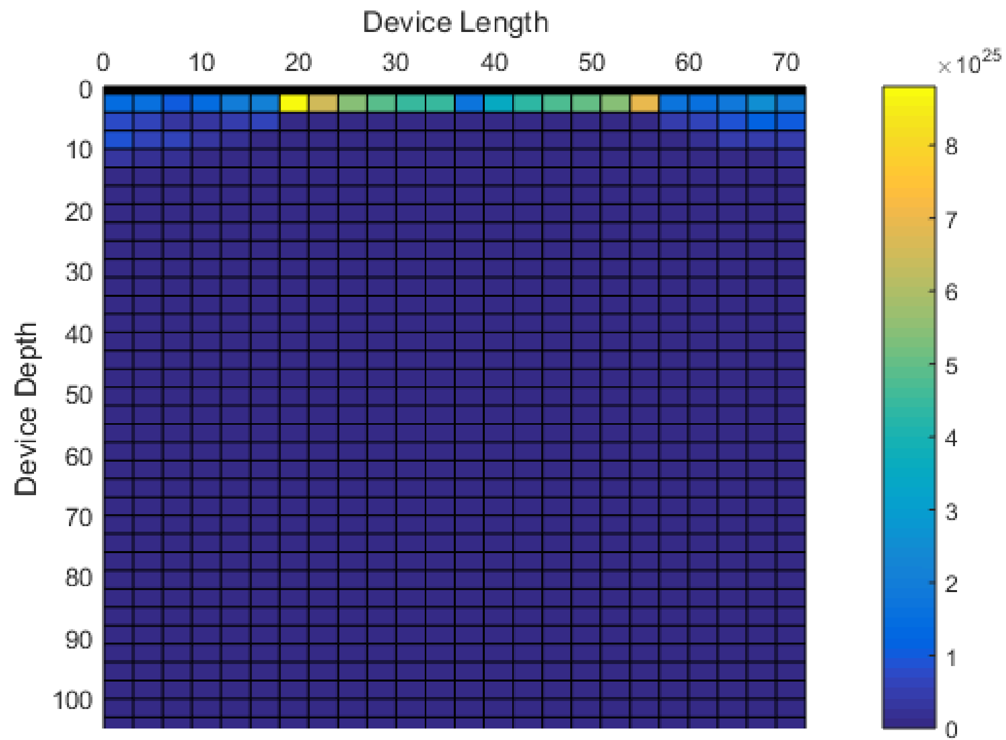

Source: Elaborated by the author

Figure 24 - Electron density [m^{-3}] along device length and width for equilibrium condition.

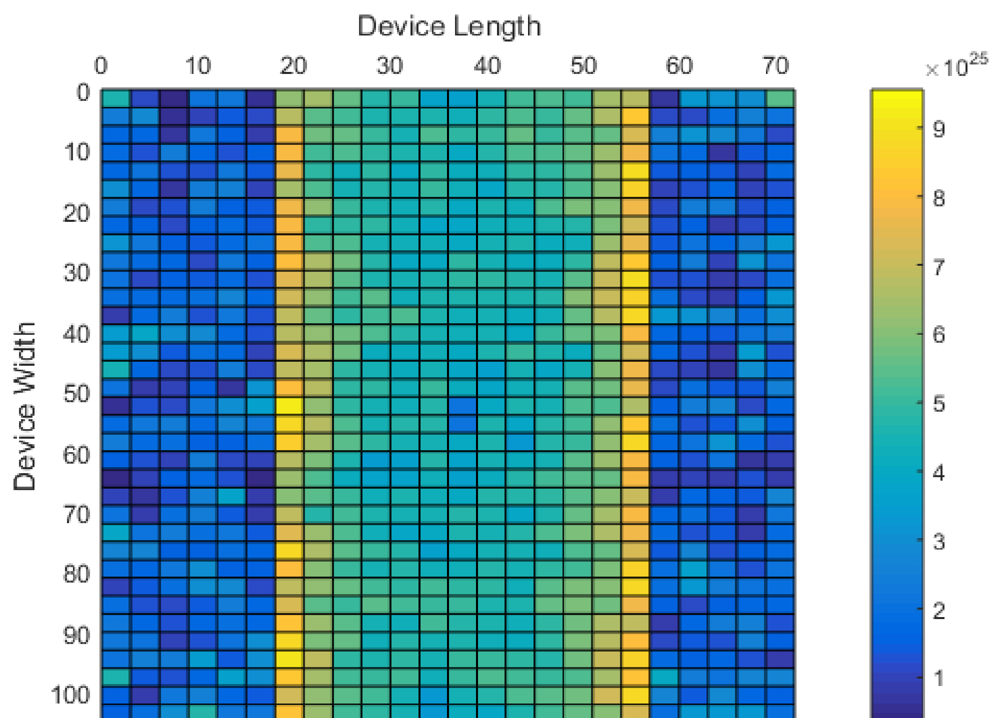

Source: Elaborated by the author

Figure 23 shows carrier accumulation on the channel interface with the oxide, creating a conductive channel between source and drain.

Figure 25 shows electron density distribution along the directions of device depth and length after the drain voltage of 1.1 V is applied and the device is simulated for 3 ps. Figure 26, alternatively, shows carrier density for these conditions but along the directions of device width and length. In both figures, pinch-off effect is clearly seen near the drain end (around 54 nm in device length direction), where the electron density becomes very low.

Figure 25 - Electron density [m^{-3}] along device length and depth after 3 ps simulation.

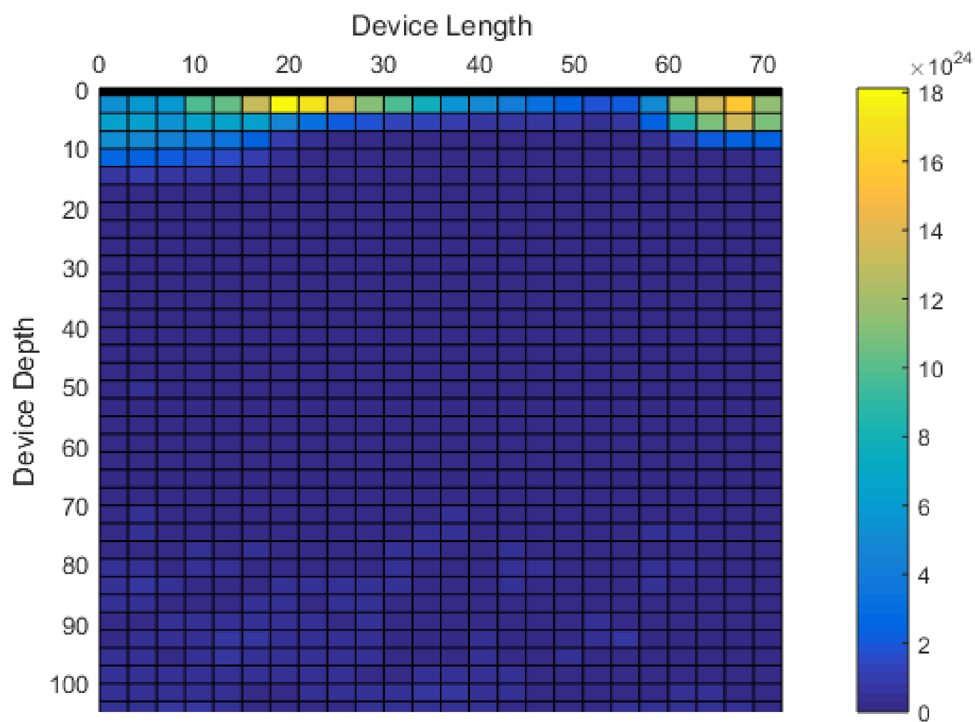

Source: Elaborated by the author

Figure 26 - Electron density [m^{-3}] along device length and width after 3 ps simulation.

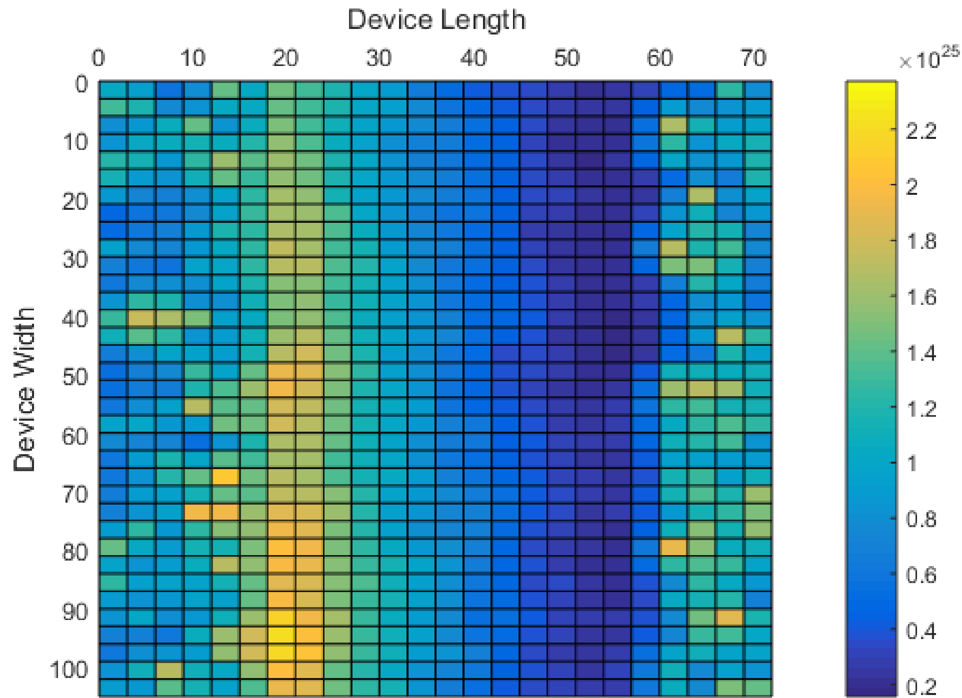

Source: Elaborated by the author

7 N-FINFET DEVICE SIMULATOR RESULTS

Some relevant simulation results that validate the 3D FinFET simulator are presented next. A single-fin n-FinFET (Figure 27) with channel length L_{ch} = 18 nm, W_{fin} = 8 nm and H_{fin} = 42 nm was simulated. The total device length (L) is 78 nm, which includes the source (0 – 30 nm), the channel (30 nm – 48 nm) and the drain (48 nm – 78 nm). The total device depth (D) is 57.2 nm. The total device width (W) is 10.4 nm, which includes the thickness of the gate dielectrics located in the interface with the side channels. The simulation time was 15 ps. The simulations were performed with $V_G = V_D = 0.9$ V and $V_S = V_B = 0$ V, except when said differently. TiN was used as metal gate material, which has average grain size of 20 nm and work function of WF = 4.6 eV with 60% probability and WF = 4.4 eV with 40% probability (DADGOUR; ENDO; DE; BANERJEE, 2010). Surface roughness scattering is treated as being 15% diffusive and 85% specular (BUFLER; SMITH, 2013).

Figure 27 – Basic structure of the FinFET used in this work. The silicon area is presented in gray, the gate dielectric is shown in yellow, the metal gate is depicted in red, and the silicon oxide is shown in blue.

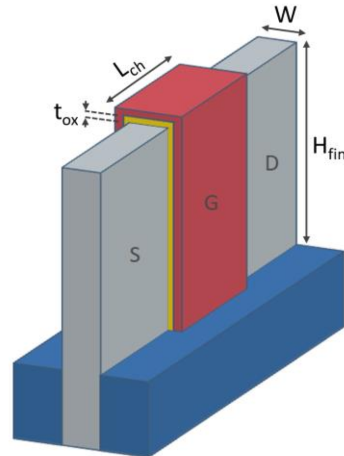

Source: Elaborated by the author

The device length is in the direction from source to drain, i.e., along the channel length (defined as L-direction). The device depth is defined as the oxide-substrate direction (D-direction). The width of the device is aligned with the channel width (W-direction).

The random placement of the dopants in a device is shown in Figure 28 for acceptors and donors doping concentration of $N_A = 5.10^{18}$ cm^{-3} and $N_D = 10^{19}$ cm^{-3} respectively.

Figure 28 - Dopant atoms randomly distributed in the device. The acceptor atoms are represented with black circles, and the donors with blue circles.

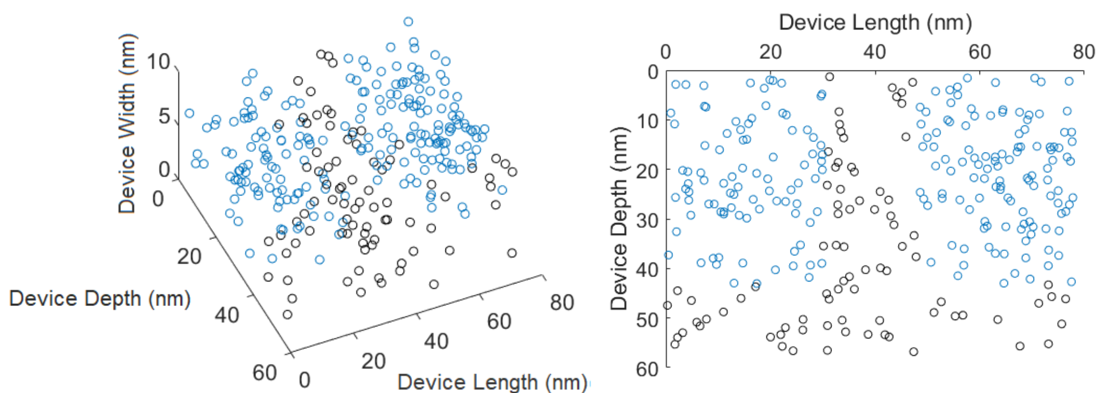

Source: Elaborated by the author

Metal grain granularity is depicted in Figure 29, which presents the electric potential on a side gate. Figure 29 clearly shows the presence of metal grains and illustrates the existence of regions with different work functions that lead to fluctuations on the gate potential.

Figure 29 - Electric potential distribution over one of the side gates of a FinFET, showing the presence of metal grains with different characteristics. The yellow cells (1.103 V) have a potential 0.2 V higher than the blue ones (0.903 V), due to the difference in the work function in those regions.

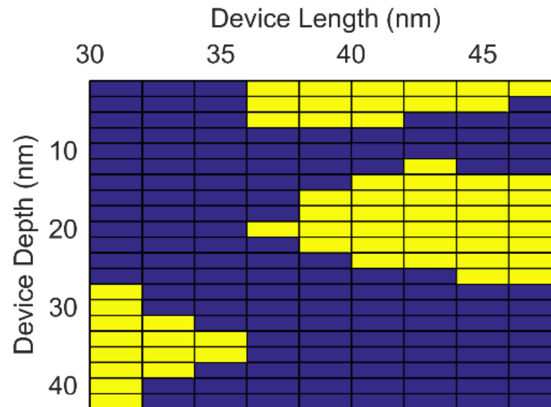

Source: Elaborated by the author

Figure 30 (a) and (b) shows respectively the average carrier velocity and energy. It is possible to see that the energy peak is located near the drain end, as expected, and experimentally verified.

Figure 30 - Velocity (a) and energy (b) of the ensemble of carriers in different devices. The black line represents the average values for a set of devices.

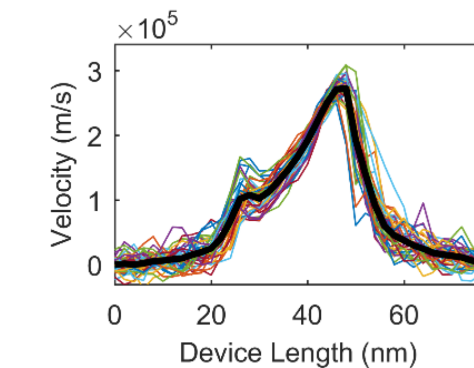

(a)

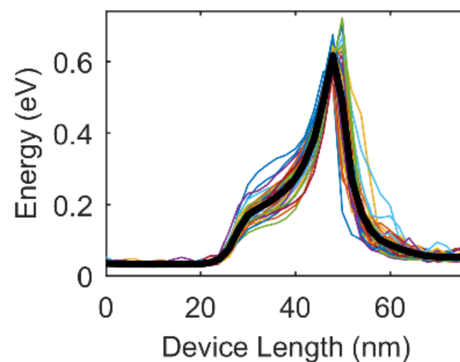

(b)

Source: Elaborated by the author

The electric potential was plotted for different cut-planes in the length and the depth of the device, with the width position fixed at the center of the fin, i.e., equal to W/2. In Figure 31, the simulation results for the electrostatic potential with $V_D = V_S = V_B = 0$ V are shown. In Figure 32, the same plot is shown, but with the drain bias of $V_D = 0.9$ V and $V_S = V_B = 0$ V. The total simulation time is 15 ps. It is possible to see that the donor dopants are randomly distributed in the source and in the drain region and they significantly perturbate the potential. In the channel region (L = 30 nm – 48 nm, H = 1.2 nm – 43.2 nm and W = 1.2 nm – 9.2 nm), there are also significant variations of the electrostatic potential caused by the substrate dopants.

Figure 31 . Electrostatic potential along the device length and depth with $V_D = V_S = V_B = 0$ V and (a) $V_G = 0.1$ V, and (b) $V_G = 0.9$ V.

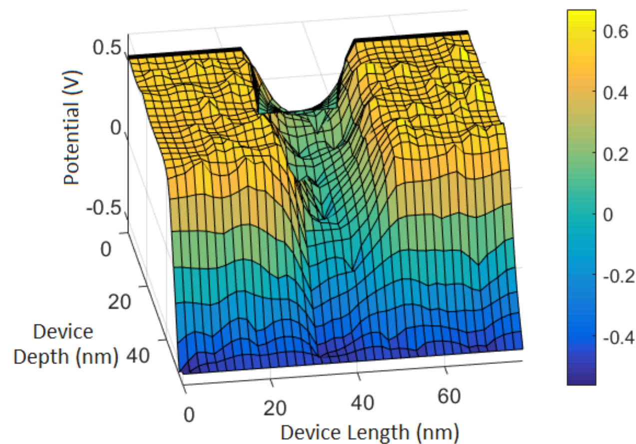

(a)

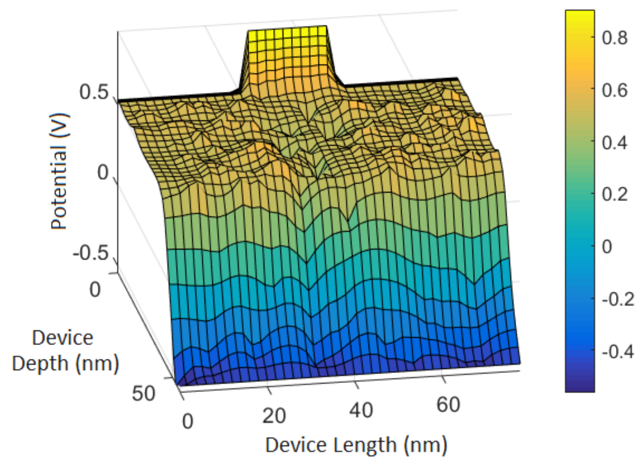

(b)

Source: Elaborated by the author

With $V_D = V_S = V_B = 0$ V, the source and drain contacts are at the same electrostatic potential, and the gate bias impact is clearly seen from Figures 31 (a) and (b). The case when voltage of 0.9 V is applied on the drain is shown in Figure 32.

Figure 32 Electrostatic potential in the device as a function of its length and depth with $V_D = 0.9$ V, $V_S = V_B = 0$ V, and (a) $V_G = 0.1$ V, and (b) $V_G = 0.9$ V.

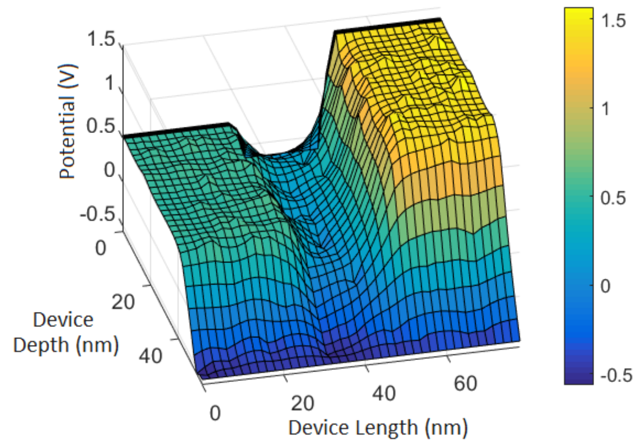

(a)

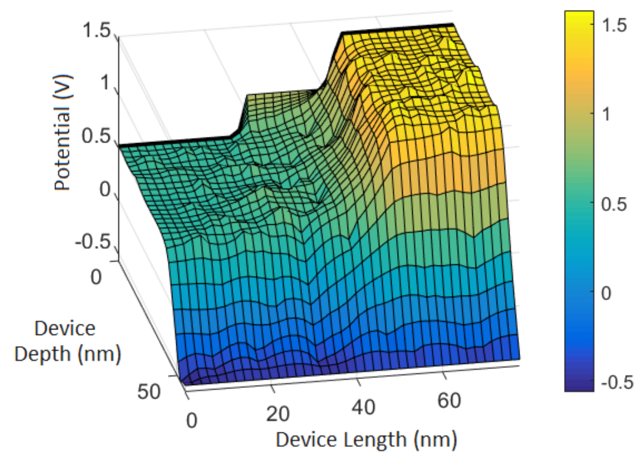

(b)

Source: Elaborated by the author

The electrostatic potential was also plotted as a function of the position in the direction of device width and length, with the position in the depth direction fixed as the top channel silicon/gate dielectric interface. Figure 33 displays the results for $V_G = 0.9$ V, $V_D = V_S = V_B = 0$ V, and in Figure 34 the results obtained for $V_G = V_D = 0.9$ V and $V_S = V_B = 0$ V after the 15 ps simulation are presented.

Figure 33 - Electrostatic potential along device length and width for equilibrium condition with $V_G = 0.9$ V, $V_D = V_S = V_B = 0$ V.

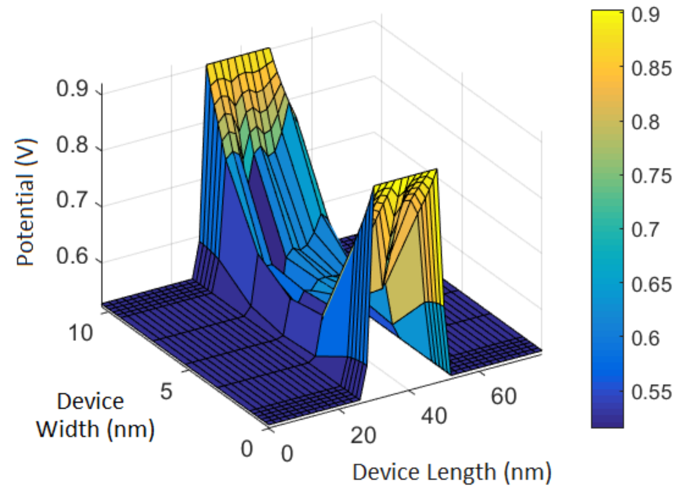

Source: Elaborated by the author

Figure 34 - Electrostatic potential in the device as a function of its width and depth with $V_G = V_D = 0.9$ V and $V_S = V_B = 0$ V.

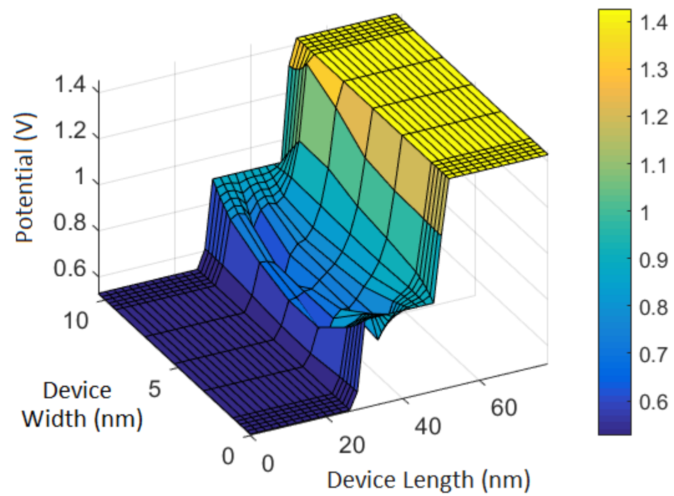

Source: Elaborated by the author

Figure 35 shows electron density distribution of a device along the directions of its depth and length after the drain voltage of 0.9 V is applied and the device is simulated for 15 ps.

Figure 35 - Electron density [m^{-3}] along device length and depth after 15ps simulation for a slice in the middle of the channel width (W/2).

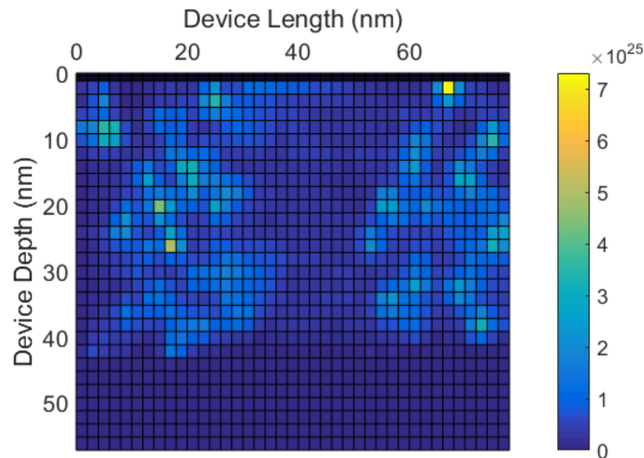

Source: Elaborated by the author

Note that, since the plot in Figure 35 represents a 2-D slice taken from the middle of the fin width, the top channel carriers are captured in the figure as a high concentration near the oxide-silicon interface with depth of 1.2 nm.

Figure 36 shows carrier density also in the directions of device length and depth and for the same simulation conditions, but with the position on the width direction defined as the interface between one of the side channels and the gate dielectric. It is possible, therefore, to capture the behavior of the side channel as well. In both Figures 35 and 36, pinch-off effect is clearly seen near the drain end (around 48 nm in the device length direction), where the electron density becomes very low.

Figure 36 - Electron density [m^{-3}] along device length and depth after 15ps simulation for a slice that captures one of the side channels.

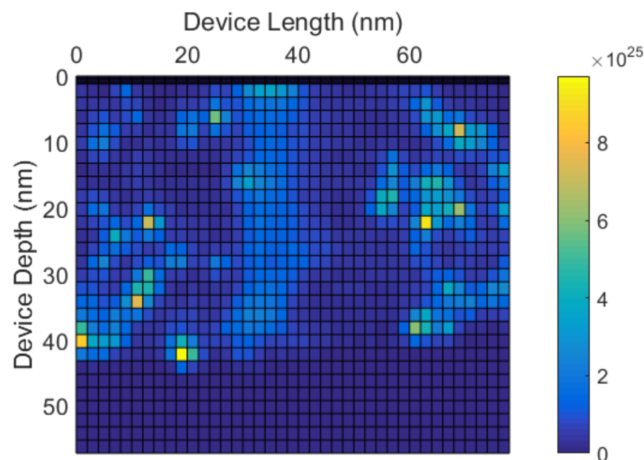

Source: Elaborated by the author

The behavior of the drain current of the n-FinFET is shown in Figure 37 as the I_D -V_G curve, and in Figure 38 as I_D -V_D curve. These results correspond to well established values for MOS transistors.

Figure 37 - I_D -V_G curve for different devices, depicting the variability between devices with the same parameters.

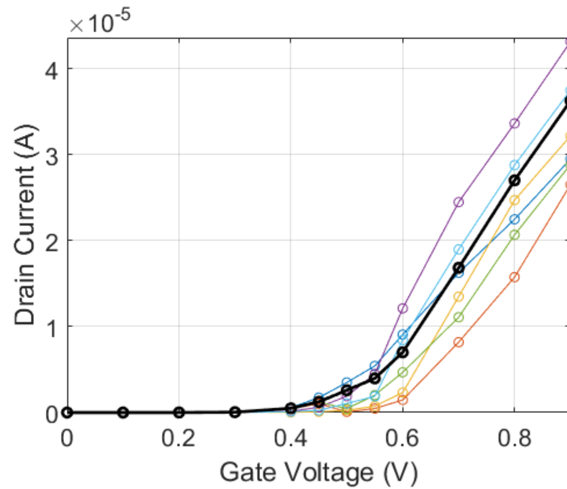

Source: Elaborated by the author

Figure 38 - I_D -V_D curve for different devices with the same parameters as in Figure 37.

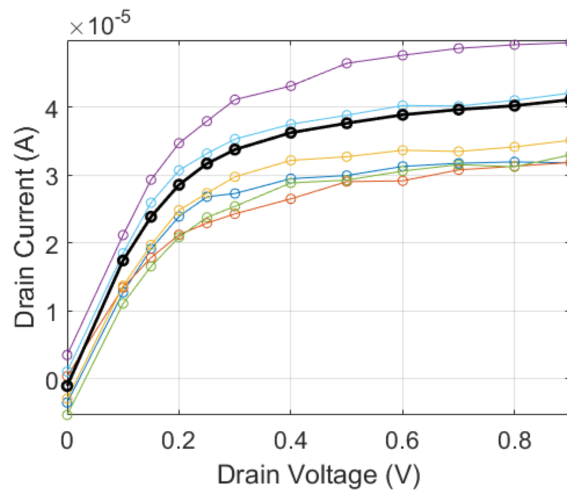

Source: Elaborated by the author

8 CASE STUDIES

Since it allows state-of-the-art FinFET simulation, the 3-D Monte Carlo Device simulator has already been used to study different aspects regarding charge transport and reliability concerns in FinFETs. The simulator unique real-space carrier-carrier and carrier-ion treatment allowed its usage to study ballistic transport in a novel carrier-centric perspective, and the results were presented in the paper “Evaluating the Ballistic Transport in nFinFETs: a Carrier Centric Perspective” (FURTADO; CAMARGO; VASILESKA; WIRTH, 2021a). The simulator was also used to study hot-carrier degradation in FinFETs, extracting breakthrough information related to its link to percolation paths and to the trap impact distribution along the channel. This is only possible because, different to the simulators typically employed in HCD model studies, the simulator which was developed considers the individual random position of the charge dopants and the carriers, without relying on densities anyhow. This study resulted in a paper entitled “Correlation of HCD and percolation paths in FinFETs: study of RDF and MGG impacts through 3-D Particle-Based Simulation” (FURTADO; CAMARGO; VASILESKA; WIRTH, 2021b). The simulator is currently being used in undergoing studies regarding trap coupling. The novel 3-D particle-based simulator itself was described in a paper called “3-D TCAD Monte Carlo Device Simulator: State-of-the-art FinFET Simulation” (FURTADO; CAMARGO; VASILESKA; WIRTH, 2021c), accepted for publication on Journal of Integrated Circuits and Systems. This manuscript accounts for the main theoretical details and the most relevant device performance/characteristics which were described in this thesis (© 2021 Journal of Integrated Circuits and Systems).

8.1 Ballistic Transport in FinFETs

The contents of the paper “Evaluating the Ballistic Transport in nFinFETs: a Carrier Centric Perspective” (FURTADO; CAMARGO; VASILESKA; WIRTH, 2021a), submitted to IEEE Transactions on Nanotechnology and currently under review, will be presented next.

As transistors’ dimensions become comparable to the mean-free path of the carriers in the material, modern FinFETs are expected to have a large number of carriers that cross the channel ballistically. Therefore, an increasing number of carriers do not undergo any scattering event in the channel (besides for the carrier-carrier interactions), so that ballistic transport may govern carrier dynamics. It is, therefore, mandatory to understand how close to

the ballistic limit are state-of-the-art FinFETs and to understand the ballistic transport properties of the same.

It is well known that TCAD simulators are a powerful tool used to evaluate transport in modern FinFETs. Furthermore, Monte Carlo (MC) device simulators are believed to be a very effective tool to evaluate ballistic transport in semiconductor devices within the semiclassical limits (ELTHAKEB; ELHAMID; ISMAIL, 2015). At least down to gate length of L_G = 10 nm, Monte Carlo device simulators are known to be an adequate tool to study charge transport in nanoscale devices (PALESTRI et al, 2005). Several studies exist regarding modeling and simulation of ballistic transport in semiconductor devices (AKIS et al., 2009; BAYKAN; THOMPSON; NISHIDA, 2012; CURATOLA; FIORI; IANNACCONE, 2004; KHAN; MAMALUY; VASILESKA, 2007; KIM; LUNDSTROM, 2008, RAHMAN *et al.*, 2003) using different methods. Monte Carlo based device simulators are consistently used to study ballistic transport in deeply scaled devices. Besides the ballisticity ratio (GNANI *et al.*, 2009), previous studies cover topics such as drift velocity along the channel (ELTHAKEB; ELHAMID; ISMAIL, 2015; BUFLER *et al.*, 2017), inversion charge and potential energy profiles along the device (PALESTRI *et al*, 2004), and the role of scattering in different parts of the device (PALESTRI *et al*, 2005).

Considering the above, the 3D-TCAD Monte Carlo device simulator presented is this thesis is used in this study to study ballistic transport in deeply scaled n-FinFETs. This work differs from previous studies as it reaches beyond the traditional metrics as the ballisticity ratio, looking at specific carrier's statistics to achieve a better understanding of the transport in FinFETs. This is one of the main advantages of the Monte Carlo device simulation technique over other simulation methods, since it allows access to individual carrier's characteristics such as their energy and position at any time instant. However, a carrier centric perspective on ballistic transport using MC device simulation has yet not been explored; in this regard, this study aims to provide a new perspective to the ballistic transport effects. Aspects, such as the importance of phonon and surface roughness scattering (individual and combined) and the percentage of carriers that cross the channel ballistically, are thus, exploited here. Valuable information about the carriers' transit time, their relation to ballistic transport, the energy distribution functions of ballistic and non-ballistic carriers, and the role of e-e interaction on the shape of this distribution is also presented. For completeness, the studies were performed on devices with different channel lengths to show the impact of scaling concerning ballistic transport. A significant advantage of this work compared to

previous works is that the ballisticity is investigated in the context of discrete impurities treated in real-space, as well as metal grain granularity, what can significantly impact the results due to changes on the percolation paths.

This study is organized as follows. In section 8.1.1, the information on the device structures used in this study is given, and details about different aspects of ballistic transport, such as ballisticity ratio, percentage of ballistic carriers, energy distribution of the ballistic carriers and its relationship with electron-electron and electron-phonon interactions are provided. The results of the simulations and in-depth discussions regarding the findings are presented in Section 8.1.2. Finally, in section 8.1.3 the key points regarding ballistic transport in nano FinFETs are summarized.

8.1.1. Methodology

The devices used in this study are nFinFETs with channel length L_{ch} varying from 14 nm to 30 nm, channel width W = 8 nm, fin height H_{fin} = 42 nm, source and drain random doping $N_D = 10^{19}$ cm-3, gate dielectric with equivalent oxide thickness of t_{ox} = 1.2 nm and TiN as metal gate with an average grain size of 22 nm and a work function of 4.6 eV with 60% probability or 4.4 eV with 40% probability (DADGOUR *et al.*, 2010), depending on MGG. The applied voltages were $V_G = V_D = 1$ V and $V_S = V_B = 0$ V. In Sections 8.1.2 (A) and (B), the simulation time was 30 ps and 60 Monte Carlo seeds were used. For the other sections, where a larger dataset was required, the simulation time was 100 ps and 70 Monte Carlo seeds were used in the analysis (more than one million carriers were used in the statistical analysis).

Only the electrons that entered the channel from the source and made it to the drain end of the channel were reported in all the studies presented here. Even though they naturally happen in the entire device during the simulation, the scattering events were counted only inside the channel, and the scattering counts were set or reset to 0 when the carrier reached the source region. The energy was measured at the moment the carriers reached the drain electrode, after crossing the channel.

The methodology used in the analysis of the vast amount of data generated is as follows. First, the ballisticity ratio (BR) is discussed. Even though this metric is commonly seen in the literature, the results deviate considerably in different papers, because the BR is strongly dependent upon the device geometry and characteristics as well as with the bias

(AKIS *et al.*, 2009). Next, the impact of channel length scaling on the number of scattering events that each carrier undergoes is studied. In this context, individual contributions of phonon and surface roughness scattering are evaluated. The time the carriers took to cross the channel was measured, here also referred to as the transit time (t_{tr}), both for electrons that did and did not suffer scattering events in the channel, to obtain the transit time distribution. Finally, the electrons' energy distribution under different conditions are analyzed. First, it is verified how the electrons' energy distributes grouped by the time the electrons took to cross the channel (for both 14 nm and 30 nm devices). Then, these distributions are compared to the ones obtained with the short-range (SR) e-e interactions turned off, aiming to study their impact. It is important to point out that the long-range e-e interactions are still present due to each electron's impact on the Poisson equation solution via the particle-mesh coupling.

8.1.2. Results and Discussions

A. Ballisticity Ratio

The ballisticity ratio ($BR = \frac{I_{on}}{I_{ball}}$) is the ratio between the on-current (I_{on}), which naturally includes scattering events, and the current with the scattering mechanisms turned off inside the channel (I_{ball}).

Figure 39 - (a) Drain current with (I_{on}) and without (I_{ball}) scattering, (b) percentage of carriers which suffer zero scattering events (ballistic carriers) for different channel lengths and (c) the ballisticity ratio compared to other similar works from the literature, being [1] (ELTHAKEB; ELHAMID; ISMAIL, 2015), [2] (PALESTRI *et al.*, 2005), [10] (BUFLER *et al.* 2017) and [11] (PALESTRI *et al.*, 2004).

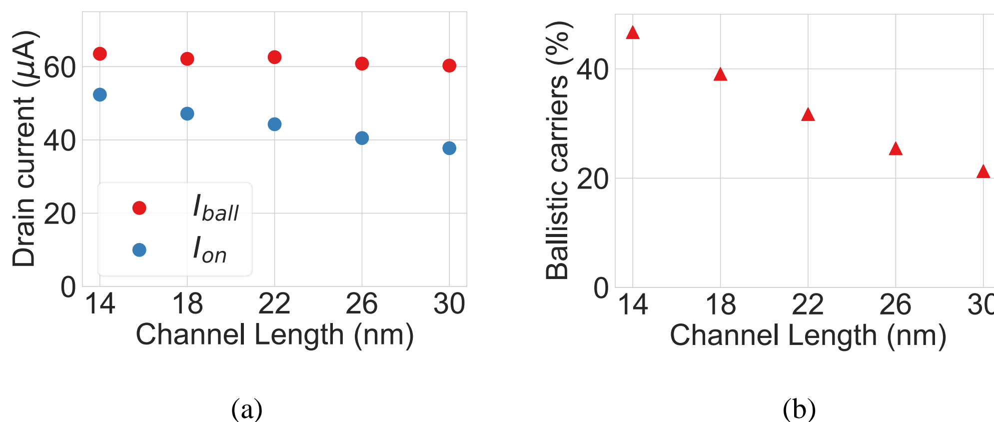

(a) (b)

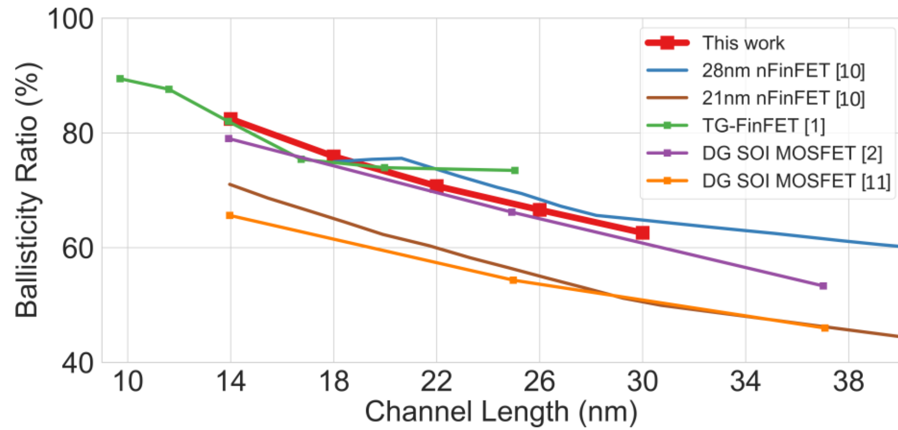

(c)

Source: Elaborated by the author

Figure 39 (a) shows that the current without scattering remains approximately constant with the change of the channel length, and the current with the scattering mechanisms turned on decreases as channel length increases, as expected. This means that the BR, which is the ratio of these two quantities, must decrease for larger channel lengths, as shown in Figure 39(c). The results obtained are consistent with the literature (ELTHAKEB; ELHAMID; ISAMAIL, 2015; PALESTRI *et al.*, 2005; BUFLER *et al.*, 2017; PALESTRI *et al.*, 2004). Note that, in order to obtain the results showed in Figure 39(c), some works only change the gate length (BUFLER *et al.*, 2017), keeping all other device and operation parameters the same, as was done in our simulations, while others also scaled other geometry and bias parameters following technology-node specifications (ELTHAKEB; ELHAMID; ISAMAIL, 2015). The percentage of ballistic carriers, i.e., the portion of carriers that drifts through the channel without undergoing any scattering event is shown in Figure 39(b). Note that the ballisticity ratio and the percentage of ballistic carriers have different meanings and significantly different values. While the BR ranges from 82.4% for the 14 nm device, it drops down to 62.6% for the 30 nm nFinFET, and the percentage of ballistic carriers changes from 46.7% to 21.3%, respectively.

B. Scattering Statistics

Each carrier was tracked during the MC simulation, and every scattering event was annotated. The histograms in Figure 40 depict the distribution of the number of scattering events experienced by a single carrier as it crossed the channel. For better visualization, the histograms are normalized. Figures 40 (a), (b) and (c) depict the histograms for FinFETs with

gate lengths of 14 nm, 22 nm, and 30 nm, respectively. When comparing these results, it is possible to notice a similar distribution, but with an increase in its mean and standard deviation, as a function of the gate length. One should also pay attention to the count zero, which groups the carriers that crossed the channel without any scattering event. An increase in the carriers' probability as the channel shrinks (from 21.3% for the 30 nm channel length device to 46.7% for the 14 nm one) is observed.

Figure 40 - Histogram of the number of scattering events a single carrier experienced while crossing the channel in devices with channel lengths of (a) 14 nm, (b) 22 nm and (c) 30 nm. The histograms are normalized by the number of carriers evaluated to show the probability as a function of the scattering events count.

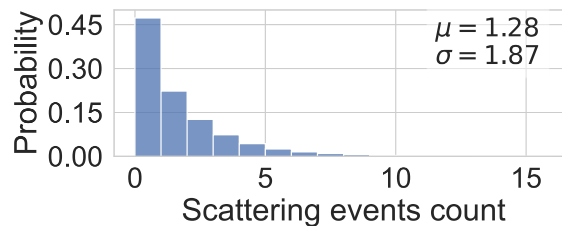

(a)

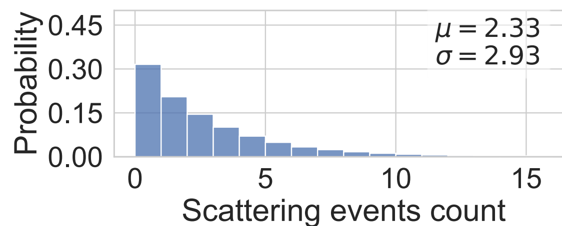

(b)

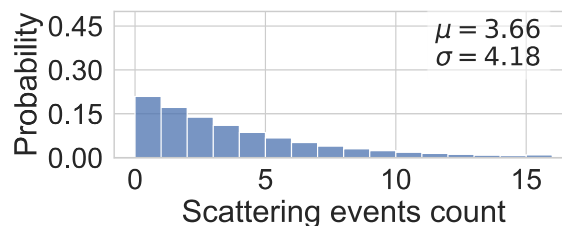

(c)

Source: Elaborated by the author

In this study, the importance of only phonon and surface roughness scattering on the transport characteristics of nano FinFET is also verified. The e-i interactions are not presented here as they are less relevant for intrinsic channels and excluding the impact of unintentional dopants. The main graphs in Figure 41(a-c) show the bivariate histograms of the count of

surface and phonon scattering events, represented as a heatmap. The sub-plots above show the histogram of the scattering event counts per carrier for each mechanism. As in Figure 40, the sub-plots in Figure 41 are normalized so that the bin's heigh indicates the probability for a particular count to happen.

Figure 41 - The main plot shows the bivariate histograms of the scattering events a single carrier experienced while crossing the channel in devices with channel lengths of (a) 14 nm, (b) 22 nm and (c) 30 nm. The sub-plots show the normalized histogram for particular scattering mechanism (either phonon scattering or surface roughness scattering).

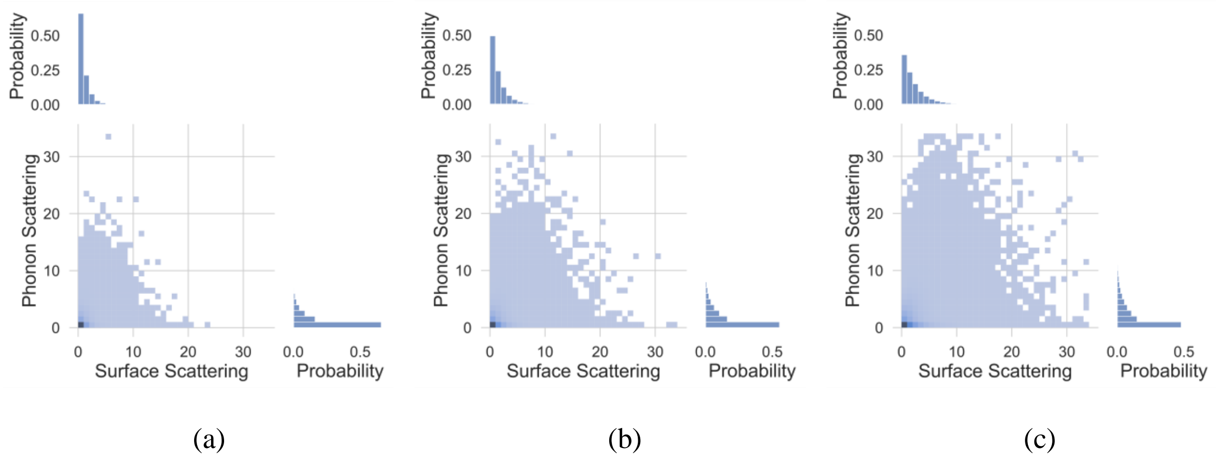

Source: Elaborated by the author

In Figure 41, one can see that, despite a reduction in the occurrence of both scattering mechanisms as the device length scales, the surface roughness scattering count reduces at a higher rate when compared to the phonon scattering. This trend is observed both in the main graphic and in the sub-plots. The surface roughness scattering reduction is directly related to the reduction of the channel length, as with a shorter channel, there are naturally fewer carrier-surface interactions. The scaling also affects phonon scattering, but it is not as pronounced as the carriers' average energy does not scale proportionally (the bias is the same for all devices considered in the study).

It is important to notice that the impact of the scattering mechanisms is device and bias dependent. The elevated gate voltage used in these simulations increases the current' density close to the Si/SiO_2 interface (BROWN *et al*., 2013), leading to a higher impact of the surface roughness scattering. The fin dimensions will also play an important role in the surface roughness scattering count. The impact of phonon scattering near the source region will depend on the source resistance and the carriers' energy there. A higher drain bias leads to high energy carriers, with a scattering rate due to ionized impurities significantly diminished.

Nevertheless, the methodology presented here allows the device engineer to clearly see the impact of each mechanism on carriers' transport.

C. Transit time

Figure 42 shows the probability distribution of the transit time (t_{tr}) in 14 nm and 30 nm devices, considering all carriers that drifted through the channel (Figure 42(a)) and filtering only the electrons that traveled ballistically (Figure 42(b)). Note that Figure 42 depicts the Probability Density Function (PDF) of log(T_{tr}). The approximated distributions presented here were obtained as the Kernel Density Estimation (KDE) of over one million carriers that crossed the device. From the results presented in Figure 42(a), it is evident that the average transit time for the carriers in the 30 nm device is larger and has a larger tail of the distribution. In this device, it takes a longer time for the carriers to cross the channel since the channel is longer. The results presented in this figure also illustrate the fact that the number of ballistic or quasi-ballistic carriers is concentrated in the short transit times for both devices, while the non-ballistic ones dominate for larger transit times. Another interesting fact this figure illustrates is that there are also non-ballistic carriers as fast as the ballistic ones. These non-ballistic fast carriers are the ones that, despite suffering scattering events, had their new momentum (after scattering) in the same direction as the electric field, thus not slowing down.

Figure 42 - Distribution of the transit time in 14 and 30 nm gate length devices. Case (a) considers all carriers that crossed the channel, and case (b) considers only the carriers that had no scattering in the channel.

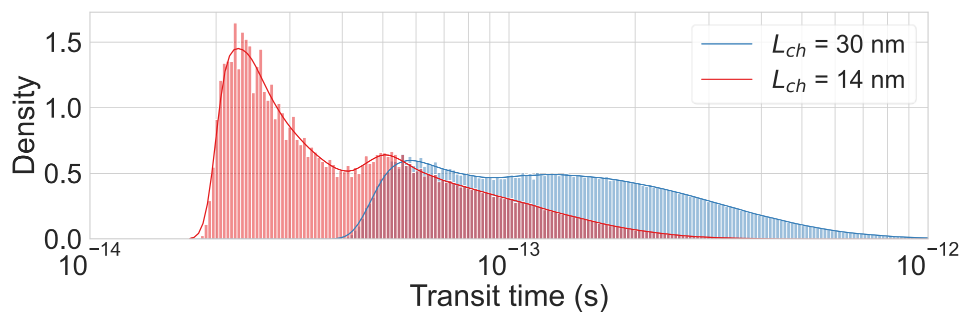

(a)

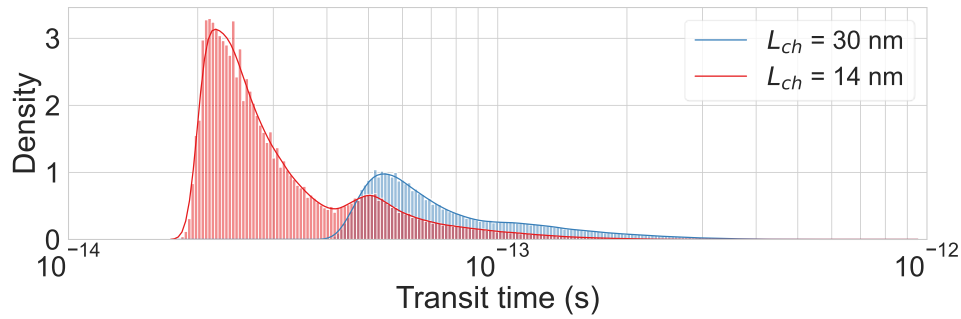

(b)

Source: Elaborated by the author

D. Energy Statistics

Analyzing the PDF of the energy of the carriers at the entrance and at the exit of the channel, presented in Figure 43, it is possible to see that, as the time the carriers spent in the channel increases, the average energy of the electron gets smaller, but the standard deviation gets larger, thus resulting in a wider distribution function. The energy at the moment the electrons enter the channel (~0.2 eV) is due to the relatively high source resistance, so the carriers are already being subject to a significant electric field before entering the channel. Comparing Figure 43(a) and Figure 43(b), it is possible to see that both, small and large devices, show roughly the same behavior. The number of carriers which meet the $t_{tr} < 50$ fs criteria gets significantly smaller in the larger device. However, since the carriers naturally take longer to cross the channel, and the carriers' average energy with $t_{tr} < 50$ fs gets larger, only the fastest (least energy loss) electrons enter the count for the 30 nm device. The distribution for $t_{tr} > 100$ fs is even more shifted to lower energies for the 30 nm device, which is a consequence of having a large amount of much slower ($t_{tr} > 200$ fs) carriers. The widening and the shift of these distributions with the increase of t_{tr} is attributed to the phonon and surface roughness scattering mechanisms.

Figure 43 - Distribution of the electrons' energy at three different moments (entrance in the channel, exit of the channel with t_{tr} < 50 fs and exit of the channel with t_{tr} > 100 fs), for (a) 14 nm device and (b) 30 nm device.

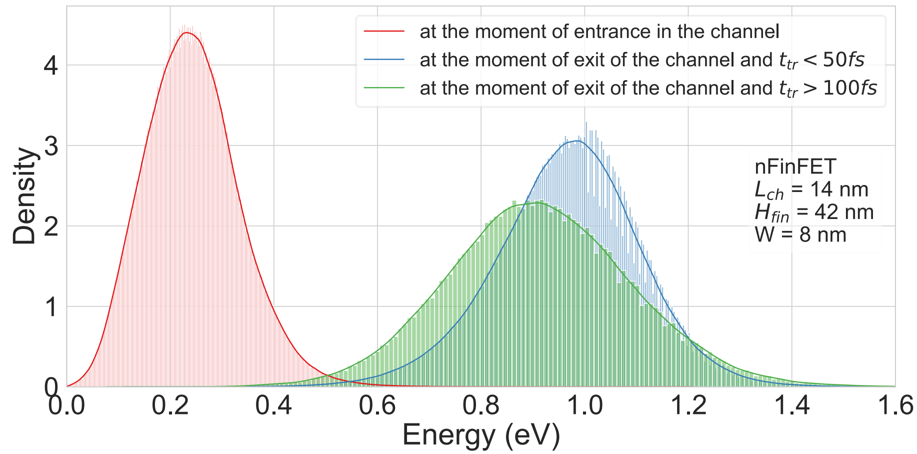

(a)

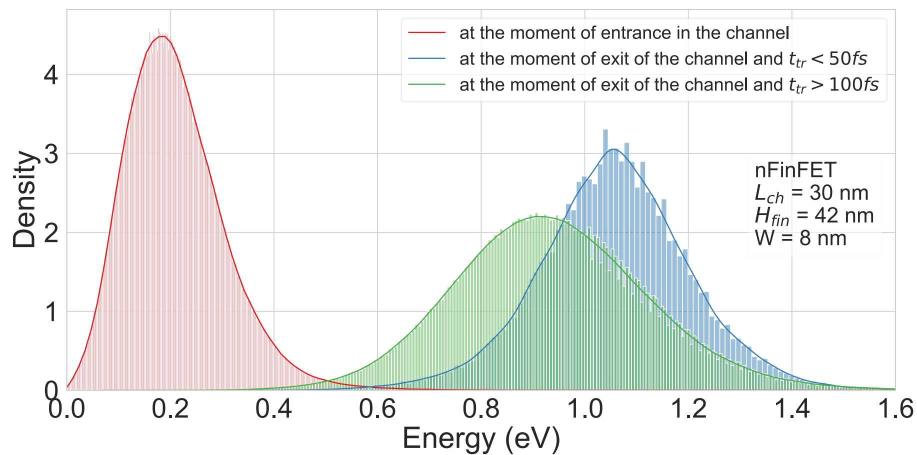

(b)

Source: Elaborated by the author

Figure 44 - Distribution of the electrons' energy for transit times in three different time windows for (a) 14 nm and (b) 30 nm devices.

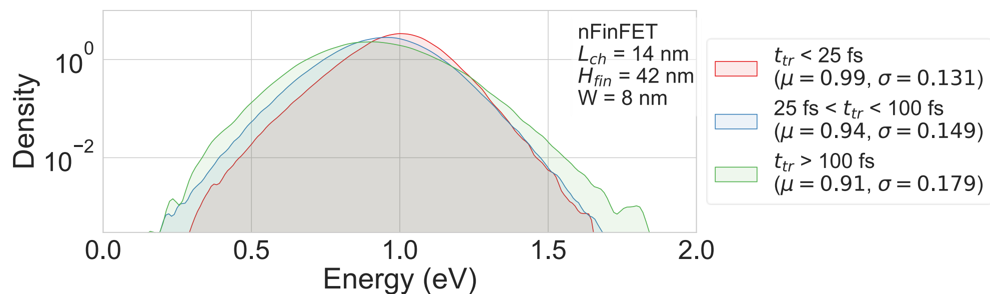

(a)

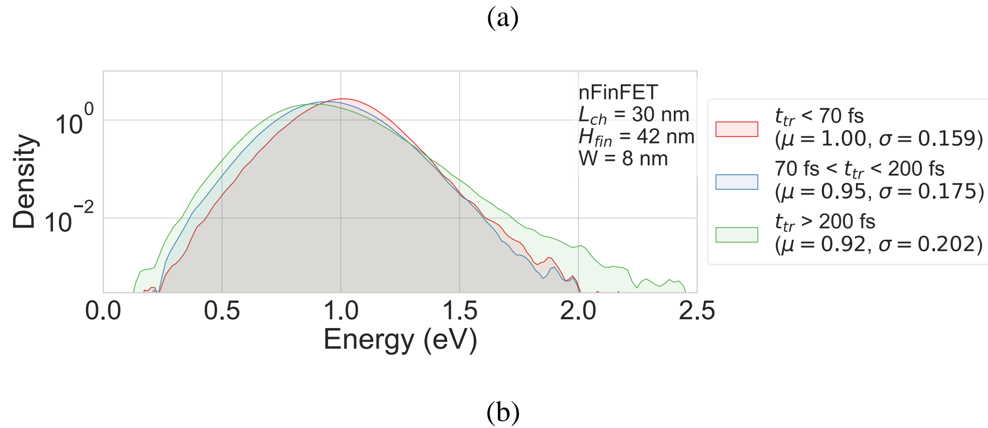

(b)

Source: Elaborated by the author

Figure 44 presents the distribution (KDE) of the carriers' energy at the moment of exit from the channel. The distributions are made for electrons with different transit times in three windows, the ones considered fast, the ones considered slow and the ones in between. Due to the different channel lengths of the devices, the limits of these windows differ from (a), relative to the 14 nm channel length device, to (b), relative to the 30 nm one. A careful look at these KDEs shows that the longer an electron stays in the channel, the smaller the average energy and the wider is the distribution. The average energy of the fast electrons (t_{tr} < 70 fs) is 1 eV, as would be expected from having V_D = 1 V. The widening of the distributions occurs due to the thermalization of the carriers' energy caused by the scattering mechanisms and the e-e interactions. The thermalization due to phonon scattering is in the order of magnitude of the pico-seconds, while due to carrier-carrier interaction may vary from femto-seconds to pico-seconds depending on the carrier concentration (OTHONOS, 1998). Thus, in these small devices, where the transit time is a fraction of pico-seconds, one can notice that in the 14 nm device the widening is much smaller than in the large one, where the shape of the distribution begins to change noticeably. Alterations like this in the carriers' energy distribution are of particular interest for Hot Carrier Injection (HCI) studies as modeled in (BINA *et al.*, 2012), particularly due to carrier-carrier interactions in which a few electrons might gain large energies. It can also be observed in this figure that in short devices, where the transit time of electrons is smaller than 0.1 ps, the hot electrons created by e-e interactions are rare, indicating a possible impact on the HCI effect.

E. Short-range electron-electron interaction impact

Figure 45 - Distributions of carriers' energy with and without short-range e-e interactions for 14 nm channel length device with transit time smaller than 25 fs (a), between 25 fs and 100 fs (c)

and larger than 100 fs (e), and for 30 nm channel length devices with transit time smaller than 70 fs (b), between 70 fs and 200 fs (d) and larger than 200 fs (f).

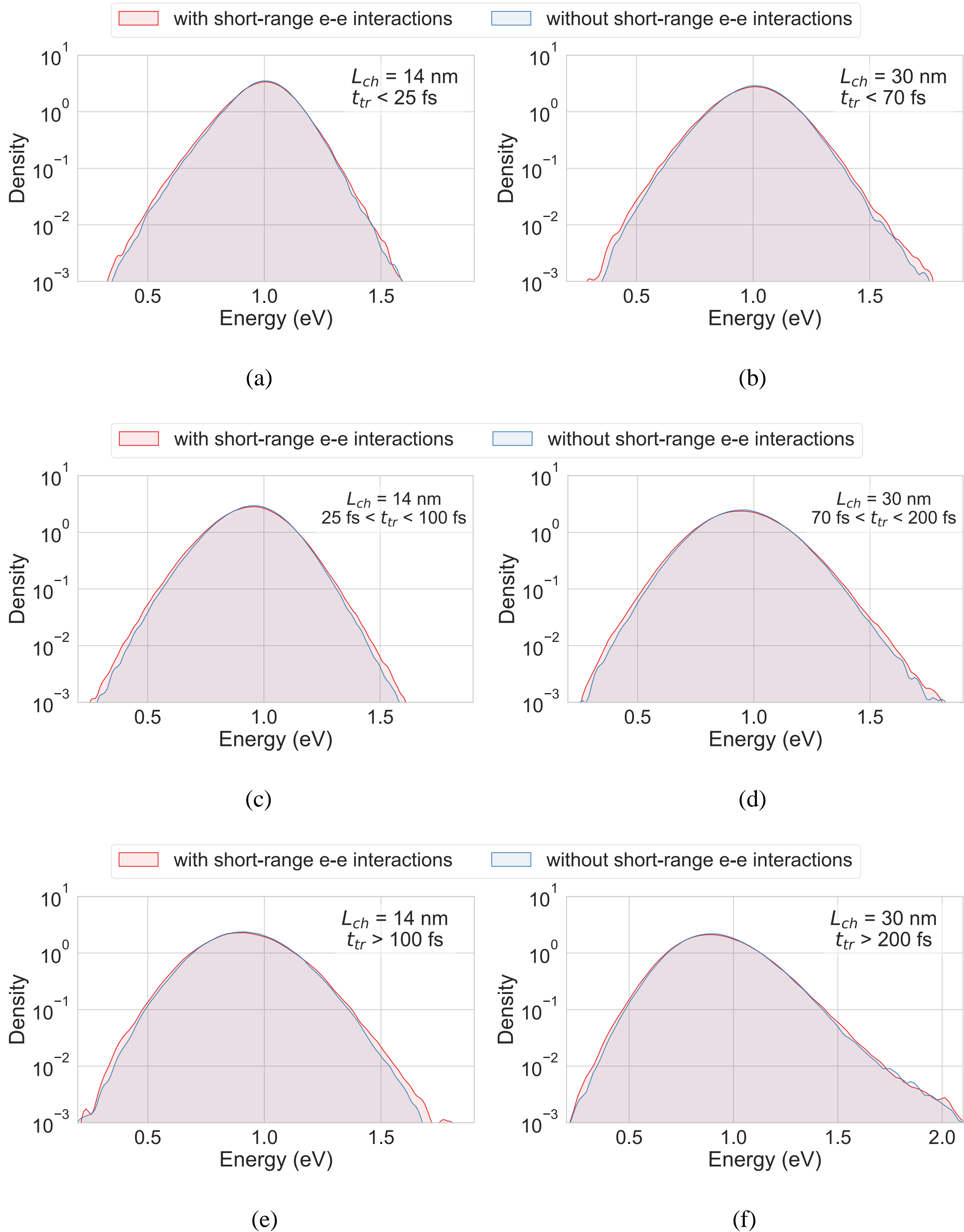

Source: Elaborated by the author

Table 1 – Mean and Standard Deviation of the Distributions in Figure 45(a),(c),(e)

14 nm		
	μ (eV)	σ (eV)
t_{tr} < 25 fs	0.992	0.131

With SR e-e interaction	25 fs < t_{tr} < 100 fs	0.943	0.149
	t_{tr} > 100 fs	0.914	0.179
Without SR e-e interaction	t_{tr} < 25 fs	0.995	0.126
	25 fs < t_{tr} < 100 fs	0.947	0.143
	t_{tr} > 100 fs	0.916	0.172

Table 2 - Mean and Standard Deviation of the Distributions in Figure 45(b),(d),(f)

30 nm			
		μ (eV)	σ (eV)
With SR e-e interaction	t_{tr} < 70 fs	1.003	0.155
	70 fs < t_{tr} < 200 fs	0.952	0.175
	t_{tr} > 200 fs	0.923	0.202
Without SR e-e interaction	t_{tr} < 70 fs	1.006	0.148
	70 fs < t_{tr} < 200 fs	0.955	0.168
	t_{tr} > 200 fs	0.925	0.196

The 3D Monte Carlo device simulator used in this study evaluates the e-e interactions through two different mechanisms, the long-range interactions, that are generated by each electron's contribution to the electrons' density, which is used in the Poisson solver, and the SR interactions, that are evaluated in the real-space. Figure 45 shows the impact of the short-range e-e interactions on the carriers' energy for the 14 nm channel length FinFET. Case (a) depicts the energy distribution of the carriers with a transit time lower than 25 fs, considering and not taking into account the SR e-e interactions. One can see that the SR e-e interactions had some effect on the shape of the distribution function with an increase in the standard deviation. The mean of the distribution had a negligible decrease of 0.3%, which is expected as the energy gained by one electron is lost by another. Figure 45 (c) and (e) present the same analysis, but filtering carriers with transit time between 25 fs and 100 fs, and larger than 100 fs, respectively. In Figure 45(c) and (e), a more significant widening of the distribution can be observed in the simulation that considers the SR e-e interaction related to the one that does not (in particular at higher energy). A close look at Figure 45 (a), (c) and (e) suggests an increase in the widening of the distribution there shown, which the authors credit to a longer transit time, which leads to a higher impact of the e-e interaction mechanisms. Such widening seems to become less significant as the transit time increases. Figure 45(b), (d) and (f) present the same analysis, however for a 30 nm channel length device. In the large device, one cannot notice an increase in the widening of the distribution due to short-range e-e interactions as

even the carriers in the fastest window stay a long time in the channel. As the transit time increases, the SR e-e interaction becomes less noticeable in the range captured by this figure, despite of still being detected in the distributions' standard deviation. This result indicates the importance of considering the SR interactions when simulating deeply scaled devices, with carrier's transit time in the same order of magnitude as the characteristic carrier-carrier scattering time. For a better analysis, Tables I and II show the average and the standard deviation values of the distributions of Figure 45.

8.1.3. Ballistic Transport in n-FinFETs Conclusions

This study provided detailed information on ballistic transport in state-of-the-art FinFETs, in order to properly understand the underlying scattering mechanisms' relevance. For this purpose, the 3D-TCAD Monte Carlo device simulator introduced in this thesis was used, which is adequate to study electron-electron interactions and the role of different scattering mechanisms on charge carrier transport.

By examining the ballisticity ratio and the percentage of carriers that cross the channel ballistically, it becomes clear that modern FinFETs have not yet reached the ballistic limit. Therefore, there is still room for progress with different devices that may go in the direction of the ballistic limit. The fraction of ballistic carriers in the devices studied is significant, reaching almost 50% for the simulated 14 nm n-FinFETs. This compromises the concept of carriers' mobility in deeply scaled devices, as ballistic transport dominates. Monte Carlo device simulators are perfectly fit to simulate devices in such situations, since the simulator is in no way dependent on mobility as a parameter.

Furthermore, a detailed study of the role of phonon scattering and surface roughness scattering showed how their contributions evolve as channel length is scaled down. The surface roughness scattering event counts reduce at a higher rate than phonon scattering count as channel length decreases. For shorter channel lengths, phonon scattering is expected to dominate over interface roughness.

As channel length scales down, the distribution of the time the carriers take to cross the channel has a smaller average and a lighter tail for higher times, suggesting the increasing contribution of ballistic transport. If carriers stay longer in the channel, the average energy of the electrons gets smaller, but the standard deviation increases, so that a wider set of energies are present.

A thorough study of carrier dynamics, including the evolution of the carriers' energy distribution, was also presented in this study. When comparing ballistic and non-ballistic carriers, ballistic carriers show a higher average energy, but a longer tail at higher energy is seen for non-ballistic carriers. This is a relevant result, for instance, in the context of HCI.

Lastly, short-range electron-electron interactions' impact in the carriers' dynamics was presented, showing the increasing importance of a proper treatment of such mechanism as the ballistic transport becomes more present in state-of-the-art devices.

9 CONCLUSIONS

The ensemble Monte Carlo algorithm has been used as a numerical method to simulate particle transport in silicon. The Monte Carlo method is based on the generation of random walks that simulate the stochastic motion of carriers followed by scattering events that change their energy and momentum. The process of generating random free-flights is used to evaluate integral equations, so that the Monte Carlo technique has been widely used for semiconductor device simulation over the past decades, providing a semi-classical solution to the Boltzmann transport equation.

Semiconductor device simulation requires the self-consistent solution of the transport and the field equations. While the particle dynamics is emulated by solving BTE using Monte Carlo technique as discussed above, the electric fields are obtained by numerically solving Poisson's equation. The device simulation is basically composed of the initialization of material parameters, device structure and carrier distribution, Monte Carlo random walk/scattering, solution of Poisson's equation, and interpolation of force to particle location. During this process, the boundaries and the contacts are constantly checked, so that no carrier leaves the device unaccounted for.

The bulk Monte Carlo method was used to simulate particle dynamics in silicon. For every discrete energy level, the scattering tables define the scattering rate of all scattering processes that may take place, such as intravalley acoustic and intervalley non-polar optical phonon scatterings and coulomb scattering. The choice of which scattering event will take place is based on the generation of a random number and its comparison with the scattering table. The use of the bulk silicon Monte Carlo electron simulator has provided good modeling of events such as velocity overshoot, and the carrier velocity and energy dependences over electric field closely match the literature data.

A *n*-MOSFET 3D device simulator was implemented and produces good qualitative results. Contrary to the bulk silicon simulator, which is suitable for direct comparison of the results obtained with the developed simulator and experimental/simulation results present in the literature, it is rather difficult to quantitatively compare the results obtained with the device simulator to other published results. The coincidence of the results will only happen if one has access to all fabrication details of the studied devices, which are typically not fully disclosed by the foundries. Besides for that, regarding commercial TCAD tools, the models employed in the simulators are usually *drift-diffusion*, for long channel devices, or *hydrodynamic*, for short-channel devices, which have inherent different results and are

usually less accurate models. Regarding the studies performed on the *n*-MOSFET 3D device simulator developed in this thesis, the charge conservation on the device was verified by confirming that the derivative of the cumulative charge in the source and drain contacts have the same absolute value. The behavior of electron velocity and energy along the channel matches the expected results, with both quantities reaching their peak values near the drain end. The drain current *vs* gate voltage and drain current *vs* drain voltage curves also exhibited the usual *n*-MOSFET characteristics. The electric potential was plotted for different positions on the directions of device length, width and depth, as well as the carrier densities, showing good agreement with the expected tendencies.

Finally, the state-of-the-art n-FinFET 3D device simulator that was developed provides established results for the device transfer and output characteristics. Similarly to the n-MOSFET device, electron's velocity and energy along the channel matches the usual tendencies. The drain current versus gate or drain voltages curves presented the expected n-FinFET characteristics. The electrostatic potential was also plotted for different cross-sections in the directions of device length, width and depth. Both the electrostatic potentials and the carrier densities showed good agreement with the expected tendencies, corroborating that the 3-D particle-based device simulator presented in this work is adequate to simulate modern FinFETs.

The 3-D TCAD Monte Carlo simulator was employed to provide a thorough study of ballistic transport in modern FinFETs and investigate the scattering mechanisms' relevance. It was verified that, as channel length decreases, surface roughness scattering event counts reduce at a higher rate than phonon scattering count, so that phonon scattering is expected to dominate over interface roughness for shorter channel lengths. The quantification of the ballisticity ratio and the percentage of carriers that cross the channel ballistically showed that modern FinFETs have not yet reached the ballistic limit. The fraction of ballistic carriers in the studied devices is significant, however, reaching almost 50% for the simulated 14 nm n-FinFETs. Analyzing the distribution of the energy of the carriers grouped by the time they take to cross the channel, it was verified that, if carriers stay longer in the channel, the average energy of the electrons gets smaller, but the standard deviation increases, so that a wider set of energies is present. Carriers that cross the channel ballistically present a higher average energy, but non-ballistic carriers show a longer tail at higher energy. Finally, when the impact of short-range electron-electron interaction in the carriers' dynamics of FinFETs was evaluated, the importance of a proper treatment of such mechanism became clear, as the ballistic transport becomes more relevant in state-of-the-art devices.

REFERENCES

AHMED, S. S. **Modeling quantum and coulomb effects in nanoscale devices**. 2005. Tese (Doutorado em Engenharia Elétrica) – School of Electrical, Computer and Energy Engineering, Arizona State University, Tempe, 2005.

AKIS, R.; FARALLI, N.; FERRY, D. K.; GOODNICK, S. M.; PHATAK, K. A.; SARANITI, M. Ballistic Transport in InP-Based HEMTs. **IEEE Transactions on Electron Devices**, New York, v. 56, n. 12, p. 2935-2944, Dec. 2009.

BAYKAN, M. O.; THOMPSON, S. E.; NISHIDA, T. Size- and Orientation-Dependent Strain Effects on Ballistic Si p-Type Nanowire Field-Effect Transistors. **IEEE Transactions on Nanotechnology**, New York, v. 11, n. 6, p. 1231-1238, Nov. 2012.

BIELAJEW, A. F. **Fundamentals of the Monte Carlo method for neutral and charged particle transport**. Ann Arbor: The University of Michigan, 2001.

BINA, M.; RUPP, K.; TYAGINOV, S.; TRIEBL, O.; GRASSER, T. Modeling of hot carrier degradation using a spherical harmonics expansion of the bipolar Boltzmann transport equation. *In*: INTERNATIONAL ELECTRON DEVICES MEETING, 58., 2012, San Francisco. **Proceedings** […]. New York: IEEE, 2012. p. 30-5.

BROWN, A. R.; DAVAL, N; BOURDELLE, K. K.; NGUYEN, B. Y.; ASENOV, A. Comparative simulation analysis of process-induced variability in nanoscale SOI and bulk trigate FinFETs. **IEEE Transactions on Electron Devices**, New York, v. 60, n. 11, p. 3611-3617, Nov. 2013.

BUFLER, F. M.; MIYAGUCHI, K.; CHIARELLA, T.; HORIGUCHI, N.; MOCUTA, A. On the ballistic ratio in 14nm-Node FinFETs. *In:* EUROPEAN SOLID-STATE DEVICE RESEARCH CONFERENCE, 47., 2017, Leuven. **Proceedings** […] New York: IEEE, 2017. p. 176-179.

BUFLER, F.M.; SMITH, L. 3D Monte Carlo simulation of FinFET and FDSOI devices with accurate quantum correction, **Journal of Computational Electronics**, New York, v. 12, n. 12, p. 651–657, Dec. 2013.

CAMARGO, V. V. A. **Evaluating the impact of charge traps on MOSFETs and circuits**. 2016. Tese (Doutorado em Microeletrônica) – Programa de Pós-Graduação em Microeletrônica, Universidade Federal do Rio Grande do Sul, Porto Alegre, 2016.

CANALI, C.; JACOBONI, C.; NAVA, F.; OTTAVIANI, G.; ALBERIGI-QUARANTA, A. Electron drift velocity in silicon. **Physical Review B**, Ridge, v. 12, n. 6, p. 2265-2284, Sept. 1975.

COSTATO, M.; REGGIANI, L. Nonparabolicity and overlap effects on transport problems in the Froehlich and Paranjape approach. **Journal of Physics C: Solid State Physics**, Bristol, v. 5, n. 2, p. 159, 1972.

CURATOLA, G.; FIORI; IANNACCONE, G., Modelling and simulation challenges for nanoscale MOSFETs in the ballistic limit. **Solid-State Electronics**, Amsterdam, v. 48, n. 4, p. 581-587, Apr. 2004.

DADGOUR, H. F.; ENDO, K.; DE, V. K.; BANERJEE, K. Grain-Orientation Induced Work Function Variation in Nanoscale Metal-Gate Transistors - Part I: Modeling, Analysis, and Experimental Validation. **IEEE Transactions on Electron Devices**, New York, v. 57, n. 10, p. 2504-2514, Oct. 2010.

ELTHAKEB, A. T.; ELHAMID; H. A., ISMAIL; Y., Scaling of TG-FinFETs: 3-D Monte Carlo Simulations in the Ballistic and Quasi-Ballistic Regimes. **IEEE Transactions on Electron Devices**, New York, v. 62, n. 6, p. 1796-1802, Jun. 2015.

FAWCETT, W.; BOARDMAN, A; D.; SWAIN, S. "Monte Carlo Determination of Electron Transport in Gallium Arsenide". **Journal of the Physics and Chemistry of Solids**, Amsterdam, v. 31, n. 9, p.1962-1990, Sept. 1970.

FERRY, D. K. First-order optical and intervalley scattering in semiconductors. **Physical Review B**, Ridge, v. 14, n. 4, p. 1605, Aug. 1976.

FERRY, D. K.; GRONDIN, R. O. **Physics of submicron devices**. New York: Springer, 1991.

FERRY, D.; GOODNICK, S. M. **Transport in nanostructures**. Cambridge: Cambridge University Press, 1997.

Reprinted, with permission, from FURTADO, G. F.; CAMARGO, V. V. A.; VASILESKA, D.; WIRTH, G. I. Evaluating the Ballistic Transport in nFinFETs: a Carrier Centric Perspective. Submitted to **IEEE Transactions on Nanotechnology**, 2021a.

FURTADO, G. F.; CAMARGO, V. V. A.; VASILESKA, D.; WIRTH, G. I. Correlation of HCD and percolation paths in FinFETs: study of RDF and MGG impacts through 3-D Particle-Based Simulation. 2021b.

FURTADO, G. F.; CAMARGO, V. V. A.; VASILESKA, D.; WIRTH, G. I. 3-D TCAD Monte Carlo Device Simulator: State-of-the-art FinFET Simulation. Accepted for publication in **Journal of Integrated Circuits and Systems,** 2021c.

GNANI; E.; GNUDI, A.; REGGIANI, S.; BACCARANI, G. Ballistic ratio and backscattering coefficient in short-channel NW-FETs. *In:* EUROPEAN SOLID STATE DEVICE RESEARCH CONFERENCE, 39., 2009, Athens. **Proceedings** […]. New York: IEEE, 2009. p. 476-479.

GREENGARD, L.; ROKHLIN, V. A fast algorithm for particle simulations. **Journal of Computational Physics**, v. 135, n. 2, p. 280-292, Aug. 1997.

GROSS, W. J.; VASILESKA, D.; FERRY, D. K. A novel approach for introducing the electron-electron and electron-impurity interactions in particle-based simulations. **IEEE Electron Device Letters**, New York, v. 20, n. 9, p. 463-465, Sept. 1999.

GROSS, W. J.; VASILESKA, D.; FERRY, D. K. 3D simulations of ultra-small MOSFETs with real-space treatment of the electron-electron and electron-ion interactions. **VLSI Design**, v. 10, n. 4, p. 437–452, Jan. 2000.

HAMAGUCHI, C.; HAMAGUCHI, C. **Basic semiconductor physics**. Berlin: Springer, 2001.

HATHWAR, R. **Generalized Monte Carlo Tool for Investigating Low-Field and High Field Properties of Materials Using Non-parabolic Band Structure Model**. 2011. Dissertação (Mestrado em Engenharia Elétrica) – School of Electrical, Computer and Energy Engineering, Arizona State University, Tempe, 2011.

HOCKNEY, R. W.; EASTWOOD, J. W. **Computer simulation using particles**. Boca Raton: CRC Press, 1988.

JACOBONI, C.; CANALI, C.; OTTAVIANI, G.; ALBERIGI-QUARANTA, A. A review of some charge transport properties of silicon. **Solid-State Electronics**, Amsterdam, v. 20, n. 2, p. 77-89, Feb. 1977.

JACOBONI, C.; LUGLI, P. **The Monte Carlo method for semiconductor device simulation**. New York: Springer Science & Business Media, 2012.

KHAN, H. R.; MAMALUY, D.; VASILESKA, D. Quantum Transport Simulation of Experimentally Fabricated Nano-FinFET. **IEEE Transactions on Electron Devices**, New York, v. 54, n. 4, p. 784-796, Apr. 2007.

KIM, R.; LUNDSTROM, M. S. Characteristic Features of 1-D Ballistic Transport in Nanowire MOSFETs. **IEEE Transactions on Nanotechnology**, New York, v. 7, n. 6, p. 787-794, Nov. 2008.

KNEZEVIC, I. RAMAYVA, E. B.; VASILESKA, D.; GOODNICK, S. M. Diffusive transport in quasi-2D and quasi-1D electron systems. **Journal of Computational and Theoretical Nanoscience**, Valencia, v. 6, n. 8, p. 1725-1753, Aug. 2009.

LEE, Y.; LIAO, P. J.; JOSHI, K.; HUANG, D. S. Circuit-based reliability consideration in FinFET technology. In: INTERNATIONAL SYMPOSIUM ON THE PHYSICAL AND FAILURE ANALYSIS OF INTEGRATED CIRCUITS, 24., 2017,

2017 IEEE 24th International Symposium on the Physical and Failure Analysis of Integrated Circuits (IPFA). Chengdu. **Proceedings** [...]. New York: IEEE, 2017. p. 1-7.

LUNDSTROM, M. **Fundamentals of carrier transport**. Cambridge: Cambridge university press, 2009.

NAGY, D.; INDALECIO, G.; GARCÍA-LOUREIRO, A. J.; ELMESSARY, M. A.; KALNA, K.; SEOANE, N. Metal Grain Granularity Study on a Gate-All-Around Nanowire FET. **IEEE Transactions on Electron Devices**, New York, v. 64, n. 12, p. 5263-5269, Dec. 2017.

OTHONOS, A. Probing ultrafast carrier and phonon dynamics in semiconductors, **Journal of applied physics**, Melville, v. 83, n. 4, p. 1789-1830, Jul. 1998.

PALESTRI, P., ESSENI, D., EMINENTE, S., FIEGNA, C., SANGIORGI, E. M SELMI, L. Understanding quasi-ballistic transport in nano-MOSFETs: part I-scattering in the channel and in the drain. **IEEE Transactions on Electron Devices**, New York, v. 52, n. 12, p. 2727-2735, Dec. 2005.

PALESTRI, P.; ESSENI, D.; EMINENTE, C.; FIEGNA, C.; SANGIORGI, E.; SELMI, L. A Monte-Carlo study of the role of scattering in deca-nanometer MOSFETs. *In*: IEEE INTERNATIONAL ELECTRON DEVICES MEETING, 50., 2004, San Francisco. **Proceedings** […]. New York: IEEE, 2004. p. 605-608.

RAHMAN, A.; GUO, J.; DATTA, S.; LUNDSTROM, M. S. Theory of ballistic nanotransistors. **IEEE Transactions on Electron Devices**, New York, v. 50, n. 9, p. 1853-1864, Sept. 2003.

STONE, H. L. Iterative solution of implicit approximations of multidimensional partial differential equations. **SIAM Journal on Numerical Analysis**, Philadelphia, v. 5, n. 3, p. 530-558, Sept. 1968

SUDARSANAN, A.; VENKATESWARLU, S.; NAYAK, K. Impact of Fin Line Edge Roughness and Metal Gate Granularity on Variability of 10-nm Node SOI n-FinFET. **IEEE Transactions on Electron Devices**, New York, v. 66, n. 11, p. 4646-4652, Nov. 2019.

TIERNEY, B. D. **Monte Carlo Studies of Electron Transport In Semiconductor Nanostructures**. 2011. Tese (Doutorado em Engenharia Elétrica) – School of Electrical, Computer and Energy Engineering, Arizona State University, Tempe, 2011.

TOMIZAWA, K. **Numerical Simulation of Submicron Semiconductor Devices**. Boston: Artech House, 1993.

TOWIE, E. A. **Extended models of Coulomb scattering for the Monte Carlo simulation of nanoscale silicon MOSFETs**. 2010. Tese (Doutorado em Engenharia Elétrica) – Department of Electronics and Electrical Engineering, University of Glasgow, Glasgow, 2010.

VARDHAN, P. H.; MITTAL, S.; GANGULY, S.; GANGULY, U. Analytical Estimation of Threshold Voltage Variability by Metal Gate Granularity in Fin-FET. **IEEE Trans on Electron Devices**, New York, v. 64, n. 8, p. 3071-3076, Aug. 2017.

VASILESKA, D. **Direct Solution of Boltzmann Transport Equation: Monte Carlo Method**. Disponível em: https://nanohub.org/resources/9111/download/monte_carlo.pdf. Acesso em: 17 jun. 2021.

VASILESKA, D.; GOODNICK, S. M. (Ed.). **Nano-Electronic Devices: Semiclassical and Quantum Transport Modeling**. New York: Springer Science & Business Media, 2011.

VASILESKA, D.; GOODNICK, S. M. **Bulk Monte Carlo Code Described**. 2008. Disponível em: https://nanohub.org/resources/4843. Acesso em: 17 jun. 2021.

VASILESKA, D.; GOODNICK, S. M.; KLIMECK, G. **Computational Electronics: semiclassical and quantum device modeling and simulation**. Boca Raton: CRC press, 2016.

WANG, X.; BROWN, A. R.; CHENG, B.; ASENOV, A. Statistical variability and reliability in nanoscale FinFETs. *In:* INTERNATIONAL ELECTRON DEVICES MEETING, 57., 2011, Washington DC. **Proceedings** [...]. New York, 2011, p. 5.4.1-5.4.4.

WEBER, L.; GMELIN, E. Transport properties of silicon. **Applied Physics A**, New York, v. 53, n. 2, p. 136-140, Aug. 1991.

WORDELMAN, C. J.; RAVAIOLI, U. Integration of a particle-particle-particle-mesh algorithm with the ensemble Monte Carlo method for the simulation of ultra-small semiconductor devices. **IEEE Transactions on Electron Devices**, New York, v. 47, n. 2, p. 410-416, Feb. 2000.